



POLITECNICO DI TORINO  
Repository ISTITUZIONALE

Design Methods for Surface-Mounted Permanent Magnet Synchronous Machines

*Original*

Design Methods for Surface-Mounted Permanent Magnet Synchronous Machines / Lu, Chao. - (2018 Mar 23).

*Availability:*

This version is available at: 11583/2704285 since: 2018-03-26T11:15:30Z

*Publisher:*

Politecnico di Torino

*Published*

DOI:10.6092/polito/porto/2704285

*Terms of use:*

Altro tipo di accesso

This article is made available under terms and conditions as specified in the corresponding bibliographic description in the repository

*Publisher copyright*

(Article begins on next page)



# ScuDo

Scuola di Dottorato ~ Doctoral School

WHAT YOU ARE, TAKES YOU FAR

Doctoral Dissertation

Doctoral Program in Electrical, Electronics and Communication Engineering  
(30<sup>th</sup> cycle)

# **Design Methods for Surface-Mounted Permanent Magnet Synchronous Machines**

By

**Chao Lu**

\*\*\*\*\*

**Supervisor(s):**

Prof. Gianmario Pellegrino

**Doctoral Examination Committee:**

Prof. A.B. , Referee, University of...

Prof. C.D, Referee, University of...

Prof. E.F, University of...

Prof. G.H, University of...

Prof. I.J, University of...

Politecnico di Torino

2018



## Declaration

I hereby declare that, the contents and organization of this dissertation constitute my own original work and does not compromise in any way the rights of third parties, including those relating to the security of personal data.

Chao Lu  
2018

\* This dissertation is presented in partial fulfillment of the requirements for **Ph.D. degree** in the Graduate School of Politecnico di Torino (ScuDo).

*I would like to dedicate this thesis to my beloved parents for persistent support*

## **Acknowledgements**

First of all, I deeply appreciate my supervisor, Prof. Gianmario Pellegrino who gives me infinite guidance, encouragement, and assistance in every aspect of my study during these years. His care, patience, and kindness provide me a strong support at the initial days when everything was in mess in both study and life experiences. His expectation on my study also brings me about the hope and strengths to overcome the troubles in the research. I am very grateful and honored to work with such a knowledgeable professor.

Sincere gratitude to China Scholar Council for providing me financial support during the three years.

My colleagues in our group also give me kindly support during the study. My appreciation is given to Dr. Matteo Gamba, Dr. Arzhang Yousefi-talouki, Mr. Simone Ferrari, Mr. Paolo Pescetto and Mr. Fausto Stella. They are not just colleagues but also friends. I would like to thank other professors and colleagues in Energy Department that create an excellent research atmosphere.

Finally, I would like to give a special thank to my parents who support me to finish my work in a long distance.

## **Abstract**

Permanent magnet synchronous machines (PMSMs) provide several advantages compared with induction machine, such as higher power and torque density, and better dynamic response. Among PMSMs, Surface-mounted permanent magnet (SPM) machine has simple rotor configuration and easy control strategy due to its isotropic characteristics.

Plenty of publications have illustrated the fundamentals and the design methods of SPM machines. Based on these, this dissertation presents new design methods for SPM machines. Both design methods are comprehensively illustrated. The presented design methods are embedded into a machine design platform available online.

One of the new methods is an automatic design procedure using multi objective optimization algorithm, whose principle is to combine multi objective differential evolution (MODE) optimization with finite element analysis (FEA) to obtain the machine with the best trade-off among the targeted objectives, like maximum torque, minimum torque ripple, good flux weakening capability, etc. Two cases are reported by using such automatic design method, one for a SPM machine with concentrated winding (CW-SPM) and the other with distributed windings (DW-SPM), respectively. The CW-SPM machine is designed for traction application. In this case, design equations, magnetic FEA, multi objective optimization, simplified structural and thermal co-design are presented. Torque and power profiles of the designed machine are reported. The losses and efficiency map are also presented. The other case is the DW-SPM machine capable of low cogging torque thanks to the automatic design procedure. Dependent on demagnetization limit and optimal magnet span calculation, the magnet bounds in optimization process are obtained. The cogging torque and maximum torque waveforms of three different machines on Pareto front are shown, which are ob-

tained by MODE optimization and FEA simulations. One optimum machine is selected as the best trade-off machine among PM volume, torque and cogging torque behaviors.

Besides the automatic design process, the other design method called parametric design for SPM machines is reported. The parametric design provides a very effective and concise solution for SPM machine design on the machine performance calculation. Three steps of parametric design development are shown. For each step, design flowcharts and examples are presented. Firstly, a parametric design plane is established based on rotor split ratio  $x$  and per unit magnetic loading  $b$ . All the sizing equations, torque and power factor calculation are functions of  $x$  and  $b$ . An example for designing a CW-SPM machine for traction application is reported. Later the parametric design plane is modified into the  $x$  and  $l_m/g$  plane, the latter parameter being the magnet-airgap length ratio, since  $l_m/g$  directly relates to the airgap flux density distribution. The comprehensive design process of SPM machines using the parametric plane ( $x, l_m/g$ ) is described. A prototype is built and verified the validity of the design process. Then, a general design approach based on accurate steel loading for both DW and CW SPM machines is proposed. By using subdomain model during the design process, the stator sizing equations are improved by considering the only one most loaded slot pitch rather than the entire pole pitch. Five different cases of SPM machines are analyzed to get the precise flux quantities passing through the most loaded tooth. A comprehensive parametric design flowchart for SPM machines is addressed. The steel loading on each tooth and yoke are measured by FEA and compared with target steel loading  $B_{fe}$  at open load condition, which shows good agreements with analytical cases. Finally, the designs are also tested at the respective rated currents. The presented methods give insightful and effective means in the SPM machine design.

## Publication

- C. Lu, S. Ferrari, G. Pellegrino, C. Bianchini and M. Davoli, "Parametric Design Method for SPM Machines Including Rounded PM Shape," *2017 IEEE Energy Conversion Congress and Exposition (ECCE)*, Cincinnati, Ohio, 2017, pp. 4309-4315.
- C. Lu and G. Pellegrino, "Magnet Shape Optimization of Surface-mounted Permanent Magnet Synchronous Machine through FEA Method," *Journal of Electrical Engineering*, vol.17, no.3, 2017, pp. 498-506.
- C. Lu, S. Ferrari and G. Pellegrino, "Two Design Procedures for PM Synchronous Machines for Electric Powertrains," in *IEEE Transactions on Transportation Electrification*, vol. 3, no. 1, pp. 98-107, March 2017.
- C. Lu and G. Pellegrino, "A simple design method for surface-mounted PM machines for traction application," *2016 IEEE Energy Conversion Congress and Exposition (ECCE)*, Milwaukee, WI, 2016, pp. 1-7.
- C. Lu, M. Abshari, and G. Pellegrino, "Design of two PM Synchronous Machines for EV Traction Using Open-Source Design Instruments," *2016 Advance in Magnetics (AIM)*, Bormio, Italy, 2016.

# Contents

<b>List of Figures</b>	<b>xii</b>
------------------------	------------

<b>List of Tables</b>	<b>xvii</b>
-----------------------	-------------

<b>1 Background and Objectives</b>	<b>1</b>
1.1 Preface . . . . .	1
1.2 SyR-e . . . . .	4
1.2.1 SyR-e Development . . . . .	4
1.2.2 SyR-e Operation . . . . .	10
1.3 Research Objectives . . . . .	12
<b>2 Surface-mounted Permanent Magnet Synchronous Machine</b>	<b>14</b>
2.1 Introduction . . . . .	14
2.2 Permanent Magnet Synchronous Machine . . . . .	14
2.2.1 Surface-mounted Permanent Magnet Synchronous Machine	16
2.2.2 Surface Inset Permanent Magnet Synchronous Machine . . .	16
2.2.3 Interior Permanent Magnet Synchronous Machine . . . . .	17
2.3 Fundamentals of SPM Machines . . . . .	17
2.3.1 Permanent Magnet Material . . . . .	17
2.3.2 Airgap Flux Density . . . . .	19
2.3.3 Induced emf . . . . .	23

---

2.3.4	Torque and Power . . . . .	24
2.3.5	Maximum Current Limit . . . . .	25
2.3.6	Synchronous Inductance . . . . .	25
2.3.6.1	Magnetizing Inductance . . . . .	25
2.3.6.2	Slot Leakage Inductance . . . . .	26
2.3.6.3	Tooth Tip Leakage Inductance . . . . .	27
2.4	Windings . . . . .	27
2.4.1	Distributed Windings . . . . .	28
2.4.2	Concentrated Windings . . . . .	30
<b>3</b>	<b>Automatic Design Using Optimization Algorithms</b>	<b>32</b>
3.1	Automatic Design for Traction Application . . . . .	32
3.1.1	Design Background . . . . .	32
3.1.2	Design Conditions for Traction Machines . . . . .	34
3.1.3	Design Flowchart . . . . .	36
3.1.3.1	Design Input . . . . .	37
3.1.3.2	Design Flowchart . . . . .	41
3.1.3.3	Non Magnetic Aspects . . . . .	43
3.1.4	Results . . . . .	44
3.1.4.1	Torque and Power Curves . . . . .	45
3.1.4.2	Loss and Efficiency Maps . . . . .	46
3.1.5	Design Summary . . . . .	48
3.2	Automatic Design of a DW-SPM Machine . . . . .	48
3.2.1	Design Background . . . . .	48
3.2.2	Design Flowchart . . . . .	50
3.2.2.1	Rotor Geometry . . . . .	50
3.2.2.2	Design Input . . . . .	50



3.2.3	Results . . . . .	54
3.2.4	Design Summary . . . . .	59
<b>4</b>	<b>Parametric Design Procedure for SPM Machines</b>	<b>60</b>
4.1	Parametric Design Procedure Based on $(x, b)$ Plane . . . . .	61
4.1.1	Design Background . . . . .	61
4.1.2	Design Procedure . . . . .	61
4.1.2.1	Nominal PF as the Metrics of the Flux Weakening Range . . . . .	63
4.1.2.2	Design Input . . . . .	65
4.1.2.3	Parametric Design Plane $(x, b)$ . . . . .	65
4.1.2.4	Torque and PF Expressions . . . . .	69
4.1.2.5	Design Flowchart . . . . .	72
4.1.2.6	Demagnetization Limit . . . . .	73
4.1.3	Results . . . . .	74
4.1.3.1	Design Examples . . . . .	74
4.1.3.2	Power and Torque Envelopes . . . . .	75
4.1.4	Design Summary . . . . .	77
4.2	Parametric Design Procedure Based on $(x, l_m/g)$ Plane . . . . .	78
4.2.1	Design Background . . . . .	78
4.2.2	Design Procedure . . . . .	79
4.2.2.1	Machine Specification . . . . .	79
4.2.2.2	Rotor Geometry . . . . .	80
4.2.2.3	Airgap Flux Density . . . . .	81
4.2.2.4	Design Input . . . . .	85
4.2.2.5	Parametric Design Plane $(x, l_m/g)$ . . . . .	85
4.2.2.6	Torque and PF Expressions . . . . .	87

---

4.2.2.7	Flowchart . . . . .	87
4.2.3	Results . . . . .	91
4.2.3.1	Design Examples . . . . .	91
4.2.3.2	FEA Simulation Results . . . . .	92
4.2.3.3	Experimental Validation . . . . .	94
4.2.4	Design Summary . . . . .	98
4.3	Parametric Design Procedure Based on Subdomain Model . . . . .	99
4.3.1	Design Background . . . . .	99
4.3.2	Design Procedure . . . . .	100
4.3.2.1	Airgap Flux Model . . . . .	100
4.3.2.2	Subdomain Model . . . . .	101
4.3.2.3	Stator Sizing . . . . .	106
4.3.2.4	Design Input . . . . .	115
4.3.2.5	Design Flowchart . . . . .	115
4.3.3	Design Examples and Results . . . . .	117
4.3.3.1	Steel Loading . . . . .	118
4.3.3.2	Torque and PF Results . . . . .	118
4.3.3.3	Efficiency . . . . .	122
4.3.4	Design Summary . . . . .	123
<b>5</b>	<b>Conclusion, and Future Work</b>	<b>124</b>
5.1	Conclusion . . . . .	124
5.2	Future Work . . . . .	126
	<b>References</b>	<b>127</b>

# List of Figures

1.1	Classification of electrical machine . . . . .	3
1.2	SyR-e working principle . . . . .	4
1.3	SyR-e circular and segmented flux barriers definition . . . . .	5
1.4	$\Delta x$ definition for flux barriers . . . . .	6
1.5	Effect on $\Delta x$ . . . . .	6
1.6	Fluid barrier shape . . . . .	7
1.7	Winding definition in SyR-e, (a) DW; (b) CW; (c) non-conventional fractional slot . . . . .	8
1.8	Automatic design of additional radial bridges for different speed ratings. a) Max speed 3,000 rpm; b) Max speed 12,000 rpm . . . . .	9
1.9	SyR-e main dialog view . . . . .	10
1.10	SyR-e automatic design setup tab . . . . .	11
1.11	SyR-e non-magnetic design view tab . . . . .	12
2.1	Main rotor configurations of PMSMs . . . . .	15
2.2	$B - H$ curve for a typical PM material . . . . .	18
2.3	Demagnetization curve for <i>BMN-38H</i> , <i>BOMATEC</i> . . . . .	18
2.4	Parallel (a) and radial (b) magnetization . . . . .	19
2.5	$B_g$ waveform for slotless SPM machines, (a) parallel, (b) radial . . .	20
2.6	Slot view and $B_g$ waveform . . . . .	21

2.7	$B_{g\_avg}$ results comparison between (2.7) and FEA . . . . .	22
2.8	$B_m$ and $B_{m1}$ waveform over one pole pair . . . . .	23
2.9	A simplified slot view . . . . .	26
2.10	Winding configuration of DW-SPM with $p = q = 2$ . . . . .	28
2.11	Effect of winding distribution . . . . .	29
2.12	Short pitching of a coil . . . . .	29
2.13	Phasor of short pitching . . . . .	30
2.14	Slot skewing . . . . .	30
2.15	Winding views of three-phase CW-SPM machines, (a) single-layer; (b) double-layer . . . . .	31
3.1	Torque versus speed requirements of an electric vehicle . . . . .	35
3.2	Vector diagram of CW-SPM machines supplied at their characteristic current . . . . .	36
3.3	Torque (a) and power (b) versus speed profiles supplied with charac- teristic current, under constrained voltage . . . . .	37
3.4	Automatic design flowchart for the CW-SPM machines . . . . .	40
3.5	(a) Torque evaluation, current is placed $\gamma = 90^0$ . (b) Flux weakening capability evaluation: current is placed at $\gamma = 180^0$ . . . . .	41
3.6	Pareto front of CW-SPM design optimization . . . . .	42
3.7	Power profile of CW-SPM machines . . . . .	42
3.8	Temperature result for CW-SPM under repeated NEDC conditions .	43
3.9	Motor structures: (a) benchmark CW-SPM; (b) present CW-SPM . .	44
3.10	Torque curve at their characteristic current and at maximum inverter current, considering the maximum voltage limit . . . . .	45
3.11	Power curve at their characteristic current and at maximum inverter current, considering the maximum voltage limit . . . . .	46
3.12	Efficiency map . . . . .	46

3.13 Power loss at specific points of the new machine, and comparison with the benchmark machine . . . . .	47
3.14 Definition of PM parameters . . . . .	49
3.15 Flowchart of optimization procedure for $T_{cog}$ and torque . . . . .	51
3.16 Operating point determination with demagnetization limit (NdFeB 32 MGOe at 80 °C) . . . . .	53
3.17 Relationship among $\beta$ , $l_m$ and maximum allowed current . . . . .	53
3.18 Pareto front of both GS and LS stages . . . . .	55
3.19 Three different machines cross-sections from Pareto front . . . . .	56
3.20 Cogging torque waveforms of three motors . . . . .	58
3.21 Torque waveforms of the three motors . . . . .	58
4.1 Torque and power versus profiles under characteristic current and limited inverter voltage conditions. Two designs are reported: one with rated current equal to $I_{ch}$ (continuous line) and rated current greater than $I_{ch}$ (dashed line) . . . . .	63
4.2 Vector diagram of the CW-SPM machine with $I_{ch}$ applied on the $q$ axis	64
4.3 Definition of $x$ and $b$ . . . . .	66
4.4 Definition of $w_t$ , $l_y$ and $l_m$ as a function of design parameters $x, b$ .	68
4.5 $T(x, b)$ and $PF(x, b)$ design plane . . . . .	70
4.6 Flowchart of the design procedure for traction motors . . . . .	71
4.7 Power (a) and torque (b) profiles of Motor 3, for same $k_j [W/m^2]$ and different number of turns . . . . .	75
4.8 Power profile for Motor 3 . . . . .	76
4.9 Loss map and torque profile of Motor 3 . . . . .	76
4.10 Efficiency map of Motor 3 . . . . .	77
4.11 Definition of design parameters for SPM machines . . . . .	81
4.12 $B_{g\_avg}$ comparison between (4.22) and FEA results . . . . .	82

4.13 Airgap flux density distribution of a slotless motor, analytical results: continuous lines; FEA results: circle marked . . . . .	84
4.14 $B_g$ spectrum of different $\beta$ . . . . .	85
4.15 Stator geometry definition . . . . .	86
4.16 Torque and PF design plane, $\alpha_m = 171^\circ$ , (a). $\beta = 1$ , (b). $\beta = 0.33$ . . .	87
4.17 Flowchart of the design procedure . . . . .	89
4.18 Operating point determination with demagnetization limit (NdFeB 32 MGOe at $80^\circ\text{C}$ ) . . . . .	90
4.19 Relationship among $\beta$ , $l_m$ and maximum allowed current . . . . .	90
4.20 Model view from parametric planes in Fig.4.16 . . . . .	91
4.21 Rotor view of Motor 4 . . . . .	92
4.22 Torque waveforms of the four motors . . . . .	94
4.23 Experimental scheme . . . . .	95
4.24 Test bench for rounded SPM motor . . . . .	95
4.25 Torque-current curve along MTPA route comparisons among FEA, experimental results and design plane . . . . .	96
4.26 Torque (a) and PF (b) maps the from experimental test . . . . .	97
4.27 Torque ripple results . . . . .	98
4.28 Comparisons among simplified, improved models and FEA results on maximum airgap flux density, parallel magnetization . . . . .	101
4.29 Analytical subdomain model view . . . . .	102
4.30 $B_{gr1}$ and $B_{gt1}$ comparisons between analytical and FEA results over one pole pitch . . . . .	106
4.31 Stator geometry definition for DW-SPM motors . . . . .	108
4.32 $B_g$ waveforms for DW-SPM motors . . . . .	108
4.33 Stator geometry definition for CW-SPM motors when $\tau_{PM} < \tau_s$ . . .	109
4.34 $B_g$ waveforms for CW-SPM motors when $\tau_{PM} < \tau_s$ . . . . .	110

4.35 Stator geometry definition for CW-SPM motors when $\tau_{PM} < \tau_s$ with small PM intervals . . . . .	111
4.36 $B_g$ waveforms for CW-SPM motors when $\tau_{PM} < \tau_s$ with small PM intervals . . . . .	111
4.37 Stator geometry definition for CW-SPM motors when $\tau_{PM} > \tau_s$ . . .	112
4.38 $B_g$ waveforms for CW-SPM motors when $\tau_{PM} > \tau_s$ . . . . .	113
4.39 Stator geometry definition for CW-SPM motors when $\tau_{PM} > 2\tau_s$ . .	114
4.40 $B_g$ waveforms for CW-SPM motors when $\tau_{PM} > 2\tau_s$ . . . . .	114
4.41 Flowchart of parametric design procedure . . . . .	116
4.42 Parametric plane of Case 2 . . . . .	120
4.43 Geometry Case 2 . . . . .	120
4.44 Parametric plane of Case 3 . . . . .	121
4.45 Geometry Case 3 . . . . .	121
4.46 Torque and efficiency comparison between Case 2a and 2b . . . . .	122
4.47 Torque and efficiency comparison between Case 3a and 3b . . . . .	123

# List of Tables

1.1	Characters of different electrical machines . . . . .	2
3.1	Machine data . . . . .	39
3.2	Main parameters of target machine . . . . .	52
3.3	Limit of search space for optimization . . . . .	54
3.4	Analytical and FEA results comparison on magnet edge . . . . .	57
4.1	Ratings of the CW-SPM motor . . . . .	67
4.2	Comparison between estimated and FEA results . . . . .	73
4.3	Ratings of the DW-SPM machine . . . . .	80
4.4	Comparison between analytical model and FEA . . . . .	84
4.5	Comparison between parametric and FEA results . . . . .	93
4.6	Common ratings of motor models . . . . .	117
4.7	Comparison between parametric method and FEA results . . . . .	119



# Chapter 1

## Background and Objectives

### 1.1 Preface

The most of the electrical energy is generated from electrical machines from primary energy resources and renewable sources. And more than half of the total electrical energy is consumed by electrical machines [1–4]. Affected by the greenhouse emission effect, the fossil fuels have to be substituted. Electrical machine is a very promising alternative to replace the use of fossil resources in many aspects, including transportation, industrial application, etc... [5–7]. Electrical machines are divided into AC and DC machines, in terms of different current input. Considering AC machines, induction machine and synchronous machine are separated according to rotating mechanism. When the rotor is magnetized either from a DC current or Permanent magnet (PM), the relevant synchronous machines are called wound, or PM synchronous machine (PMSM), respectively [8–11]. The classification of electrical machine is presented in 1.1, and the characters of different electrical machines are reported in Table 1.1.

PM materials with high energy product have been developed in their magnet energy product properties during last half century [12]. NeFeB magnets are able to contain higher maximum energy product, more robust against the operating temperature and improved magnetization behaviors [13, 14].

Benefited from the improvement of the PMs, PMSMs have been significantly developed since 1950s. Although induction motors are prevailed in industrial applications, PMSMs have become competitive alternatives, since they can improve

Table 1.1 Characters of different electrical machines

Machine type	Advantage	Disadvantage
Induction machine	Simple and robust structure	Relatively low efficiency
PMSMs	High torque density and efficiency	Magnets retention problem
	Good dynamics	Low inductance
Synchronous reluctance	High saliency	Low power factor
	Simple control strategy	Complex rotor designs
Switched reluctance	High speed	Serious torque ripple and noise
Flux switching machine	High torque density and robust rotor structure	Complicated in manufacture and more PM quantity
BLDC	High speed and reliability	Electronic commutation is needed

both steady-state and dynamic performances, compared with induction motors [15]. Efficiency is highly increased since PMSMs have no excitation loss and windings on the rotor. Power and torque densities are also increased, compared with current excited machines [16–18]. Thanks to the improved performance of the recent permanent magnet materials, such machines exhibit high efficiency and high torque density [27, 28]. Among PMSMs, SPM machines have simple rotor geometry. Meanwhile, compared with other PMSMs or synchronous reluctance (SyR) machine [29–31], the control strategy for SPM machines is also concise due to its isotropic geometry.

In terms of application aspects, PMSMs have been used in electric powertrains [19, 20], direct-drive home applications [21], servo motors in industry [22], and aerospace actuators [23].

Nonetheless, the PM materials might be demagnetized irreversibly, resulting from the thermal issue and excessive current loading [24]. A powerful cooling system should be used to keep the machine temperature under control. Moreover, mitigating PM losses should also be considered in the design process of PMSMs

[25, 26]. The PMs also increase the entire raw material cost of the electrical machines. In case of fault situation, the back EMF is also way high.

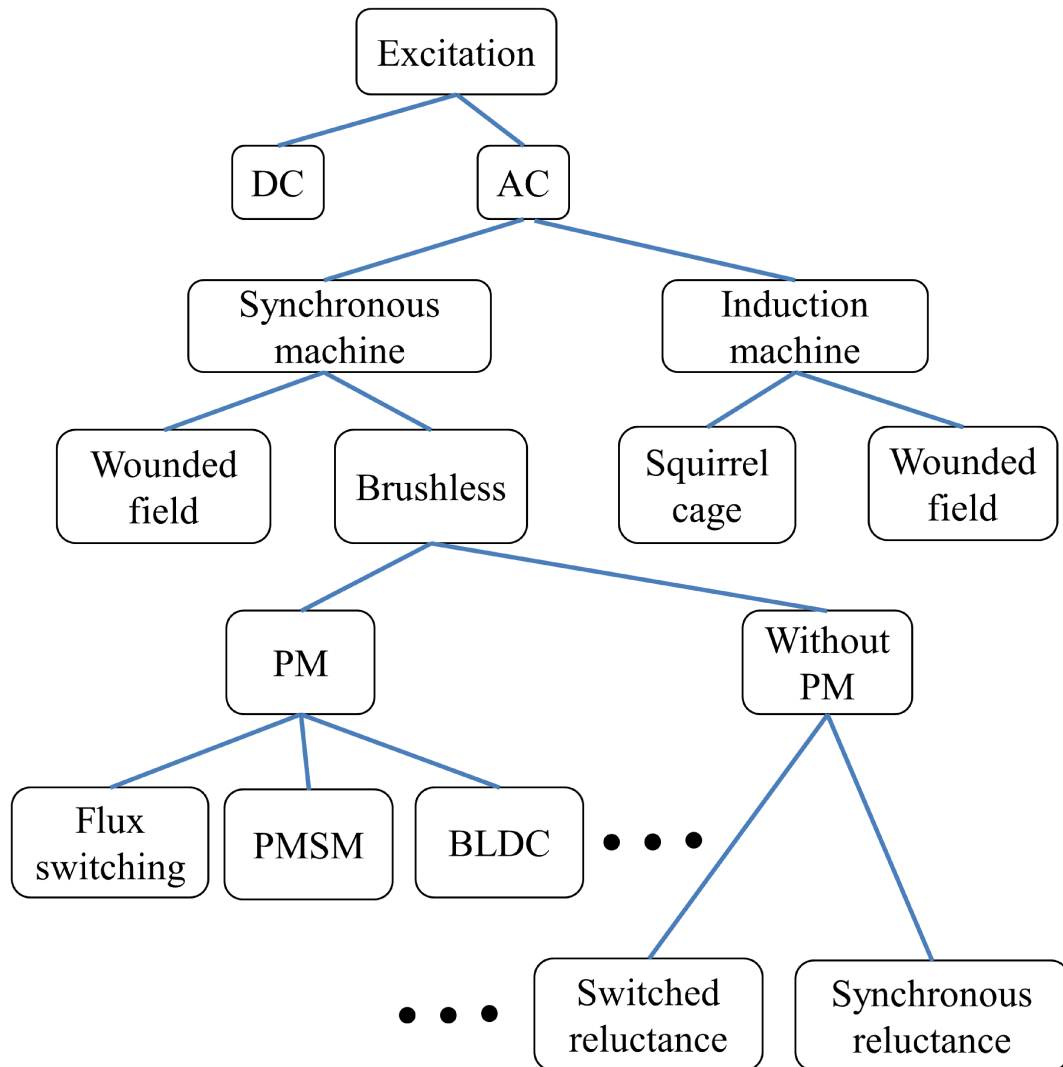


Fig. 1.1 Classification of electrical machine

Finite element analysis (FEA) has been applied in the electrical machine analysis since last decades. As a numerical method, FEA is highly precise in computing the distribution of the electromagnetic field, based on the solution of Maxwell's equations. However, if the elements quantity is huge, the required computing time will last long [32, 33]. Thanks to the significant improvement in computing hardware and FEA software, electrical machines can be easily and effectively evaluated by FEA.

The research in this dissertation mainly focuses on the development of new design methods for SPM machines. Both design methods are integrated in a machine design platform called SyR-e, which is available online [34].

## 1.2 SyR-e

SyR-e stands for Synchronous Reluctance evolution. It is online since late 2014, as the summary of a research activity on automatic design of synchronous reluctance machines started in 2010. The core of SyR-e is the interaction between the Matlab (or Octave) and a 2D magnetic FEA client, FEMM [82]. This is made possible by the Octave-FEMM scripting library. The basic principle of operation of SyR-e is depicted in Fig. 1.2. SyR-e has a graphical user interface (GUI) where the user can organize its design very finely. SyR and PM assisted synchronous reluctance (PM-SyR) machines are covered. Since 2015, SPM machines are also included.

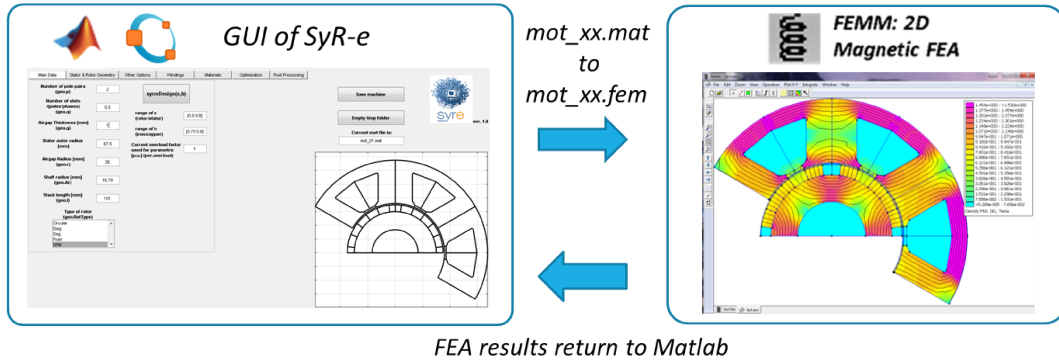


Fig. 1.2 SyR-e working principle

### 1.2.1 SyR-e Development

The automatic design method was firstly proposed in 2010. The design optimization of three-layer IPM motors by means of multi-objective genetic algorithm (MOGA) was introduced and tested in [83]. Maximum torque, minimum torque ripple and constant power speed range (CPSR) were selected as cost functions. A trade-off IPM machine was obtained, considering minimum torque ripple and magnet quantity. Then a position offset was proposed to decrease the number of

FEA simulations [84]. Rotor core losses were also added as another cost function during the optimization process.

An automatic design procedure for SyR machines was proposed in [85]. Two-step optimization flowchart was introduced, i.e. global search of multi-objective genetic optimization (GS-MOGA) and Local search MOGA refinement (LS-MOGA). Then one PM-assisted or IPM machine can be obtained from the optimized SyR motor by off-line definition of PM material and quantity. The two different rotor geometries are reported in Fig.1.3.

Two different segmented rotor flux barrier shapes for multi-layer SyR machines were studied in [86] by using automatic design procedure. The flux barrier shape was defined after two parameters, angular position  $\Delta\alpha$  and width  $hc$ . Later, one more degree of freedom  $\Delta x$  was added to define the radial position of flux barriers [87], shown in Fig.1.4. Considering both motor performance and computational time, the rotor definitions with six degrees of freedom of three-layer flux barrier had a better trade-off than the one with seven degrees of freedom (one more  $\Delta x$ , Fig.1.5). More degrees of freedom can improve the torque performance at cost of a longer computation and worse convergence in multi-objective differential evolution (MODE) process.

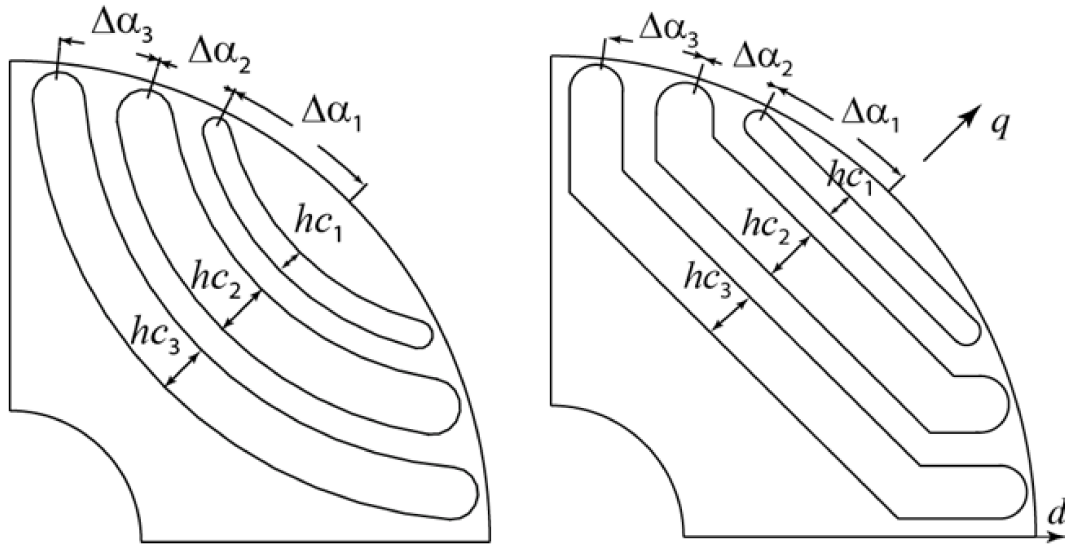
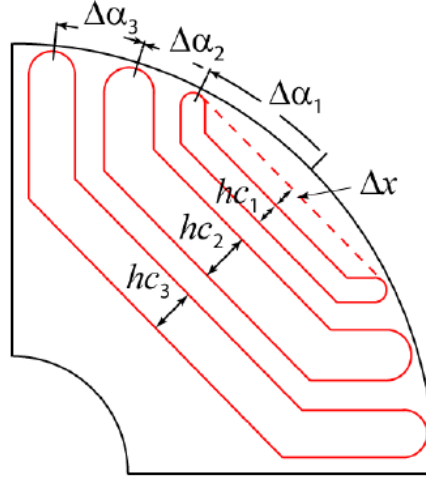
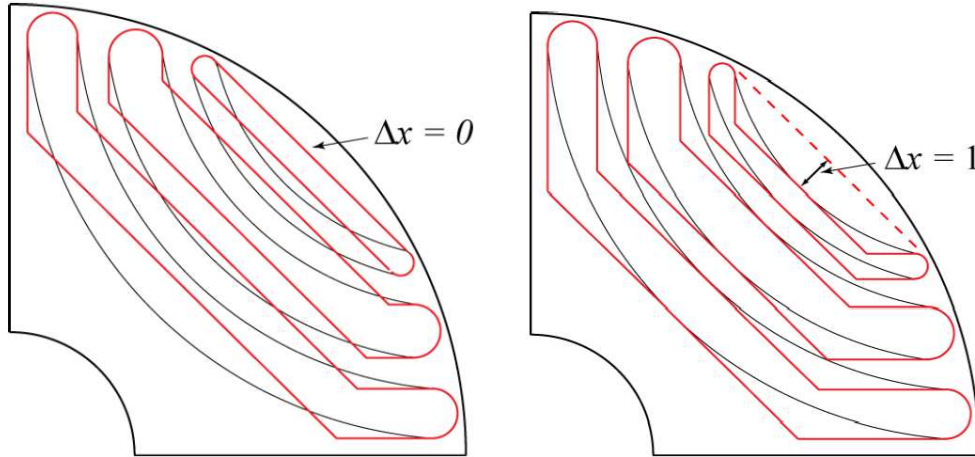


Fig. 1.3 SyR-e circular and segmented flux barriers definition

Fig. 1.4  $\Delta x$  definition for flux barriers

In [88, 89], a comprehensive research on multi-objective optimization algorithms (MOOAs) for automatic design of SyR motors was presented. Three MOOAs were analyzed and compared in terms of both motor performance and computational time. Compared with genetic algorithm (GA), simulated annealing (SA) means, differential evolution (DE) turns out to have the best results considering both convergence time and repeatability.

Fig. 1.5 Effect on  $\Delta x$ 

By applying MODE in automatic design process of SyR motors, the performance on combinations of stator slots and flux barrier numbers was studied [90].

A general design guideline was proposed in choosing optimal slots and barriers numbers to get best trade-off between the losses and torque ripple.

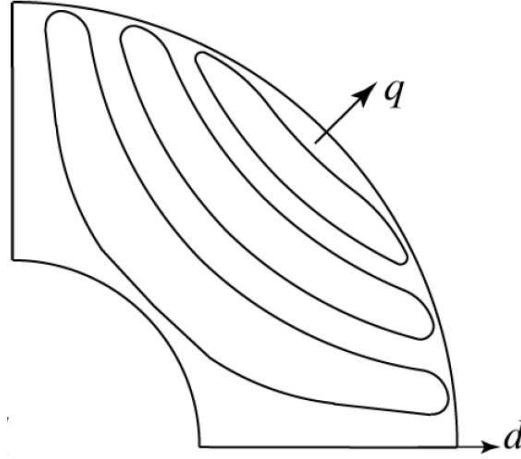


Fig. 1.6 Fluid barrier shape

Later, a new flux barrier shape called “fluid barrier” rotor geometry was introduced in [91]. Three degrees of freedom were used to define each barrier. The proposed rotor geometry 1.6 improved the torque performance, compared with “3U” shape SyR machines.

Considering stator winding configuration, a non-conventional fractional slot winding type was introduced [92]. The presented winding type made it more convenient to manufacture without losing torque and power characters, compared with the distributed windings. The traditional distributed winding (DW), concentrated winding (CW) and the non-conventional winding layouts in SyR-e are presented in Fig. 1.7.

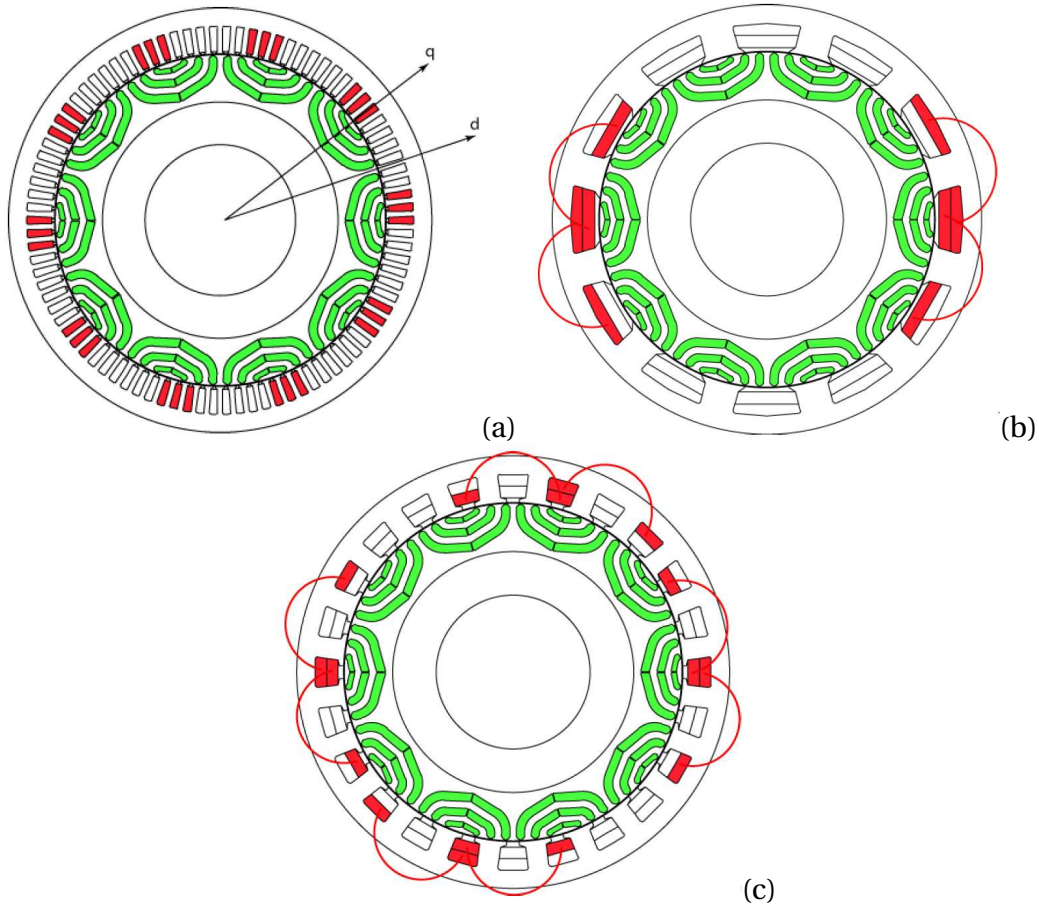


Fig. 1.7 Winding definition in SyR-e, (a) DW; (b) CW; (c) non-conventional fractional slot

Apart from electromagnetic performance, structural analysis was first introduced into SyR-e in [93]. The steel material effect on structural performance was studied. Two different lamination materials were studied and compared in both magnetic characteristics and yield strength. By means of MODE, FEA and multi-physics validations, the machine performance at high speed was demonstrated. Better efficiency can be obtained by a lower level steel material on magnetic performance when the machine was beyond a specific speed. To improve the structural robustness, the shape of end rotor barrier was optimized in [94]. Both electromagnetic and mechanical performances were studied.

In [95], a design method targeting on maximum power density at high speed for SyR machine was presented. It presented that the targeted SyR machine output power increased with rotational speed up to 70 krpm. Beyond the speed, the structural limit will in turn degrade the power performance.



In [96, 97], two design flowcharts for high speed SyR machine were reported. One simultaneous and the other separated magnetic-structural approach were both illustrated and validated respectively. Both methods got comparable torque and power performances with different structural layout. The separated approach (electromagnetic optimization was followed by mechanical optimization), can reduce the computing time.

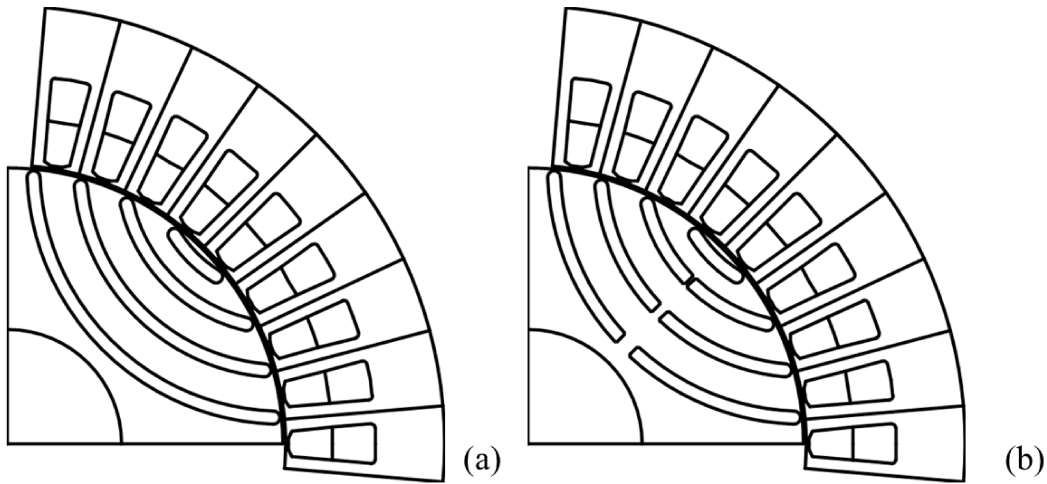


Fig. 1.8 Automatic design of additional radial bridges for different speed ratings. a) Max speed 3,000 rpm; b) Max speed 12,000 rpm

Then in [98], the effect of centrifugal stress on radial ribs in flux barriers was illustrated. Centrifugal stress at maximum speed was evaluated by SyR-e via simplified structural equations for each candidate design. If needed, additional radial bridges were automatically calculated and included in the barriers of PM-SyR rotors. The dimensions of the additional radial bridges were evaluated via the simplified structural model described in [94]. The higher the speed rating, the thicker such additional bridges will be, as represented in Fig. 1.8. Same as for the copper temperature estimation, also stress verification was seamless, in terms of computational time. In detail, off-line validation performed with static 2D finite element analysis (SolidWorks) showed that peak stress in the bridges is 333 MPa at 12,000 rpm. The margin to yield point is 455 MPa, corresponding to a maximum overspeed limit equal to 14,000 rpm with these bridges. Safety factor used in preliminary and end-of-line structural verifications was obtained pursuing 80 % of the material's yields strength, thus 20 % safety, or 25 % overspeed.

### 1.2.2 SyR-e Operation

The simpler operation that SyR-e can do is parametric FEA simulation and data collection. The user can define the design through the GUI and then run FEA simulations in FEMM [82]. Results of the simulations return to Matlab where they are processed to get to comprehensive characterization of the machine under test. Torque and flux maps, control trajectories including maximum torque per ampere and per volt (MTPA, MTPV) laws, flux weakening laws, efficiency maps can be evaluated with post processing scripts included in SyR-e. The main tab setting on machine type, stack size... is shown in Fig.1.9.

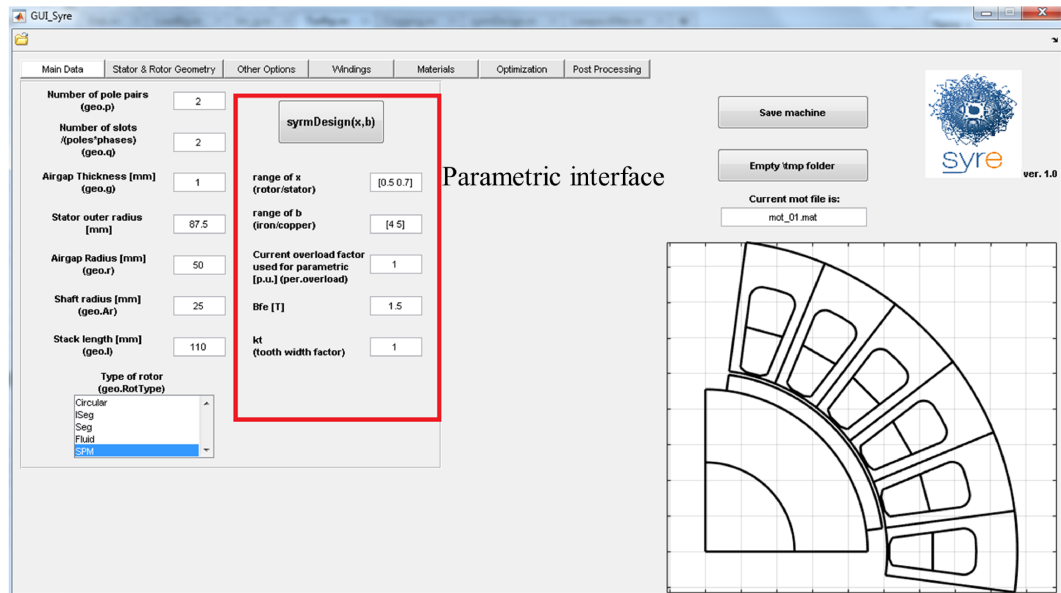


Fig. 1.9 SyR-e main dialog view

In addition, the design can be exported to other CADs for other types of evaluation. A second possible approach is to use the design equations integrated into SyR-e. This is possible for both the SyR and SPM machine types. The user can design the machine using the design equations in a parametric fashion, pick up a design from the plane of the parameters, and then verify its performance in FEMM. Design optimization is also included. The parametric window is emphasized in red area in Fig.1.9, which will be described in the next chapter.

A large set of geometric and non-geometric parameters can be optimized using MODE, using FEMM for fitness evaluation. Matlab supports parallel processing, so

that multiple instances of FEMM can be run in parallel to reduce simulation time by simply using the “parfor” command in place of the usual instruction “for”. The input setup window for automatic design is reported in Fig. 1.10. On the automatic panel, the generation and population size of optimization procedure can be set. The variables that participate in the process are magnet length, magnet span, magnet shape factor, magnet remanence, tooth length, tooth width, slot opening ratio, slot tangential width, airgap length and current angle. The optimization target can be the torque, torque ripple, copper quantity, flux weakening capability, etc.

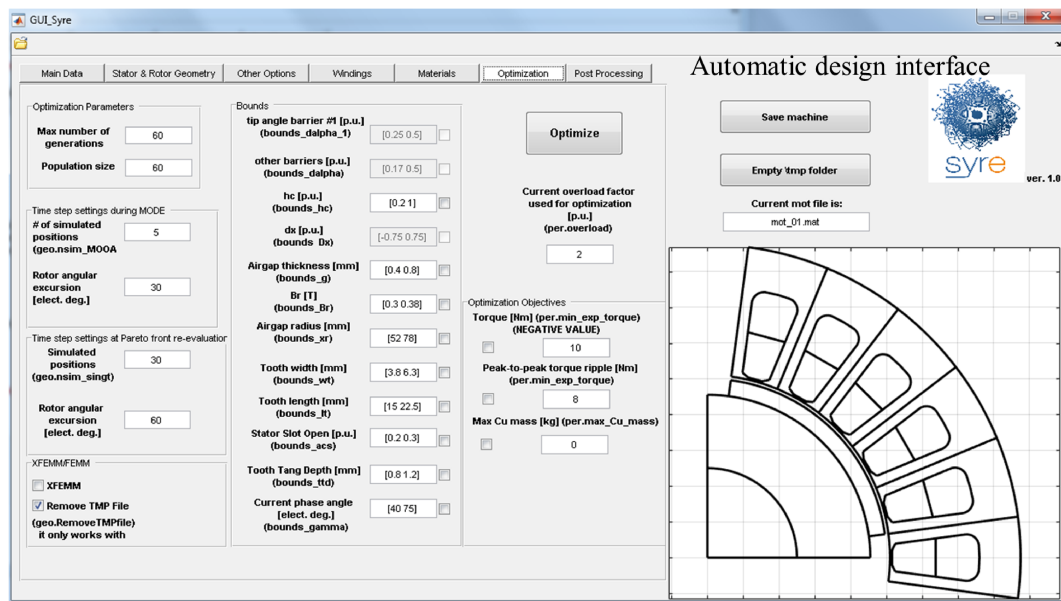


Fig. 1.10 SyR-e automatic design setup tab

Apart from that, a couple of non-magnetics aspects are covered, namely thermal and structural analysis. The steady-state temperature in the stator slot is estimated, for consistency of Joule loss evaluation given the specific current loading, and for the sake of thermal verification. Moreover, structural bridges of SyR rotors are calculated automatically according to the specified maximum rotor speed. The non magnetic part view is presented in Fig. 1.11.

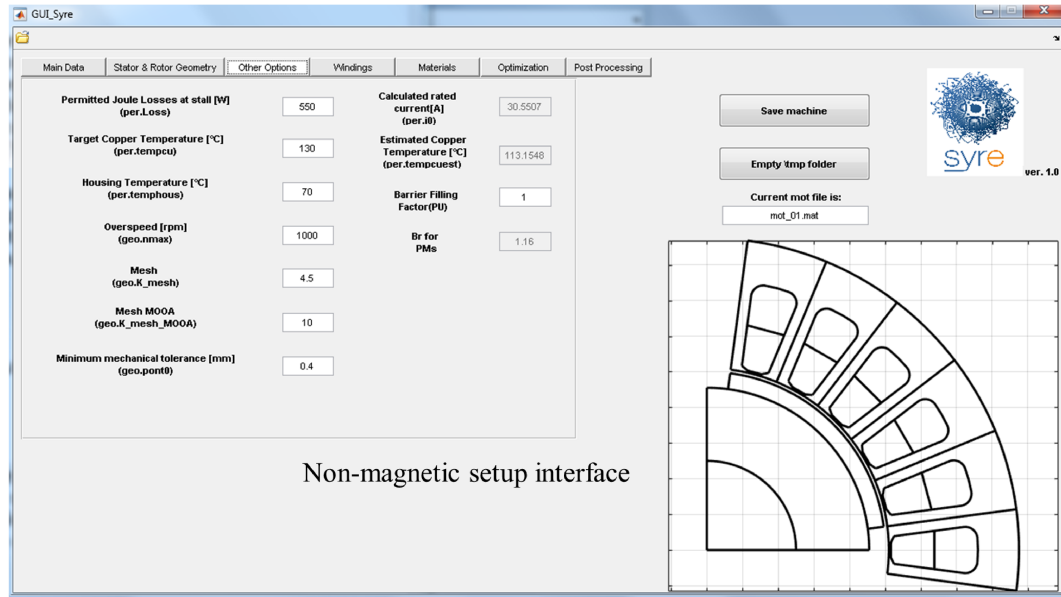


Fig. 1.11 SyR-e non-magnetic design view tab

### 1.3 Research Objectives

The goal of this research is to develop two effective design methods for SPM machines. The proposed methods are called automatic design procedure and parametric design procedure. Both design procedures are embedded in SyR-e.

The fundamentals of SPM machines are reviewed in Chapter 2, including the reviewed of magnet materials, the definition of airgap flux density, torque, power and winding configurations.

In Chapter 3, an automatic automatic design procedure through multi objective optimization method is presented. The automatic design procedure aims at obtaining the SPM machine capable of best trade-off among maximum torque, minimum torque ripple and cogging torque, minimum PM quantity, and good flux weakening capability. In this case, two design cases are reported by using automatic design. One is a SPM machine with concentrated windings (CW-SPM) for traction. The maximum torque and flux weakening capability are set as the two optimization goals. The losses, efficiency, thermal simulation under a specific driving condition and demagnetization issues are also discussed. The other case study is on a shaped SPM with distributed winding (DW-SPM). By targeting getting

minimum cogging torque and maximum torque at rated current, the automatic design is used to get optimum trade-off machine among the Pareto front. The torque and cogging torque performance are reported and validated by FEA.

Besides the automatic design procedure, a parametric design procedure is also introduced for SPM motors in Chapter 4. The development of the parametric design is illustrated in three successive steps. At the beginning, the parametric plane is established on the rotor split ratio and magnetic loading factor. Then in order to make the parametric plane more insightful, the rotor and magnet-airgap length factor are used in place of magnetic loading to build the design plane. After that, more accurate sizing equations are embedded into the design process by applying subdomain analytical model. The whole design development will be discussed in Chapter 4. For each stage, the detailed flowchart is presented. Design examples are also obtained and validated by FEA. A DW-SPM machine prototype is built and tested experimentally. The detailed experiment procedure and output is also illustrated.

The conclusion is presented in Chapter 5. In addition, the future research on SPM machine design is also discussed.

## **Chapter 2**

# **Surface-mounted Permanent Magnet Synchronous Machine**

### **2.1 Introduction**

In general, PM brushless machines are divided into two main parts: DC brushless machines (BLDC) and PMSMs. In this chapter, the main types of PMSMs are reviewed. Then the fundamentals of SPM machines are illustrated. Based on the winding configuration, the two dominant conventional types, distributed winding and concentrated winding, are described.

### **2.2 Permanent Magnet Synchronous Machine**

PMSMs can be an alternative for induction machine in industry since its higher torque, power density, and efficiency. Based on the relative positions of stator and rotor, two main categories are defined, i.e. inner rotor and outer rotor, respectively. In this section, several popular inner rotor types of PMSMs are addressed.

Depends on the arrangement ways of PMs on the rotor, several types of PMSMs are built. Some popular rotor configurations are reported in Fig. 2.1.

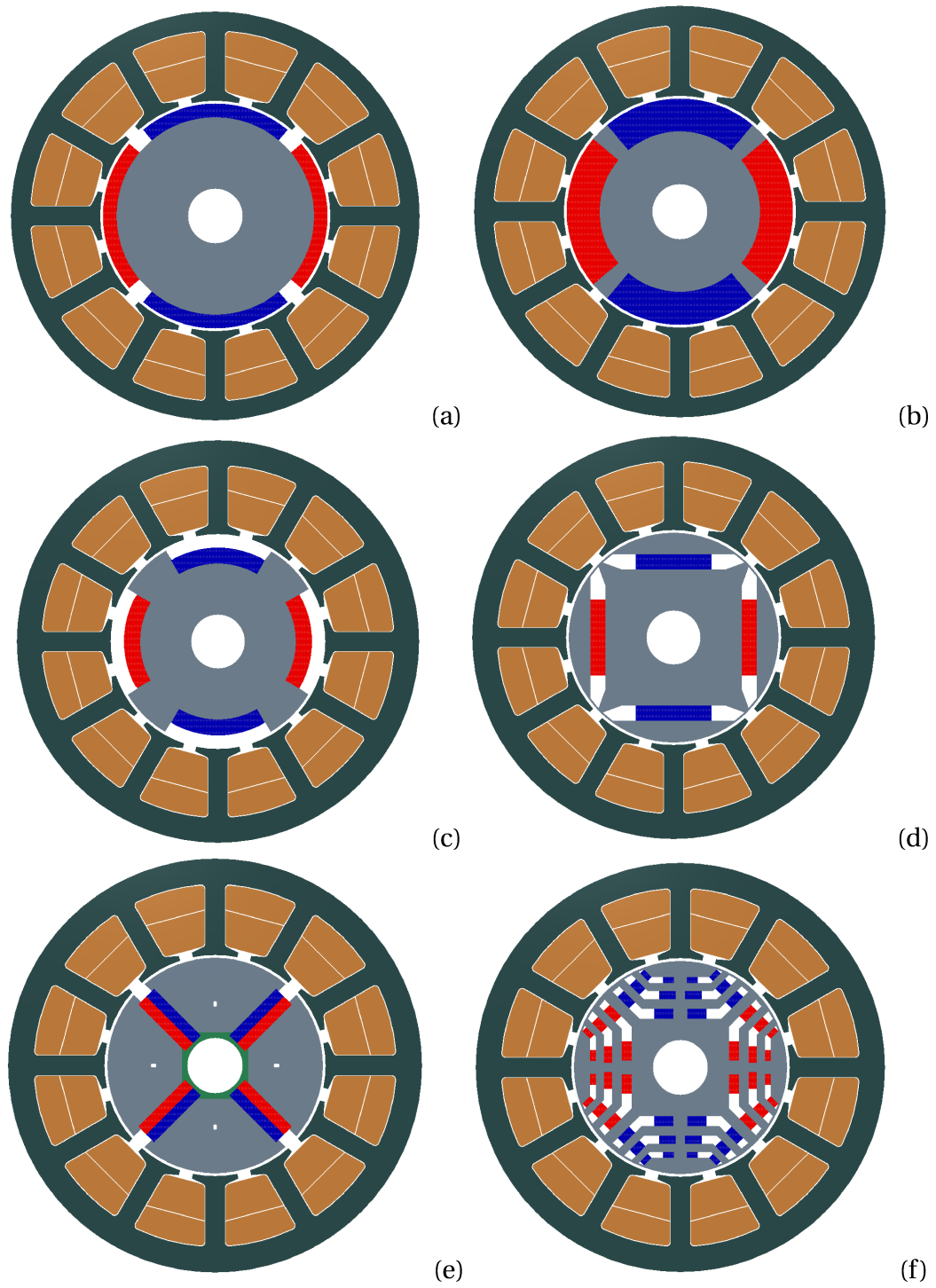


Fig. 2.1 Main rotor configurations of PMSMs

### 2.2.1 Surface-mounted Permanent Magnet Synchronous Machine

Surface-mounted permanent magnet synchronous machine is defined that the magnets are fixed on the rotor surface, shown in Fig. 2.1a. Since no geometry modification is needed in the rotor core, this rotor configuration is the simplest one among the PMSMs during the manufacturing process. With the help of PMs directly working at airgap interface, it produces the airgap flux density as high as possible [35–37].

Nonetheless, when the PMs are exposed directly at airgap, the demagnetization risk is increased, because the magneto-motive force (mmf) effect generated by stator current directly acts on the PMs [38, 39].

In terms of drives, the inductance variation between  $d$  and  $q$  is relatively small, there is no reluctance contribution to the torque production. The control of SPM machines is simplified. The details are described in the later sections.

### 2.2.2 Surface Inset Permanent Magnet Synchronous Machine

Fig. 2.1b presents a surface inset PM (SIPM) machine, which has a uniform cylindrical surface of the rotor. In this type of machine, the airgap length is constant along the rotor circumference. SIPM machines not only have reliable rotor structure than SPM machines, but also gains saliency effect due to the anisotropy between  $d$  and  $q$  axes. The saliency generates reluctance torque and hence, improves both the power density and constant speed range [40–42].

Except the uniform airgap length, unequal airgap length SIPM machine is introduced to obtain high saliency ratio. In this case, the airgap length at  $q$  axis is shorter than  $d$  axis. By this way,  $q$  -axis inductance  $L_q$  is increased while  $d$  -axis inductance  $L_d$  is reduced. therefore the saliency ratio  $L_q/L_d$  can be improved. Large reluctance torque and wide speed range are achieved. The relevant geometry is reported in Fig. 2.1c. Extended airgap length at  $d$  axis also can reduce the demagnetization risk because the mmf drop at airgap is increased [43].



### 2.2.3 Interior Permanent Magnet Synchronous Machine

Except surface PM rotor shapes, Fig. 2.1d-e report two interior PMSMs with the PMs embedded in the rotor lamination in radial and circumferential orientations, respectively. Compared with SPM and SIPM machines, interior PM (IPM) machines are mechanically robust and can be used in high speed applications. The radial type IPM machines (Fig. 2.1d) have flux barriers at rotor core. The flux barriers result in decreasing mutual flux linkages  $L_{dq}$  and  $L_{qd}$ . The weight of the rotor is also reduced thereby diminishing rotor inertia. The circumferential IPM rotor, also known as spoke type (Fig. 2.1e), can obtain higher airgap flux density. However, large quantity of PMs will increase the cost of the machine [44–46].

IPM machines significantly improves the saliency ratio when multi layers are used in the rotor (shown in Fig. 2.1f), [47–49]. Therefore, the flux weakening performance is better than SPM machines[36, 50]. On the other hand, the manufacturing becomes more complex.

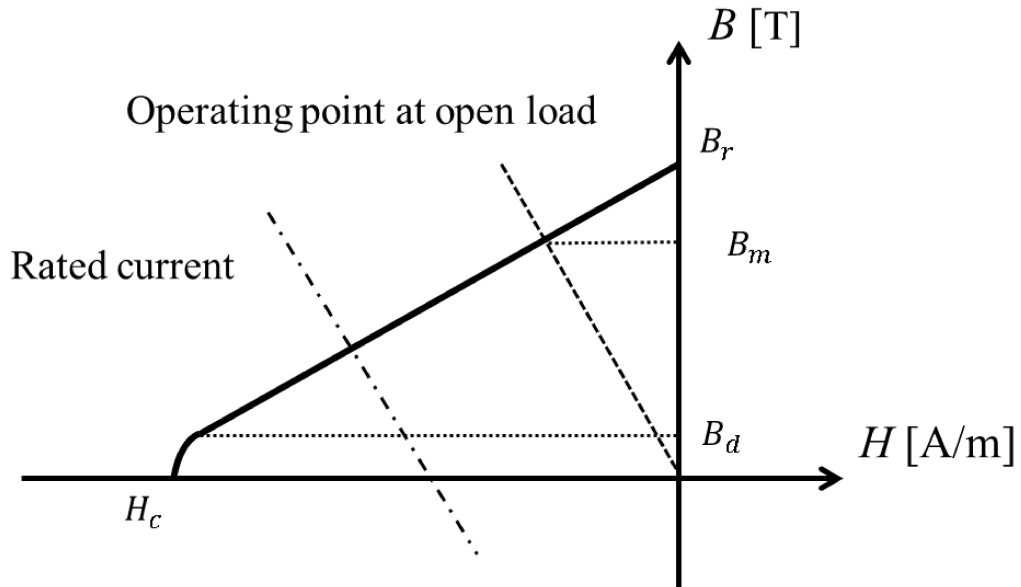
## 2.3 Fundamentals of SPM Machines

The fundamentals of SPM machines are reviewed in this section, including magnet material, airgap flux density, induced voltage(emf), Armature current density, torque, power and power factor (PF). The synchronous inductance of SPM machines is also calculated.

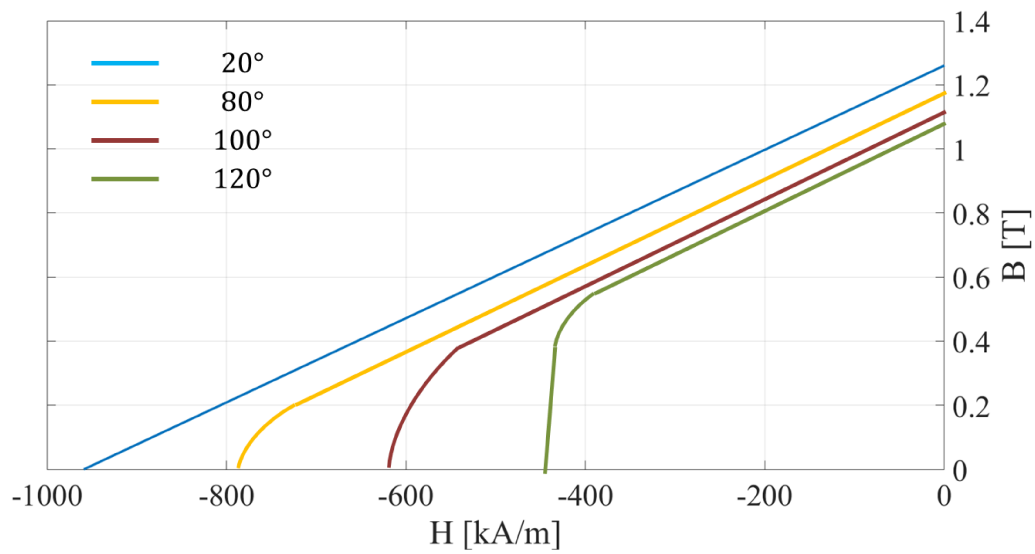
### 2.3.1 Permanent Magnet Material

Magnet materials were used in electrical machine since the middle of last century [51, 52]. The material characteristic has been rapidly developed since then by using rare-earth material. A typical demagnetization  $B-H$  characteristic of NdFeB PM, located at the second quadrant, is presented in Fig.2.2. The PM magnetic flux density is given as,

$$B_m = B_r + \mu_0 \cdot \mu_r \cdot H \quad (2.1)$$

Fig. 2.2  $B - H$  curve for a typical PM material

Where  $B_r$  is known as remanent flux density,  $\mu_0$  is the air permeability,  $\mu_r$  is the relative permeability of the magnet, and  $H$  is magnet field intensity. At open load condition, the magnet operating point is rounded  $B_m = 0.7 \sim 0.8B_r$ . When applied with current,  $B_m$  is influenced and moved along the demagnetization curve.

Fig. 2.3 Demagnetization curve for *BMN-38H*, *BOMATEC*

Besides the influence of armature current, both  $B_r$  and coercivity  $H_c$  of Neodymium magnets vary with the temperature. The demagnetization flux density  $B_d$  increases as the operating temperature grows up. While  $B_r$  drops notably instead [53, 54]. The demagnetization curves of *BMN-38H*, *BOMATEC* according to different temperatures are shown in Fig. 2.3.

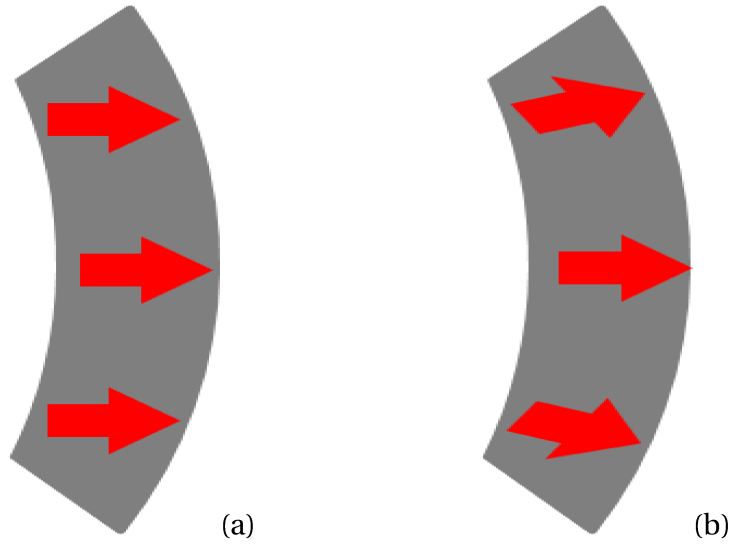


Fig. 2.4 Parallel (a) and radial (b) magnetization

PMs can be magnetized at specific orientation, including radial, parallel, and halbach array [55, 56]. The magnetization directions of two dominant arrangements, radial and parallel magnetizations are presented in Fig. 2.4. The relevant airgap flux density distributions  $B_g$  produced by magnet over one pole pair for slotless machines are shown in Fig. 2.5.

### 2.3.2 Airgap Flux Density

When the PMs are directly facing with the airgap, the airgap flux density is significantly referring to the magnet shape. The two main parameters relating to PM shape are magnet length  $l_m$  and magnet span  $\alpha_m$ . When the machine is slotless, the airgap flux density distribution  $B_g$  is uniform. The  $B_g$  waveforms for both parallel and radial magnetized SPM slotless machine are shown in Fig. 2.5, the tangential component of  $B_g$  is neglected.

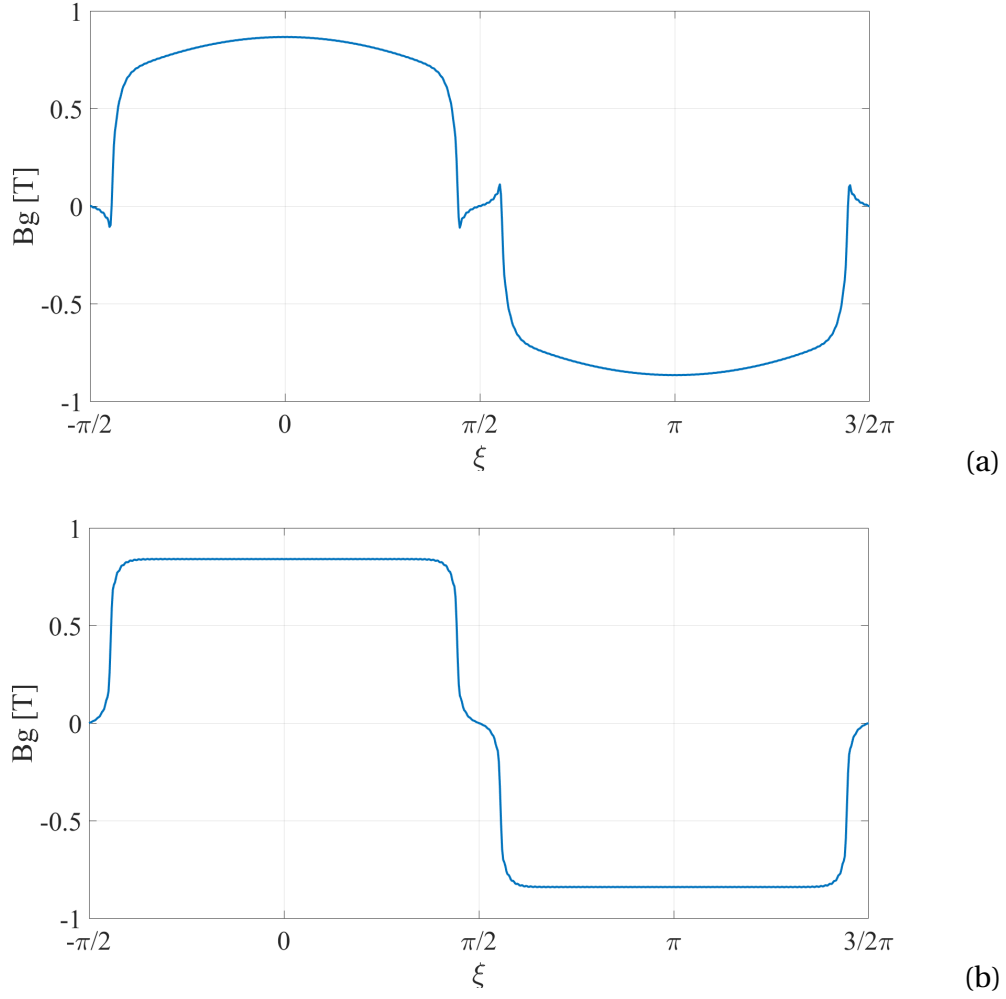


Fig. 2.5  $B_g$  waveform for slotless SPM machines, (a) parallel, (b) radial

However, due to the slot effect, the flux density always drops at the slot opening area. Then the average flux density  $B_{g\_avg}$  is reduced per pole [57, 4]. Carter coefficient  $k_c$  is introduced to calculate the reduction resulting from slot effect on  $B_{g\_avg}$ . The effective airgap length is increased by  $k_c$ ,

$$g' = k_c \cdot g \quad (2.2)$$

Here  $k_c$  is obtained by the slot opening width,

$$k_c = \frac{\tau_s}{\tau_s - \tau_s \cdot k_{so} \cdot \gamma'} \quad (2.3)$$

Where  $\tau_s$  is the slot pitch,  $k_{so}$  is the slot opening ratio in p.u. of  $\tau_s$ . The parameter definition is reported in Fig.2.6.  $\gamma'$  is given as [15],

$$\gamma' = \frac{2}{\pi} \cdot \left[ \arctan \frac{\tau_s \cdot k_{so}}{2g} - \frac{2g}{\tau_s \cdot k_{so}} \cdot \ln \sqrt{1 + \left( \frac{\tau_s \cdot k_{so}}{2g} \right)^2} \right] \quad (2.4)$$

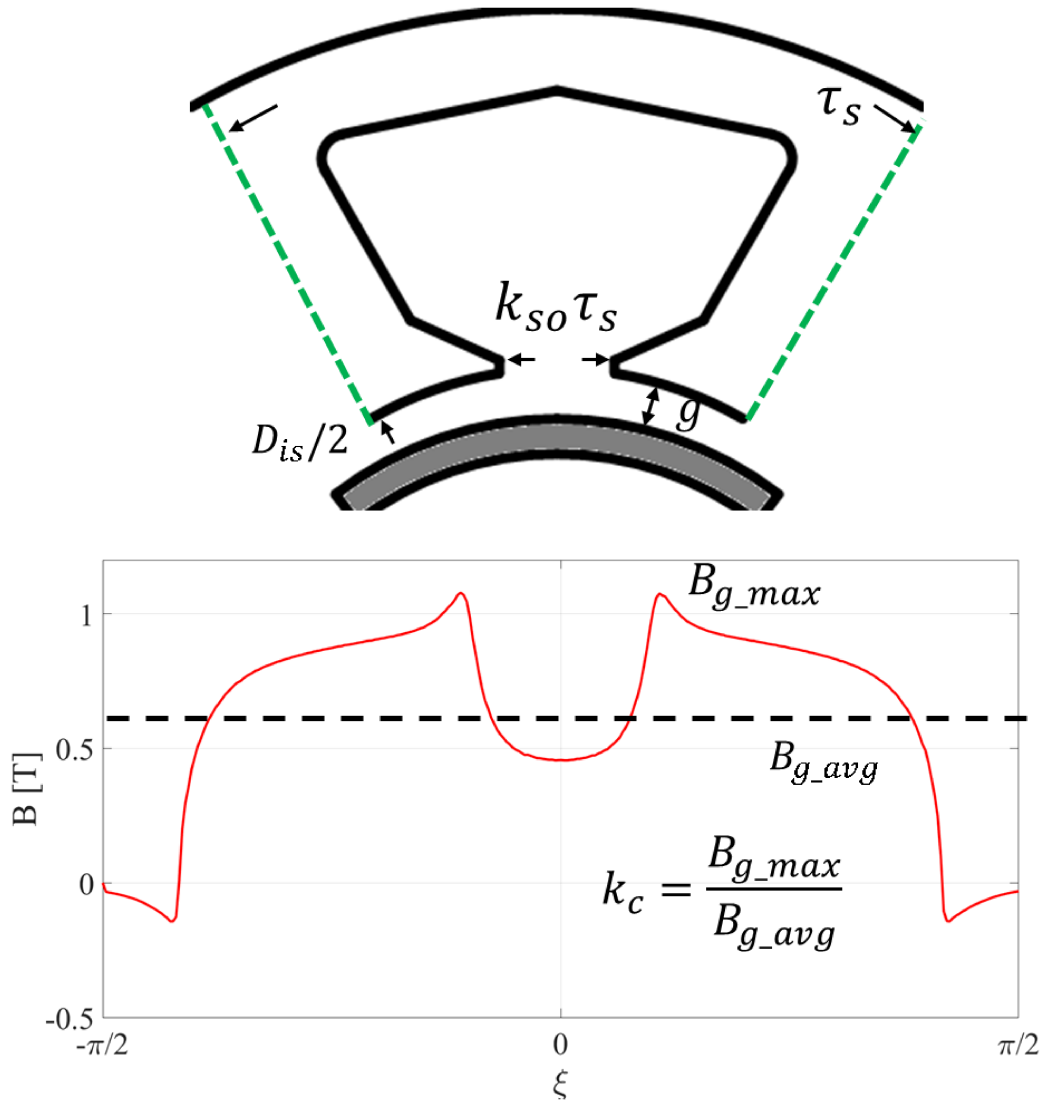


Fig. 2.6 Slot view and  $B_g$  waveform

Here the slot pitch  $\tau_s$  is calculated from

$$\tau_s = \frac{\pi \cdot D_{is}}{6 \cdot p \cdot q} \quad (2.5)$$

Where  $D_{is}$  is the stator inner diameter,  $p$  is the number of pole pairs, and  $q$  is the number of slots per pole per phase. In addition, the Carter coefficient is also defined as the ratio of the maximum flux density  $B_{g\_max}$  to the average flux density  $B_{g\_avg}$  [58, 59],

$$k_c = \frac{B_{g\_max}}{B_{g\_avg}} \quad (2.6)$$

By introducing  $k_c$  to account for  $B_g$  reduction on slot effect, then  $B_{g\_avg}$  is calculated as,

$$B_{g\_avg} = \frac{l_m}{l_m + g \cdot \mu_r \cdot k_c} \quad (2.7)$$

From the equation above, It shows that the magnet length  $l_m$  has a significant effect on the magnitude of  $B_g$ , when  $g$  is invariable.  $B_{g\_avg}$  results calculated from (2.7) and FEA results are shown in Fig. 2.7. In the calculation, the airgap length  $g = 1\text{ mm}$  as a reference value.

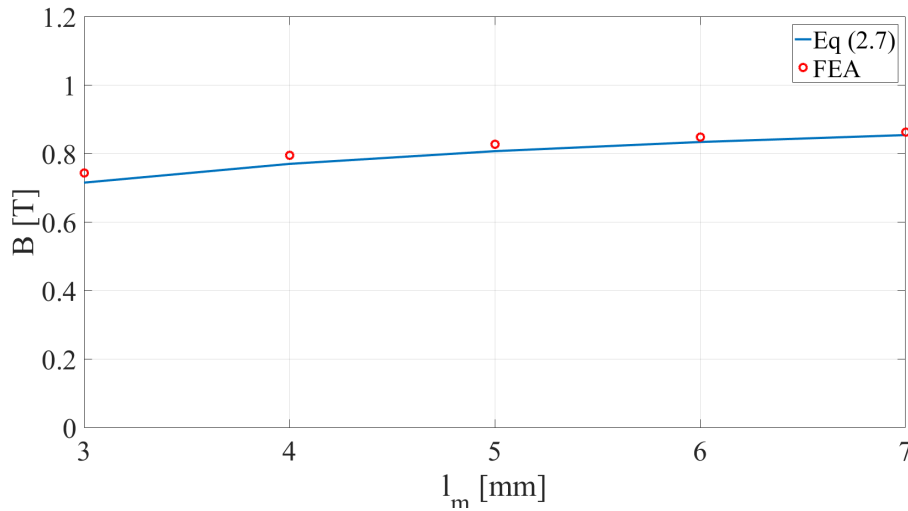


Fig. 2.7  $B_{g\_avg}$  results comparison between (2.7) and FEA

### 2.3.3 Induced emf

The thickness and angular span of PMs play a key role in the induced emf in stator winding. Considering the magnet span over one pole is  $\alpha_m$  in radians, the the peak of its fundamental component flux density is,

$$B_{m1} = \frac{4}{\pi} \cdot B_m \cdot \sin \frac{\alpha_m}{2} \quad (2.8)$$

The waveforms of relevant magnet flux densities is shown in Fig. 2.8.

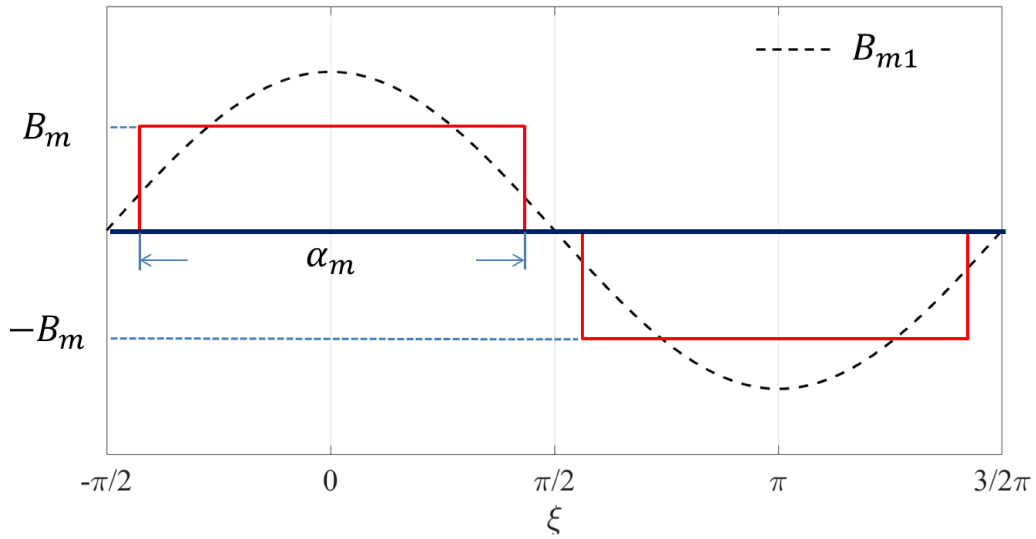


Fig. 2.8  $B_m$  and  $B_{m1}$  waveform over one pole pair

Then the peak of induced emf is calculated as,

$$E_m = \sqrt{2}\pi \cdot N_s \cdot k_w \cdot f \cdot \Phi_{m1} \quad (2.9)$$

where  $N_s$  is the number of turns per phase,  $k_w$  is the winding factor,  $f$  is the rotational frequency, and  $\Phi_{m1}$  is the peak fundamental flux in the airgap, which is given by,

$$\Phi_{m1} = B_{m1} \cdot D_{is} \cdot L / p \quad (2.10)$$

Here  $L$  is the machine length. Substituting (2.10) into (2.9), then the induced emf can be achieved as,

$$E_m = \frac{4}{\pi} \cdot k_w \cdot N_s \cdot D_{is} \cdot B_m \cdot \omega_m \cdot \sin \frac{\alpha_m}{2} \quad (2.11)$$

Where  $\omega_m$  is the mechanical angular speed of the machine.

### 2.3.4 Torque and Power

The electromagnetic torque of PMSMs has one magnet component and one reluctance component,

$$T = \frac{3}{2} \cdot p [\lambda_m \cdot i_q + (L_d - L_q) \cdot i_d \cdot i_q] \quad (2.12)$$

Where  $i_d$  and  $i_q$  are the current in  $d$  and  $q$  axis respectively.  $\lambda_m$  is the PM flux linkage. The second portion (term with  $L_d - L_q$ ) is the reluctance contribution, which is none in the SPM case, since the inductance  $L_d$  and  $L_q$  are identical. Normally, the current of SPM machines is fixed on  $q$  axis at low load condition. Then (2.12) is modified as,

$$T = \frac{3}{2} \cdot p \cdot \lambda_m \cdot i_q \quad (2.13)$$

$\lambda_m$  is achieved by

$$\lambda_m = \tau_p \cdot L \cdot k_w \cdot N_s \cdot B_{g1} \quad (2.14)$$

$\tau_p$  is the pole pitch, and calculated as,

$$\tau_p = \frac{D_{is} \cdot \pi}{2p} \quad (2.15)$$

From (2.13), the torque is in proportional to the PM flux linkage and the machine current. Then the output power is obtained as,

$$P = T \cdot \omega_m \quad (2.16)$$



### 2.3.5 Maximum Current Limit

While fed with stator current on  $q$  axis, the PM flux density  $B_m$  increases on the leading edge of the magnet and drops on the opposite edge. The maximum mmf on the airgap derived from stator current is [16, 60],

$$F_{p1} = \frac{3}{2} \frac{4}{\pi} \frac{k_w \cdot N_s}{2p} \cdot I_s \quad (2.17)$$

The peak flux density  $B_{g,I_s}$  produced by phase current acting alone is

$$B_{g,I_s} = \frac{3}{2} \frac{4}{\pi} \frac{\mu_0 \cdot k_w \cdot N_s}{2p \cdot \mu_r \cdot k_c \cdot g} \cdot I_s \quad (2.18)$$

To prevent demagnetization at any current angle, the operating magnet flux density must be more than the knee point  $B_d$ :

$$B_m - B_{g,I_s} \geq B_d \quad (2.19)$$

Where  $B_m$  is the PM flux density at open load condition. Combining (2.7), (2.18) and (2.19), the maximum allowed current is calculated,

$$I_{max} = \frac{2p\pi}{6\mu_0 \cdot k_w \cdot N_s} \cdot (B_r \cdot l_m - B_d \cdot g') \quad (2.20)$$

### 2.3.6 Synchronous Inductance

The inductance of the isotropic synchronous machine consists of magnetizing inductance  $L_m$ , slot leakage inductance  $L_s$ , tooth tip inductance  $L_{tip}$ , and end winding leakage inductance. In 2D FEA simulation, end winding effect is neglected. The calculation on  $L_m$ ,  $L_s$  and  $L_{tip}$  are illustrated in this section.

#### 2.3.6.1 Magnetizing Inductance

The PM flux linkage  $\lambda_m$  is shown in (2.14) at no load condition. Similarly, when the machine is fed with current, the current flux linkage is obtained [61, 62],

$$\lambda_{ms} = \tau_p \cdot L \cdot k_w \cdot N_s \cdot B_{g,Is} \quad (2.21)$$

Substituting (2.18) into (2.21), the current flux linkage is,

$$\lambda_{ms} = \tau_p \cdot L \cdot \frac{3}{2} \frac{4}{\pi} \frac{\mu_0 \cdot (k_w N_s)^2}{2p \cdot \mu_r \cdot k_c \cdot g} \cdot I_s \quad (2.22)$$

Then the magnetizing inductance is given by

$$L_m = \frac{\lambda_{ms}}{I_s} = \frac{12}{\pi} \left( \frac{k_w N_s}{2p} \right)^2 \mu_0 \cdot \frac{D_{is} \cdot L}{k_c \cdot \mu_r \cdot g} \quad (2.23)$$

### 2.3.6.2 Slot Leakage Inductance

Except passing through the steel, the flux also circulates in the slot area, which is called the slot leakage flux [63, 64].  $L_s$  results from the leakage flux entering the slot. A simplified slot view is reported in Fig.2.9.

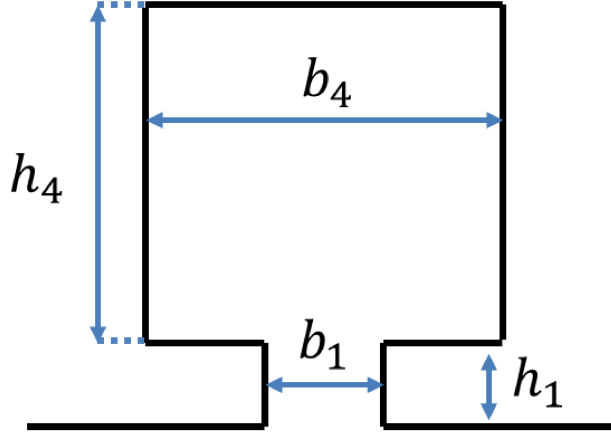


Fig. 2.9 A simplified slot view

For the slot area, the magnetic permeance factor of the simplified slot is defined as,

$$\sigma_4 = \frac{h_4}{3b_4} \quad (2.24)$$

Here  $h_4$  is the slot length,  $b_4$  is the slot width. In terms of slot opening region, the magnetic permeance factor is,

$$\sigma_1 = \frac{h_1}{b_1} \quad (2.25)$$

Where  $h_1$  is the slot opening height,  $b_1$  is the slot opening width. Then the slot inductance  $L_s$  is obtained,

$$L_s = \frac{12}{6 \cdot p \cdot q} \cdot \mu_0 \cdot L \cdot N_s^2 \cdot (\sigma_1 + \sigma_4) \quad (2.26)$$

### 2.3.6.3 Tooth Tip Leakage Inductance

The tooth tip leakage inductance is decided by the magnitude of leakage flux flowing in the airgap outside the slot opening region [4, 65, 66]. The tooth tip leakage inductance  $L_t$  is decided by another permeance factor;

$$k_t = \sigma_t \cdot \frac{5 \left( \frac{g'}{b_1} \right)}{5 + 4 \left( \frac{g'}{b_1} \right)} \quad (2.27)$$

Where  $\sigma_t$  is a factor referring to the arrangement of coils. Then  $L_t$  is achieved as,

$$L_t = \frac{12}{6 \cdot p \cdot q} \cdot k_t \cdot \mu_0 \cdot L \cdot N_s^2 \quad (2.28)$$

## 2.4 Windings

The torque of PMSMs is produced by the interaction between a PM flux and a stator mmf, which is generated from armature current in PMSMs. The current frequency is synchronized to the rotor electrical frequency. The mmf resulting from one coil concentrated is rectangular distribution along the relevant slots where the two coil sides locate. However, the harmonic content is abundant in rectangular mmf distribution. Additional losses rather than excess torque are produced by the mmf harmonics. Therefore, minimizing the stator mmf harmonics is a key factor to

improve torque and efficiency performance. Two dominant layouts are used, i.e. distributed winding and concentrated winding.

### 2.4.1 Distributed Windings

For DW machine, the number of slot per pole per phase  $q$  is greater than one and the coil span is constant for each coil. A two-layer DW-SPM with four-pole and 24-slot ( $p = 2, q = 2$ ) is shown in Fig. 2.10 Considering current mmfs from the two adjacent coils in the same phase are  $E_1$  and  $E_2$  respectively, the total voltage induced by this phase current can be obtained by the phasor diagram below.

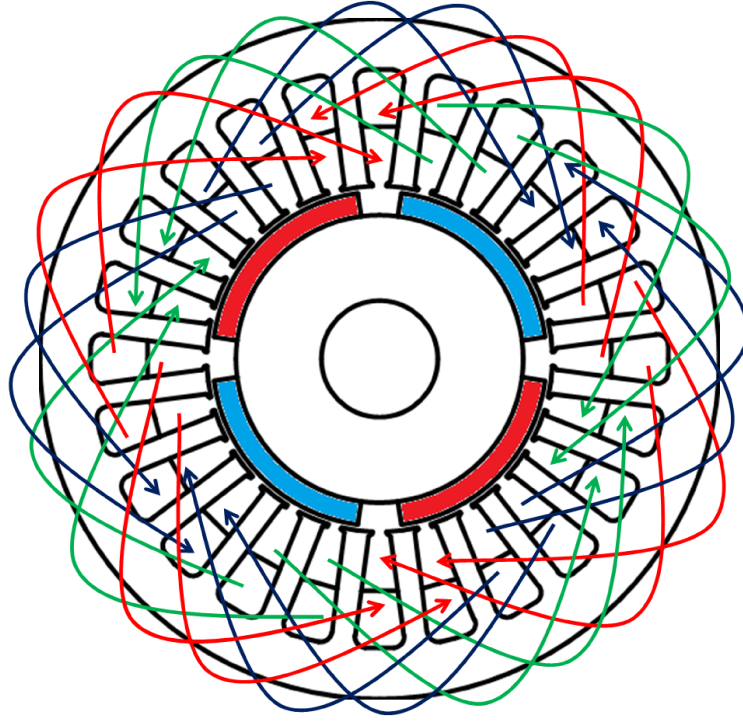


Fig. 2.10 Winding configuration of DW-SPM with  $p = q = 2$

The distribution factor is defined as the ratio between the magnitude of  $E_a$  and the algebraic sum of coil mmf  $E_1 + E_2$ ,

$$k_d = \frac{\sin\left(\frac{q \cdot \alpha_s}{2}\right)}{q \cdot \sin\left(\frac{\alpha_s}{2}\right)} \quad (2.29)$$

Here  $\alpha_s$  is the slot pitch angle in electrical degree.

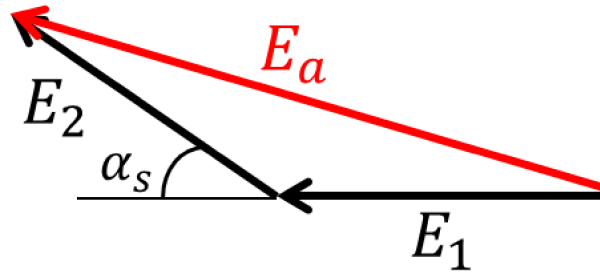


Fig. 2.11 Effect of winding distribution

In analysis above, the coil span is considered as same as the pole pitch. If the coil span is less than the pole pitch, the resultant mmf is decreased by another pitch factor  $k_p$ , which is defined as,

$$k_q = \sin\left(\frac{\delta}{2}\right) \quad (2.30)$$

Where  $\delta$  is the coil span in electrical degrees, shown in Fig. 2.12 The short pitching can benefit in both diminishing harmonic contents and reducing the end turn length. Furthermore, the copper quantity and resistive losses are decreased.

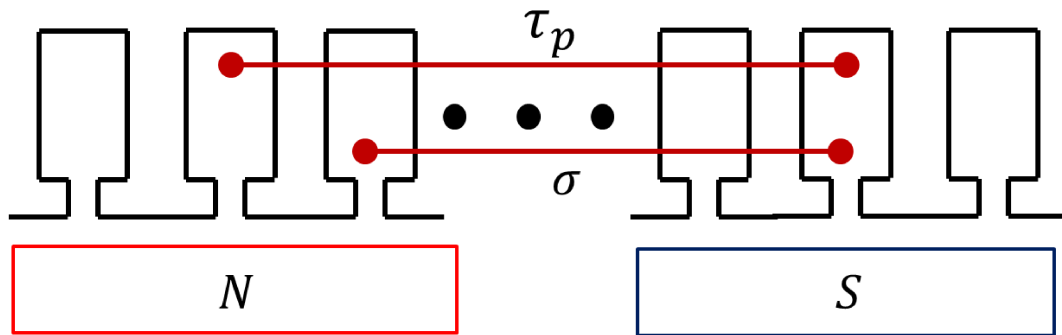


Fig. 2.12 Short pitching of a coil

In addition, the stator skewing along axial length is an effective method to eliminate both cogging torque and mmf harmonics. The stator is normally skewed over a slot pitch angle  $\delta_{sk}$ , shown in Fig. 2.13. However, the skewing in return degrades the mmf product by a skewing factor, which is given as,

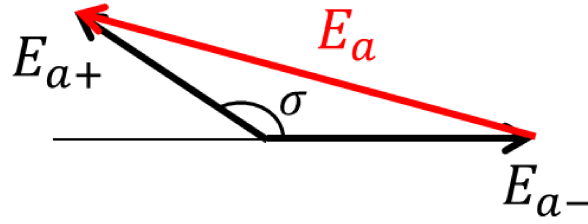


Fig. 2.13 Phasor of short pitching

$$k_{sk} = \frac{\sin(\frac{\delta_{sk}}{2})}{(\frac{\delta_{sk}}{2})} \quad (2.31)$$

Where  $\delta_{sk}$  the the skewing angle of the slot, defined in Fig. 2.14

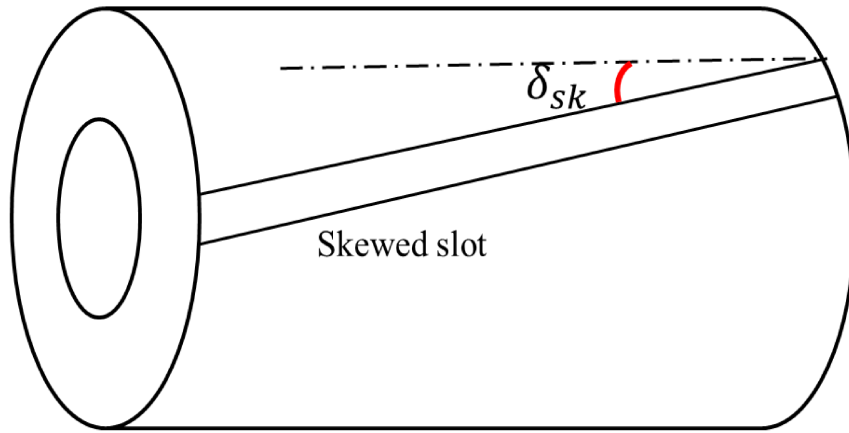


Fig. 2.14 Slot skewing

Overall, the effect on mmf is contributed together by  $k_d$ ,  $k_p$  and  $k_{sk}$ . Then the total winding factor is obtained as

$$k_w = k_d \cdot k_p \cdot k_{sk} \quad (2.32)$$

### 2.4.2 Concentrated Windings

PMSMs with concentrated windings have been studied and developed over the last two decades. CW can improve high power density, high efficiency, high slot

fill factor and short end turns [67]. In addition, low cogging torque, good flux-weakening capability and fault tolerance can be also achieved [68].

Two kinds of CW-SPM machines are shown in Fig. 2.15, one is single-layer with alternate teeth occupied, and other is double-layer with all teeth occupied.

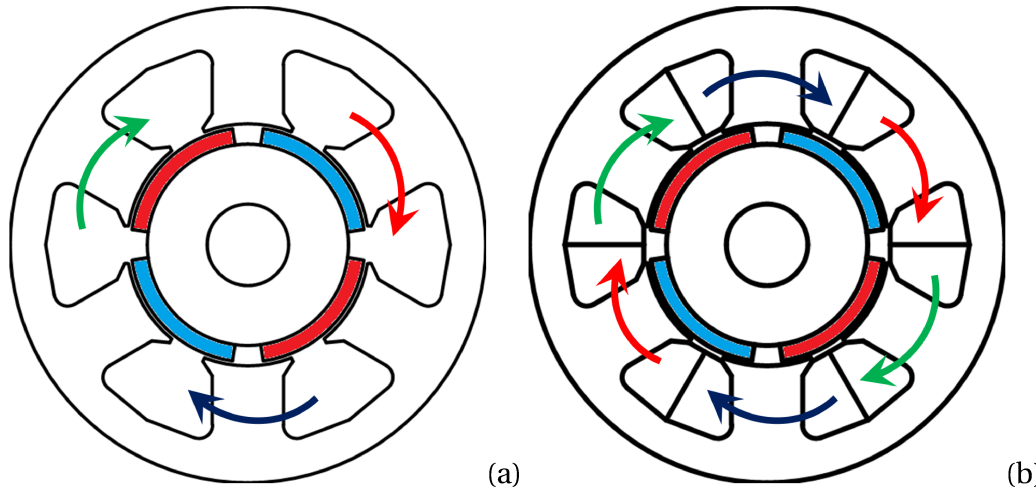


Fig. 2.15 Winding views of three-phase CW-SPM machines, (a) single-layer; (b) double-layer

A design approach to get optimal flux weakening capability in CW-SPM machines was illustrated in [69, 70], since the CW can highly increase the slot inductance to meet the characteristic current condition. A design procedure for CW-SPM machines with both single and double layers is presented in [71, 72]. The detailed mmf distribution and torque performance were analyzed. The instruction to get suitable slot and pole combinations was studied in [73]. The machine pole number, diameter-length ratio, number of winding layers and magnet type effects were presented in [74, 75]. The winding inductance was thoroughly presented in [76]. A method for decreasing airgap flux density subharmonics by using magnetic flux barriers in stator yoke was shown in [77]. For traction application, a design optimization method of CW-SPM machines based on NEDC was presented in [37]. To reduce mmf subharmonics, a new nonconventional winding with  $q = 3/5$  was addressed in [78]. Lower rotor losses can also be obtained for CW-SPM machines. An analytical calculation of the slot leakage inductance in CW-SPM machine for four-layer windings was presented in [79].

## **Chapter 3**

# **Automatic Design Using Optimization Algorithms**

This chapter mainly illustrates the automatic design process for SPM machines by using multi-objective optimization algorithm. Two design cases are described, one for traction application using the CW-SPM machine and the other for DW-SPM machine capable of low cogging torque.

In terms of traction application, the optimization targets are the maximum torque and flux weakening capability. For the DW-SPM machine case, the targets are set as the cogging and rated torque performance.

### **3.1 Automatic Design for Traction Application**

Part of the work described in this chapter has been previously published in [98].

#### **3.1.1 Design Background**

Electrical machines design is a complex, multi-objective engineering challenge whose typical goals are maximizing the output torque, minimizing losses, mass, cost, torque ripple, etc... Magnetic aspects play the central role in the design, but many other non-secondary aspects make this a multi-physical problem and a kaleidoscopic challenge. Recent efficiency standards [99] demand for accurate



loss evaluation and thermal-magnetic co-design. Today's demanding applications like the more electric aircraft [100] or vehicle powertrains [101–103] ask for high compactness, transient operation in a variety of operating points, and high efficiency in all operating conditions. A number of non-magnetic aspects must be taken into account, such as structural co-design for high-speed operation [104, 105], sustainable iron and PM losses [106], flux weakening capability, transient overload capability, and high efficiency in a large operating region [107], as said. The multi-objective design problem is thus becoming complicated more and more. Fortunately, the growing complexity of application requirements is backed by an even stronger growth of artificial intelligence and available computational resources. This case study illustrates an automatic design procedure for CW-SPM machines, integrated in a machine design environment SyR-e, linked with FEA engine FEMM.

The traction machine of an electric vehicle (EV) is one of the most challenging application design wise. Its mission contains a multitude of transient operating points, defined by the different possible driving cycles of the vehicle. The PMSMs applied to EVs are the CW-SPM machines and the IPM machines. Previous work compared CW-SPM and IPM machines to the IM in EV application [36]. This study uses the traction machines presented in [36] as the benchmark for two new designs made in SyR-e. The machine considered here is the CW-SPM machine. The automatic design procedure, based on MODE and FEA, for the sake of accurate performance evaluation [87, 108]. After the design part, both machines are FEA characterized in detail, including the study of iron and PM losses, the determination of the control trajectories like the MTPA law and the flux-weakening law. The limits of the torque – speed envelope given the power converter will be put in evidence, alongside calculated efficiency maps, as final performance indicators against the reference machines of [36]. All operations presented in the study can be repeated by the reader using online resources of SyR-e, with the only exception of iron and PM loss evaluation, for now delegated to commercial software [109]. The main contributions of this study are:

- 1) to provide comprehensive design procedures for CW-SPM machines for traction, where most of key aspects are taken into account.

2) Such design strategies take advantage of shortcuts purposely intended for traction machines, such as the goal function that summarizes flux weakening capability in one FEA simulation.

3) The consequence of 2) is that no extensive optimization covering multiple operating points in the torque versus speed plane was required to obtain satisfactory performance and high efficiency.

### 3.1.2 Design Conditions for Traction Machines

When dealing with a vehicle powertrain, it is not easy to extract a single operating condition as the only reference for magnetic and thermal design. The typical torque versus speed envelope of an EV traction drive is reported in Fig. 3.1. It has a large constant power speed range, dictated by the power converter and battery limits. Besides maximizing torque at low speed, the designer must fulfill the power target at maximum speed, in flux weakening operation. Two key design points summarize the magnetic design:

- Point U (110 Nm, 4,000 rpm, stands for up-hill) in Fig.3.1 represents worst case climbing conditions.
- Point F (39 kW, 12,000 rpm, stands for flat) represents the power required to run the vehicle at its maximum speed.

Both design conditions refer to quasi-continuous operation, intending that both situations can be prolonged in time for more than one thermal time constant, even if this is not strictly specified by driving cycle used for this vehicle (NEDC: new European driving cycle [110]). Point U defines the rated torque, whereas point F defines the flux weakening speed range of the drive.

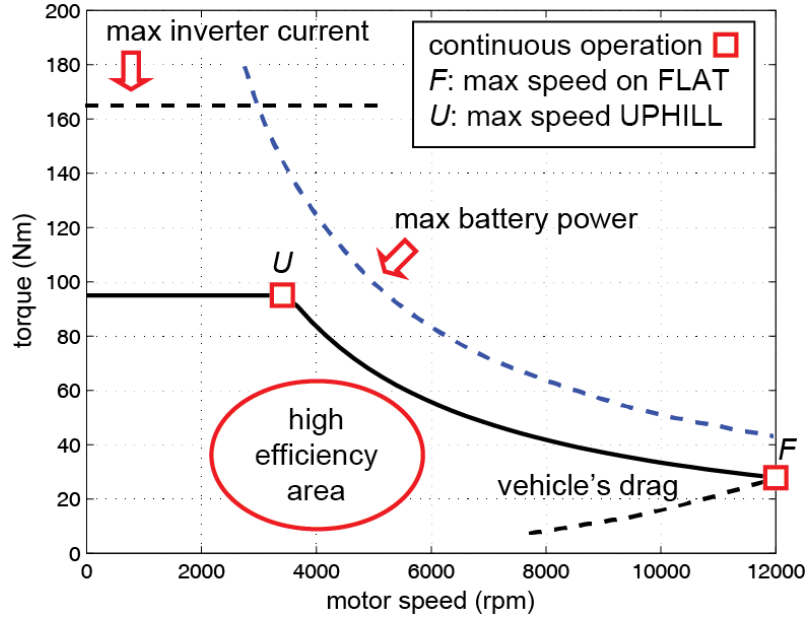


Fig. 3.1 Torque versus speed requirements of an electric vehicle

The steady state model of a PMSM is briefly reviewed:

$$v_{dq} = R_s i_{dq} + j\omega \lambda_{dq} \quad (3.1)$$

$$\lambda_{dq} = \begin{bmatrix} L_d & 0 \\ 0 & L_q \end{bmatrix} \cdot i_{dq} + \begin{bmatrix} \lambda_m \\ 0 \end{bmatrix} \quad (3.2)$$

Where  $v_{dq}$ ,  $i_{dq}$  and  $\lambda_{dq}$  respectively are the voltage, current and flux linkage vectors in rotor coordinates  $dq$ ,  $R_s$  is the phase resistance, and  $\omega$  is the rotor speed in electrical degree [rad/s]. The electromagnetic torque (2.13) has only one magnet component  $\lambda_m$ .

**Target torque is defined after point U. Point F dictates that flux weakening capability is sufficient. It means that the machine is able to reach the required power at maximum speed under maximum voltage constraint.** A powerful metric of flux weakening capability of a PMSM is its characteristic current:

$$i_{ch} = \frac{\lambda_m}{L_d} \quad (3.3)$$

At current level (3.3), the armature flux can cancel the magnet flux, if the current vector is aligned against the magnet direction. Fig. 3.2 reports the vector diagram of CW-SPM machines operating at their characteristic current. Starting from the respective MTPA conditions, i.e. from full torque and full flux, flux weakening is applied via rotation of the current vector (dashed trajectories), eventually ending into zero flux conditions (red circle in Fig. 3.2). Neglecting losses, the power versus speed curve of both such CW-SPM machines is asymptotically flat Fig. 3.3, with a plateau called the characteristic power:

$$P_{ch} = \frac{3}{2} \cdot V_{max} \cdot i_{ch} \quad (3.4)$$

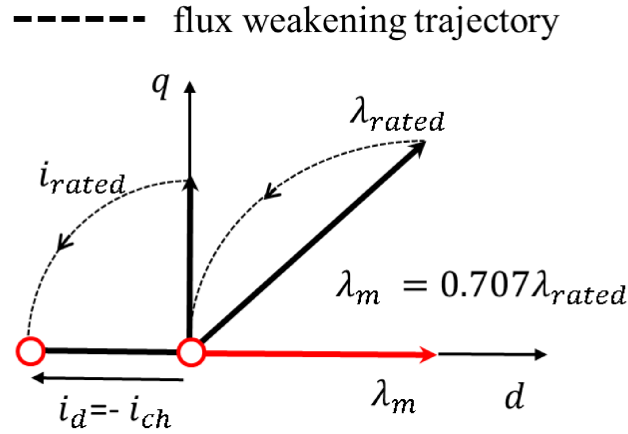


Fig. 3.2 Vector diagram of CW-SPM machines supplied at their characteristic current

### 3.1.3 Design Flowchart

This study considers one CW-SPM machine:

- having the characteristic power equal to rated power at maximum speed.
- enough torque at low speed to fulfill design condition U.

To do so, the two design conditions U and F will be merged into a single optimization, with automatic methodology for the CW-SPM machine.

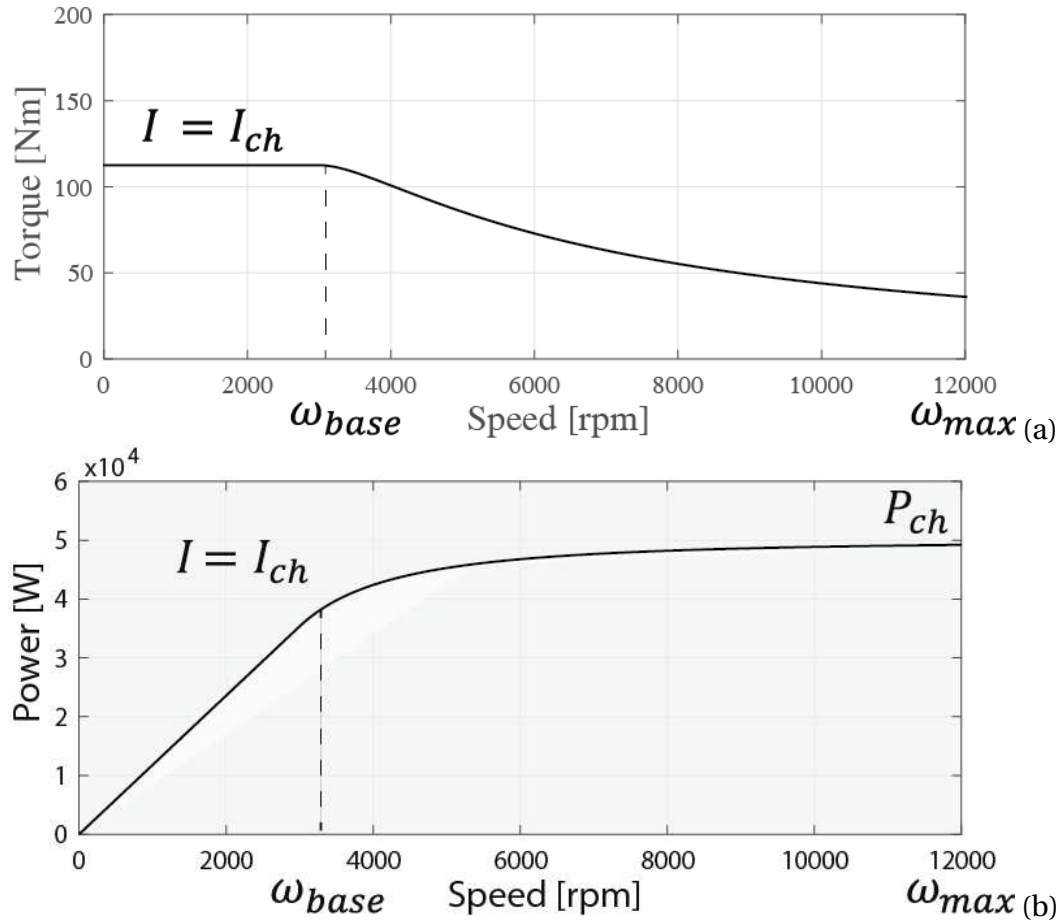


Fig. 3.3 Torque (a) and power (b) versus speed profiles supplied with characteristic current, under constrained voltage

### 3.1.3.1 Design Input

With reference to the machine's ratings reported in Table 3.1, the slot-pole combination is constant in this study and the initial design inputs are:

- Stack dimensions  $D$ ,  $L$  and airgap length  $g$ .
- PM remanence  $B_r$  and peak flux density in steel  $B_{fe}$ .
- Thermal loading  $k_j$ .
- Tooth length  $l_t$  and Tooth width  $w_t$ .
- magnet length  $l_m$  and magnet angular span  $\alpha_m$

The number of turns  $N_s$  is set to an initial value and adjusted in the final stages of the design according to the specified voltage and speed ratings.

The thermal loading  $k_j$  [ $W/m^2$ ] is expressed in the form of copper loss per stack surface:

$$k_j = \frac{\text{copper loss}}{\pi DL} = \frac{(6N_s I)^2}{\frac{k_{cu}}{\rho} \cdot \frac{L}{l_{end}+L} \cdot 2\pi D \cdot A_{slots}} \quad (3.5)$$

Where  $\rho_{Cu}$  is the copper resistivity,  $k_{Cu}$  is the slot fill factor.  $A_{slots}$  is the total slot areas,  $l_{end}$  is the end-turn length, and  $I$  is the amplitude of current.

After defining the size and winding type, the allowed electric loading  $A_s$  [ $A/m$ ] is indirectly obtained by the thermal loading (3.5),

$$A_s = \frac{6N_s I}{2\pi \cdot (r + l_m)} \quad (3.6)$$

The product  $N_s I$  together is proportional to  $\sqrt{k_j}$  according to (3.5), and also contributes to electric loading  $A_s$ .

Thermal loading  $k_j$ , instead of  $A_s$ , is used here because it contains information both on stator and rotor quantities, whereas the electric loading refers to the rotor size only. Moreover,  $k_j$  is more intimately related to the copper temperature.

Table 3.1 Machine data

	Unit	motor in [36]	present motor
Converter phase voltage	V pk		173
Converter current	A pk		360
Stack length	mm		170
Steel grade			M250-35A
PM grade			BMN-42SH
Copper temperature	°C		150
Rotor temperature	°C		130
Pole pairs			2
Rated current	A		≥192A
Torque at base speed	Nm		120
Base speed $\omega_{base}$	rpm		about 4000
Power target at max. speed	W		50000 (point F)
Max. speed $\omega_{max}$	rpm		12000
Stator outer diameter	mm		216
Number of slots			6
Stator bore diameter	mm	124	128
Airgap	mm	0.7	1
Copper fill factor		0.4	0.55
Number of turns		23	24
Torque at 360 A	Nm	150	164
Characteristic current	A pk	193	198
Phase resistance at 130 °C	Ω	0.026	0.02
Magnet mass	kg	1.35	2.17

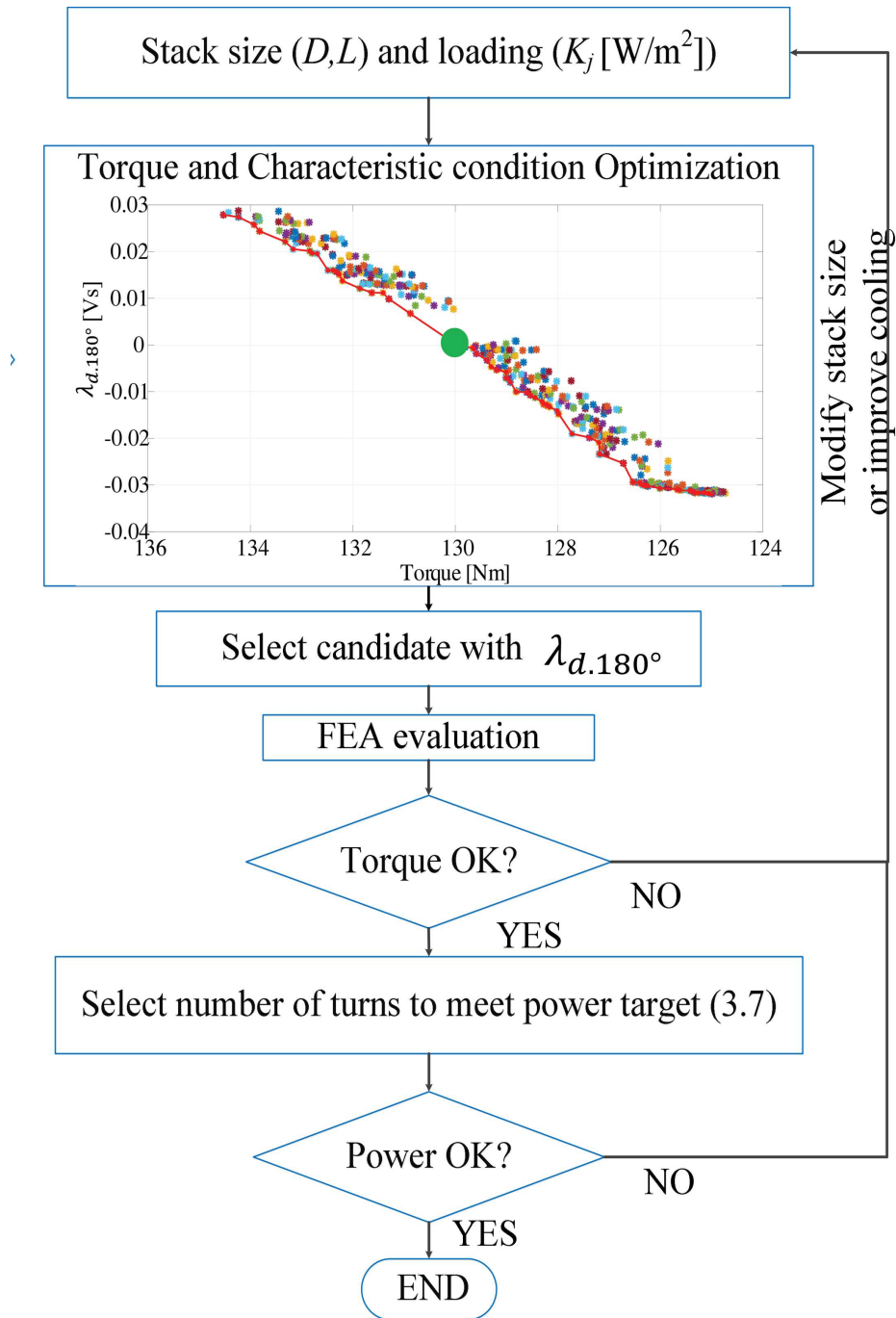


Fig. 3.4 Automatic design flowchart for the CW-SPM machines



### 3.1.3.2 Design Flowchart

The design flowchart is reported in Fig. 3.4. The MODE optimization algorithm produces a Pareto front in two dimensions. One solution machine is selected from the Pareto front (green marker), as explained in the following.

The first design goal is torque, evaluated with a current phase angle  $\gamma = 90^\circ$ , corresponding to MTPA production, as reported in Fig. 3.5. The second design goal is the metric of the flux weakening capability of the machine and it is called  $\lambda_{d,180^\circ}$ . The goal function  $\lambda_{d,180^\circ}$  accounts for the  $d$ -axis flux linkage when the current vector is aligned against the PMs ( $\gamma = 180^\circ$ , Fig. 3.5 b). If this is positive, then the characteristic current of the candidate design is larger than the simulated current. The opposite is true for negative values of  $\lambda_{d,180^\circ}$ . If this is zero, then the candidate design is exactly in characteristic current conditions. Fig. 3.5 describes how the two goals are FEA evaluated during the optimization process. Torque evaluation (Fig. 3.5a) requires the simulation of at least 5 rotor positions over one stator slot pitch to account for torque ripple effect. The first position is randomly selected within one fifth of the stator slot pitch, and then other four positions are distributed evenly [83]. One additional simulation is used to evaluate the residual flux linkage  $\lambda_{d,180^\circ}$  (Fig. 3.5b). All included, this makes 6 static FEA simulations per candidate. The anticipated Pareto front required the evaluation of 10,000 individuals, for a total 60,000 FEA simulations. This took 26.5 hours on a standard desktop computer (Intel Core i7-2600 CPU @3.40 GHz), using four cores in parallel.

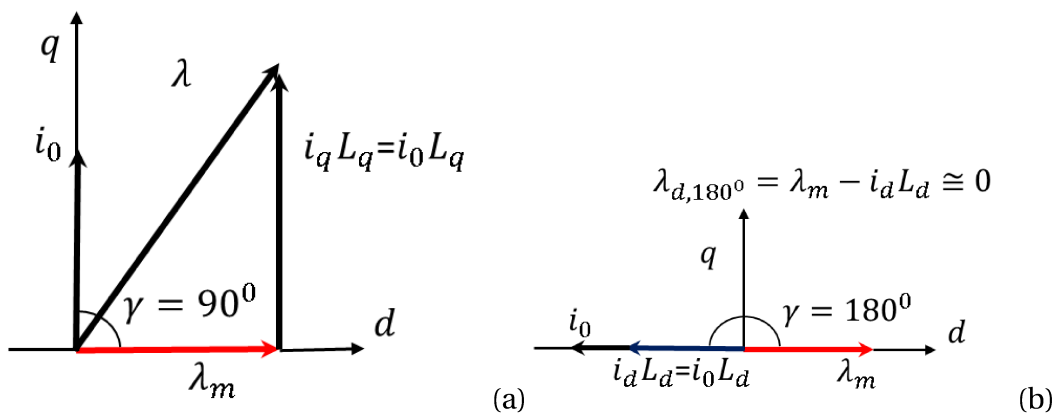


Fig. 3.5 (a) Torque evaluation, current is placed  $\gamma = 90^\circ$ . (b) Flux weakening capability evaluation: current is placed at  $\gamma = 180^\circ$

Large quantities of individuals evaluations are used to ensure adequate candidate models can be obtained to form the Pareto front of Fig. 3.6. On the Pareto front, one gets nearly zero  $\lambda_{d,180^\circ}$  is chosen as the final solution (green marker).

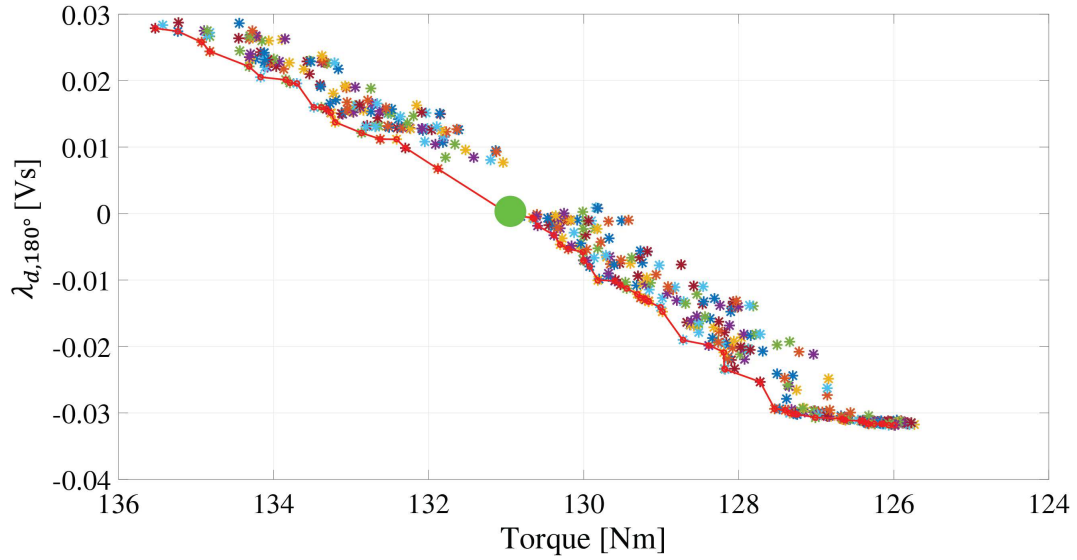


Fig. 3.6 Pareto front of CW-SPM design optimization

The FEA calculated power envelope of design candidate is presented in Fig. 3.7.

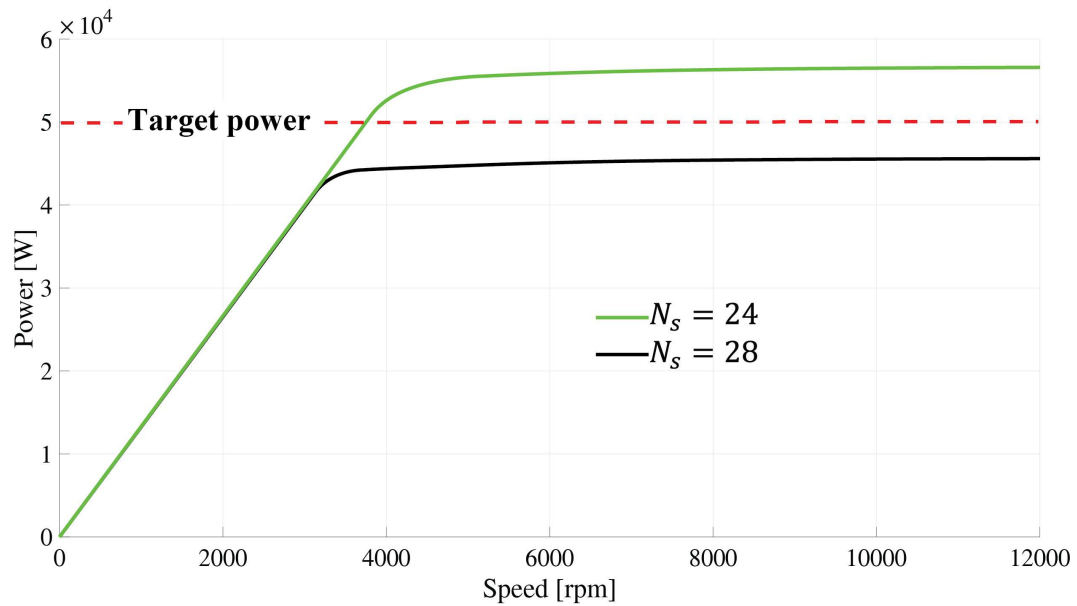


Fig. 3.7 Power profile of CW-SPM machines

The figure shows that changing the number of turns modifies the height of the power plateau and not the nominal torque. From (3.7),  $k_j$  is proportional the combination of  $N_s I$ . As given the key input  $k_j$ ,  $N_s$  is inversely proportional to machine current, which is directly relates to maximum power. In turn,

$$\frac{N'_s}{N_s} = \frac{P_{ch}}{P'_{ch}} \quad (3.7)$$

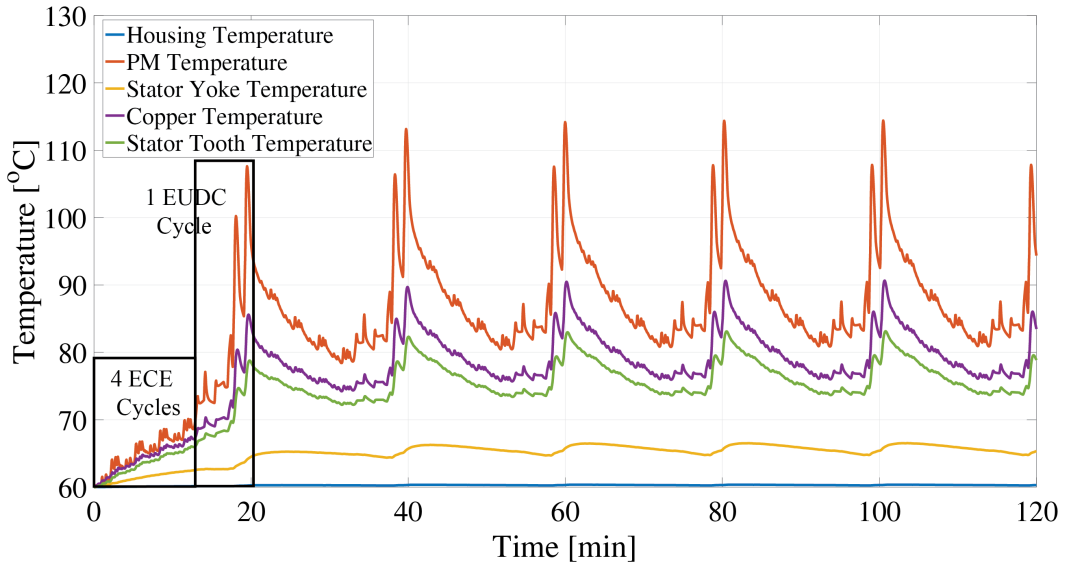


Fig. 3.8 Temperature result for CW-SPM under repeated NEDC conditions

### 3.1.3.3 Non Magnetic Aspects

A simplified thermal model integrated into SyR-e estimates the copper temperature given the loading condition  $k_j$  [ $W/m^2$ ]. This model is based on radial heat transfer between stator copper and housing. Axial effect is neglected (2D model). Housing temperature is set. The steady-state copper temperature is estimated after the loading factor  $k_j$ , the total stator slot area, slot filling factor and housing temperature [111]. The user can immediately check if the considered  $k_j$  is compatible with the target copper temperature. In this research, the target copper temperature was 130 °C. Finally, copper and magnet temperatures are verified using a lumped parameter transient thermal model available in *Infolytica/Motorsolve* [112], with reference to the selected driving cycle. Made up of 4 ECE and 1 EUDC

cycles, the NEDC driving cycle has been repeated six times in two hours through the test, with the coolant temperature at 60 °C and flow rate at 10 *liter/min*. The temperature result for CW-SPM is reported in Fig. 3.8.

### 3.1.4 Results

The final structures of both machines are shown in Fig.3.9. Compared with previous machines [36], the magnets (grey parts) are both radially and axially segmented into 5 parts, respectively. PMs are thicker than the one in [36] to prevent irreversible demagnetization. Conversely, the cost of magnet is higher.

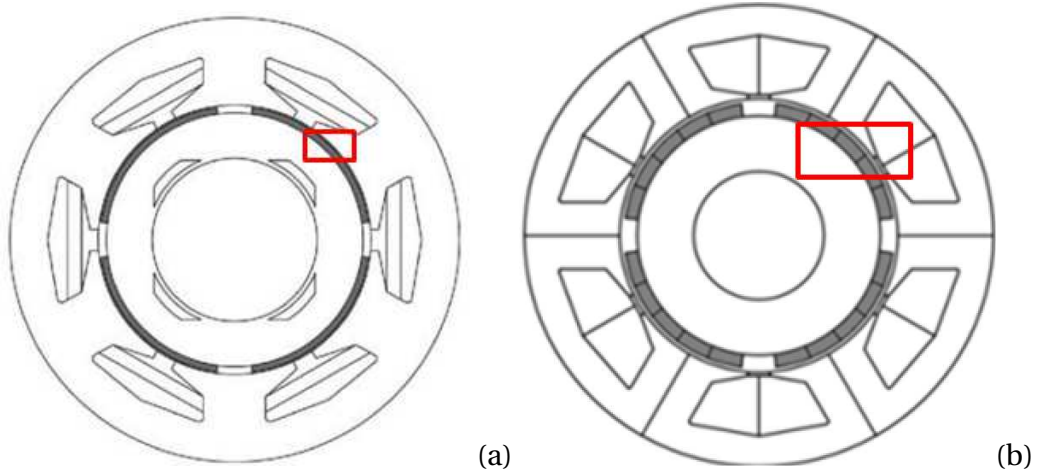


Fig. 3.9 Motor structures: (a) benchmark CW-SPM; (b) present CW-SPM

As mentioned before, the final metric of this study are torque and power curves, as well as efficiency maps. Firstly, flux linkage maps ( $\lambda_d \cdot \lambda_q$ ) of two machines are evaluated off-line via SyR-e over a current domain as large as  $360\text{A} \times 360\text{A}$  in  $i_d, i_q$ . Afterwards, torque maps are calculated by (2.12).

Based on these maps, the MTPA control law is obtained, valid at low speed. When voltage limit is met, the current vector is further rotated for flux weakening Fig.(3.2). Another script available in SyR-e builds the flux weakening control law, including the MTPV trajectory and minimization of total loss for each torque and speed combination.

### 3.1.4.1 Torque and Power Curves

Fig. 3.10 shows the torque curve of the machine. The CW-SPM machine have a torque at maximum current condition that is markedly higher than the corresponding one in [36], which demonstrates an increase of the transient capability of the powertrain. This is true also at maximum speed, where present machines get higher torque (50  $Nm$ ) than those of benchmark machines (39  $Nm$ ). Dealing with the power curves of Fig. 3.11, the present CW-SPM machine shows similar power curves in characteristic current conditions, having very similar values of  $I_{ch}$ .

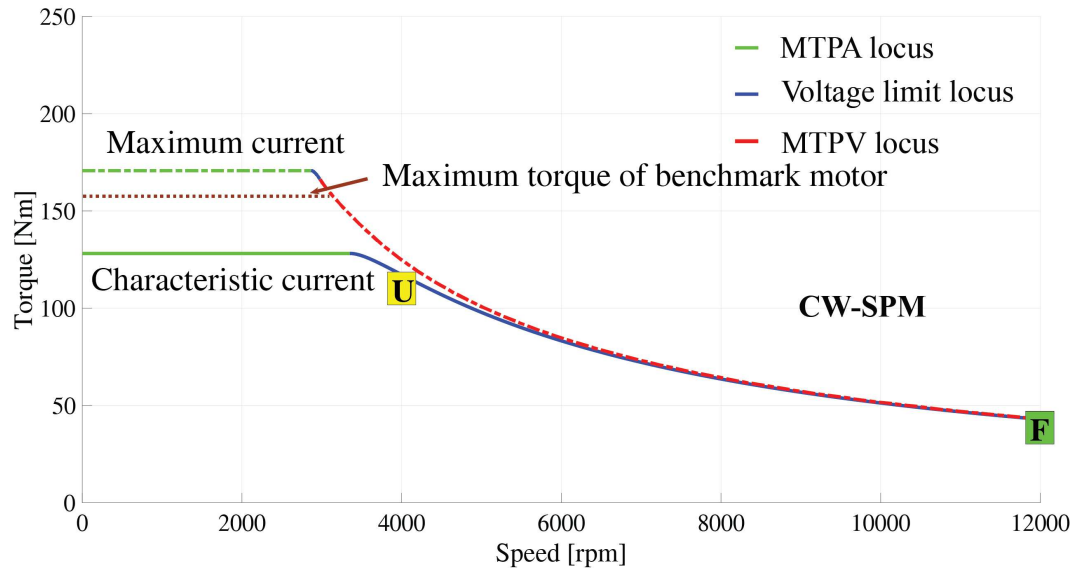


Fig. 3.10 Torque curve at their characteristic current and at maximum inverter current, considering the maximum voltage limit

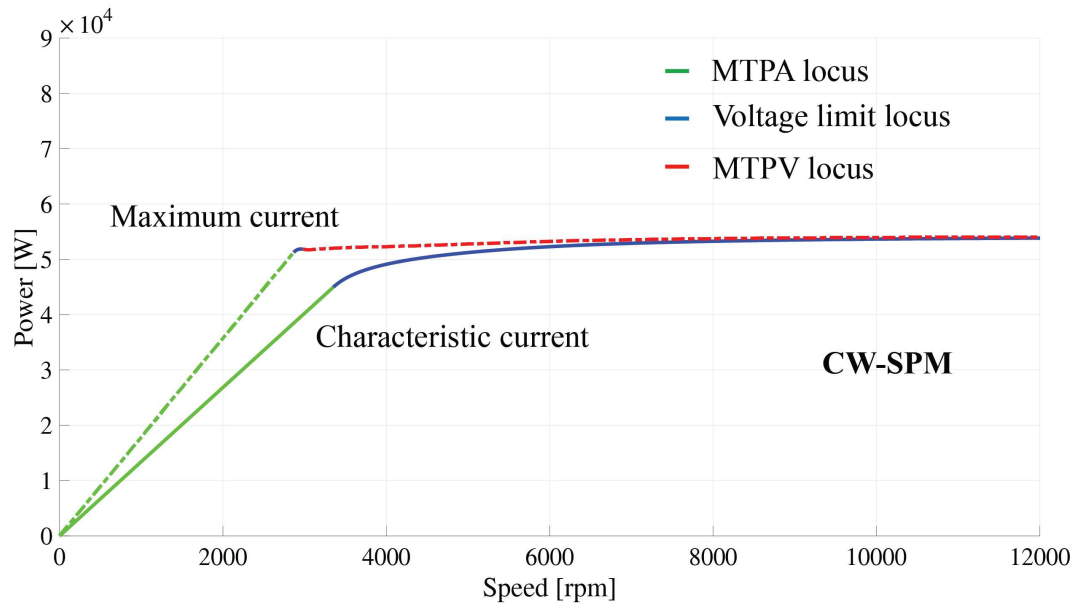


Fig. 3.11 Power curve at their characteristic current and at maximum inverter current, considering the maximum voltage limit

### 3.1.4.2 Loss and Efficiency Maps

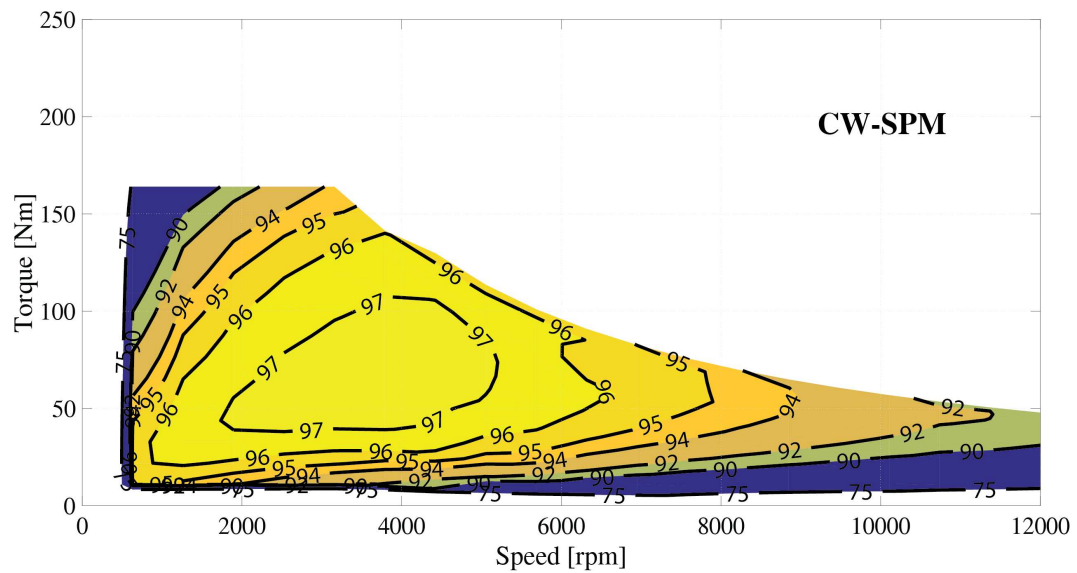


Fig. 3.12 Efficiency map

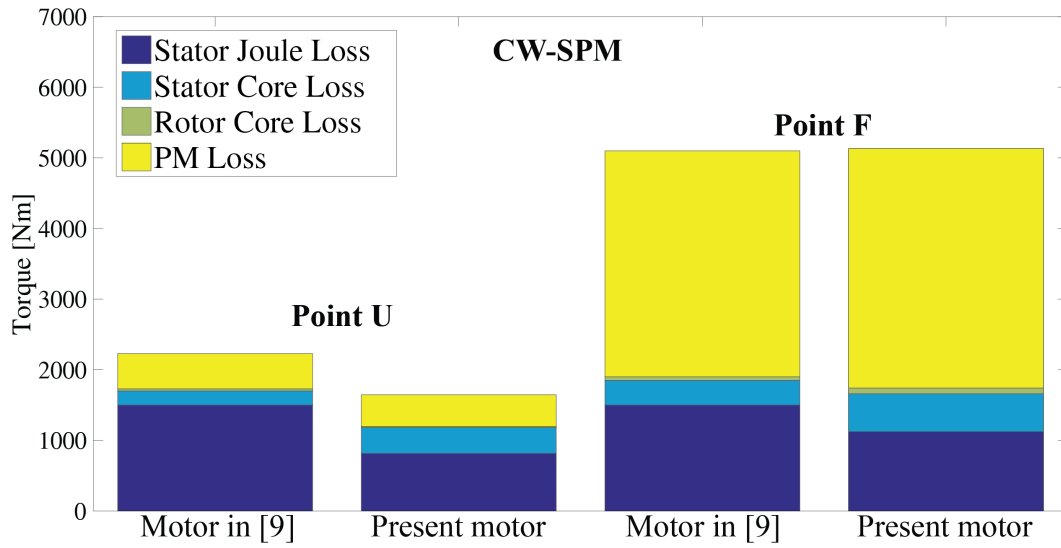


Fig. 3.13 Power loss at specific points of the new machine, and comparison with the benchmark machine

Power losses are FEA evaluated through *MagNet/Infolytica*, including core, PM, and copper losses. Simulations are repeated over the machine current domain at a single speed value. Then, frequency is adapted to the different speed conditions using the modified Steinmetz approach described in [113], using the coefficients of the magnetic steel in use. Fig. 3.12 shows the efficiency map of the designed machine.

Burdened by high PM loss, the high-speed efficiency of the CW-SPM machine is that much high. Loss details are reported in Fig. 3.13, for operating points U and F. Compared to the efficiency map reported in [36], efficiency distributions are similar to the ones of the respective benchmark machine. Both present designs show an increase of peak efficiency (97% versus 96%). This is related to the better torque per copper loss factor of both new design, as put in evidence by the loss split of Fig. 3.13.

The magnets of the CW-SPM machine are segmented both axial and radial wise (5 segments per direction) for diminishing eddy current loss. Nevertheless, the machine is still burdened by high magnet loss at high speed (point F). In addition, copper loss grows from point U to point F, due to the significant power loss de-excitation current component. Compared to the benchmark CW-SPM machine, although copper loss is lower for the same operating point, total loss at point F is the same, due to augmented magnet loss. Higher magnet loss come

from the larger magnet volume of the new design (+59%, see Table 3.1), mainly related to the augmented airgap (1.0 *mm* instead of 0.7 *mm*).

### 3.1.5 Design Summary

The study presents an automatic design approach for the design of CW-SPM machines for traction. The design tool used in the study consists of Matlab scripts available online and includes design equations, magnetic FEA, multi objective optimization, simplified structural and thermal co-design. The CW-SPM machine example accounts for automatic design capability of SyR-e, based on MODE optimization. Besides providing comprehensive design procedures for CW-SPM machines for traction, the study suggests new design methodologies, such as the goal function  $\lambda_{(d,180^\circ)}$  that summarizes flux weakening capability in one FEA simulation. Torque and power profiles of designed machine are reported. The losses and efficiency map are also illustrated.

## 3.2 Automatic Design of a DW-SPM Machine

Part of the work described in this chapter has been previously published in [114].

### 3.2.1 Design Background

The cogging torque of SPM machines, which results from interaction between PM edge and stator slot openings causing vibration and noise, is a significant issue for high performance requirements [9]. Many methods have been developed for reducing cogging torque [115], for example, rotor skewing, magnet shifting or shaping, applying notches in stator teeth, etc. Each method has its own merits and drawbacks. In terms of skewing, although it effectively diminishes cogging torque, it also reduces the torque output of the machine and increases the manufacturing cost [116]. Similarly, magnet shaping can decrease the interaction between magnet and stator teeth, at the risk of reducing the fundamental airgap flux density, and therefore average output torque.



This research deals with analytical calculation of SPM machines cogging torque, when magnet shaping is applied. Based on that, this study investigates the trade-off between average torque and cogging torque performance using a constrained stator geometry and MODE optimization. Demagnetization of PMs and volume (i.e. cost) of PMs are also considered in the study. In turn, the study formulates an automatic design process for SPM machines with magnet shaping, validated by FEA.

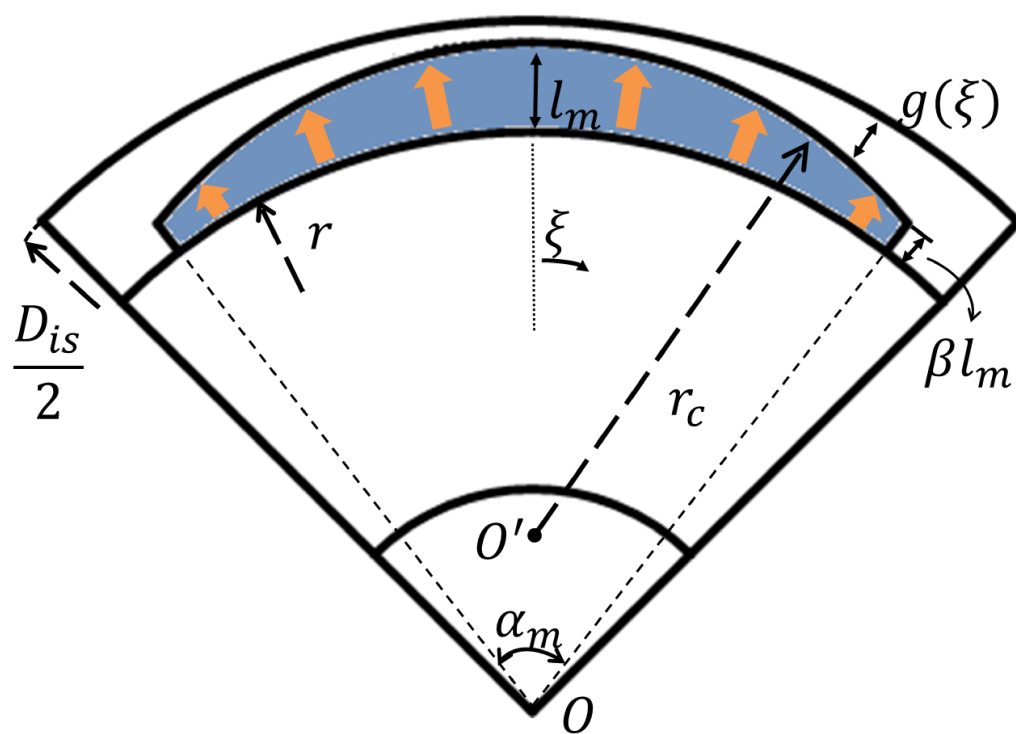


Fig. 3.14 Definition of PM parameters

### 3.2.2 Design Flowchart

#### 3.2.2.1 Rotor Geometry

In order to define the shaping degree of the PMs, one more factor  $\beta$  is added. It is defined as the length at PM ends, in p.u of the magnet length  $l_m$ . The relevant rotor geometry is shown in Fig.3.14. The detailed geometry analysis will be discussed in next chapter.

#### 3.2.2.2 Design Input

The main machine ratings of the selected design example are reported in Table 3.2. MODE and FEA methods are utilized to optimize PM shape giving optimal magnet flux linkage  $\lambda_m$  and cogging torque  $T_{cog}$  at open load condition. By applying (2.13), the torque output is obtained from the product of  $\lambda_m$  and maximum current  $i_q$ . The cross-saturation effect is neglected. Therefore, by evaluating  $\lambda_m$  and  $T_{cog}$  at open load condition, the torque performance at rated condition can be estimated.

The optimization inputs are:  $l_m$ ,  $\alpha_m$  and  $\beta$ . The stator geometry is not changed in this study. Other cost functions considered off-line after the optimization are the distance from the demagnetization limit and the mass of the PMs. The procedure of optimization process is shown in Fig. 3.15.

To prevent fracture in manufacturing process, the PM ends should not be too thin. Besides the manufacturing issues, the PMs must be protected against demagnetization by having adequate minimum length  $\beta \cdot l_m$ . The maximum armature magnetoforce (mmf) per pole is defined as [60]. Since the current is fixed on  $q$  axis, then (2.17) can be modified as,

$$F_{p1} = \frac{3}{2} \frac{4}{\pi} \frac{k_w N_s}{2p} i_q \quad (3.8)$$

Assuming that the iron has infinite permeability and all the mmf drop happens at the airgap, the maximum airgap flux density produced by current alone at the magnet's edges is,

$$B_{g_{iq}} = \frac{F_{p1} \mu_0}{g} \frac{4}{\pi} \frac{\mu_0 k_w N_s i_q}{2p [l_m (\xi = \frac{\alpha_m}{2}) + \mu_r k_c g (\xi = \frac{\alpha_m}{2})]} \quad (3.9)$$

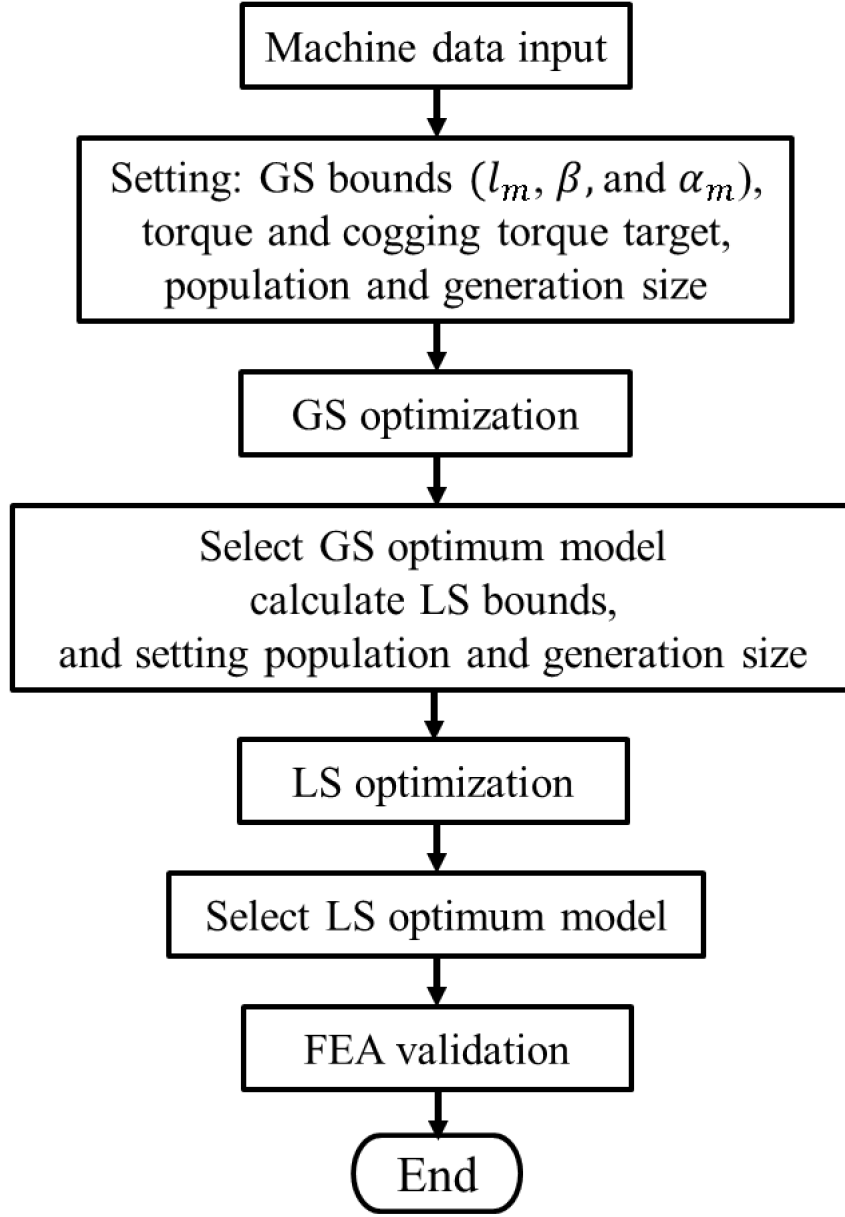


Fig. 3.15 Flowchart of optimization procedure for  $T_{cog}$  and torque

To protect the PMs, they must be designed so that the flux density (4.31) is equal or larger than the minimum allowed flux density of the PMs  $B_d$ , corresponding to the knee point of the magnet demagnetization curve. Hence,

$$B_m(\xi = \frac{\alpha_m}{2}) \geq B_{g_{iq}} + B_d \quad (3.10)$$

The  $B$ - $H$  curve and the relationship (4.32) are graphically associated in Fig. 4.19. In this study,  $B_d$  is 0.1 T and the maximum allowed current  $I_{max}$  is 26 A. Moreover, Fig. 3.16 represents the relationship among maximum allowed current and  $\beta$ , with  $l_m$  as a parameter. The figure illustrates that the maximum current is proportional to the shaping factor  $\beta$  when  $l_m$  is fixed. For this design, acceptable values of  $\beta$  are above 0.33.

For magnets having constant length the magnet span  $\alpha_m$  giving minimum cogging torque is as [118],

$$\frac{\alpha_m}{\tau_p} = \frac{N - m_1}{N} + m_2 \quad (3.11)$$

Table 3.2 Main parameters of target machine

Parameters	Unit	Values
Number of slots		36
Pole pairs		3
Stator inner diameter	120	mm
Stator outer diameter	175	mm
Stack length	110	mm
Minimum airgap length	1	mm
Slot opening ratio	0.3	
Maximum current	26	A
Maximum speed	1000	rpm
Number of turns per phase		120
Torque target	Nm	56
Peak cogging torque limit	Nm	1

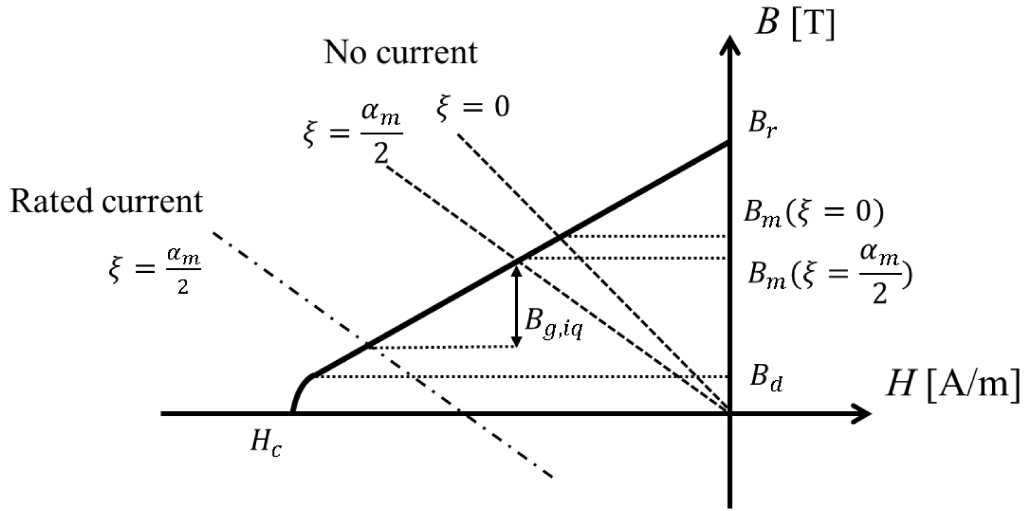


Fig. 3.16 Operating point determination with demagnetization limit (NdFeB 32 MGOe at 80 °C)

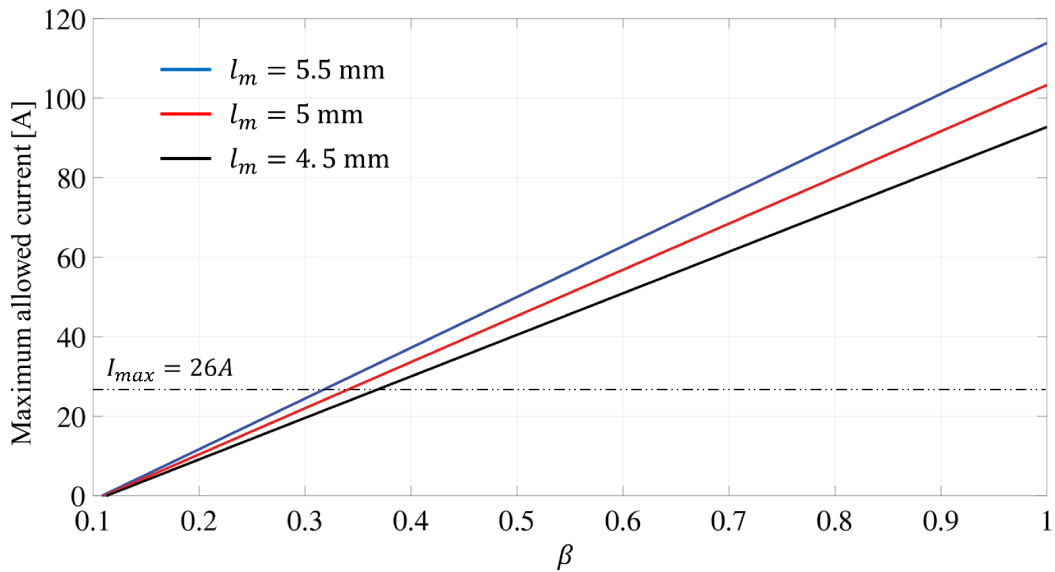


Fig. 3.17 Relationship among  $\beta$ ,  $l_m$  and maximum allowed current

Where  $N = k/2p$  ( $N = 6$  in the reported example),  $m_1$  is an integer from 1 to  $(N - 1)$ ,  $\tau_p$  is the pole pitch. Due to the fringing PM flux entering into the slot side, additional factor  $m_2$  should be taken into account, which ranges from 0.01 to 0.03 [119]. The formula is valid for magnets having uniform thickness. In this study, the airgap thickness is gradually increasing from pole center to PM edge, making the

mutual effect between PM edge and slots less acute than that in uniform thickness PM case. Based on that, in order to achieve more possible solutions,  $m_2$  has been increased to 0.05. Since larger  $\alpha_m$  generate higher torque, it is convenient to set  $m_1 = 1$ . In this study, the range of PM span is set as  $0.83\tau_p$  to  $0.88\tau_p$ . After defining the bounds of PM shape, the MODE procedure will automatically optimize the torque and cogging torque performance.

### 3.2.3 Results

As mentioned beforehand, the stator geometry in this study is fixed. According to [117], MODE is more efficient to get desired results in terms of the number of machine candidates. The bounds setting of magnet parameters are shown in Table 3.3.

Table 3.3 Limit of search space for optimization

Main parameter	$l_m$	$\beta$	$\alpha_m$
Bounds (GS)	[5, 7]	[0.24, 1 ]	[150, 159]
GS-optimum (Motor 0)	6.89	0.55	155.7
Bounds (LS)	[6.54, 7]	[0.52, 0.57]	[150, 159]
LS-optimum (Motor 2)	6.95	0.57	158
Units	mm	p.u.	elt. degree

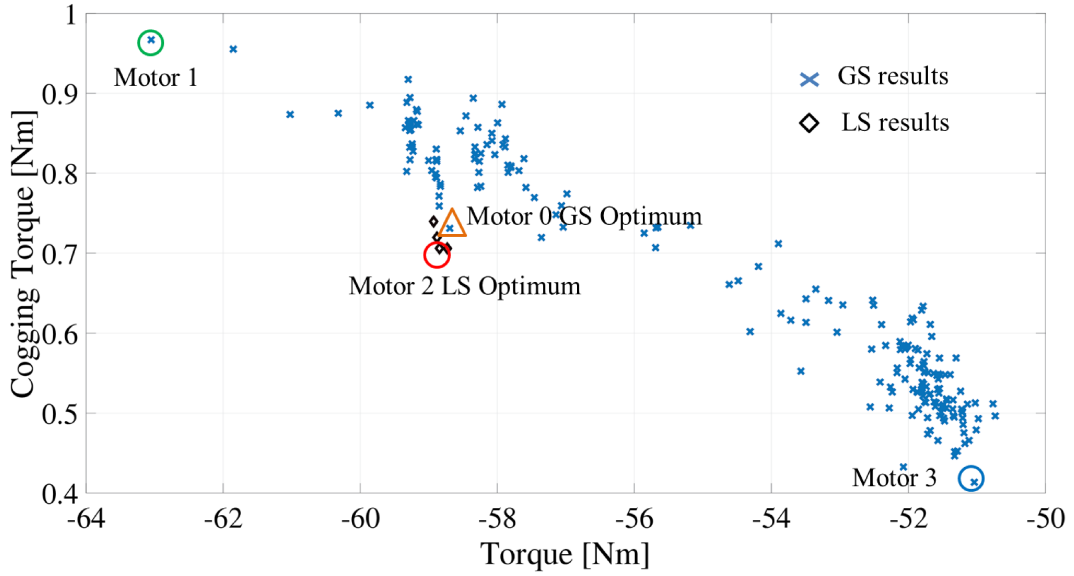


Fig. 3.18 Pareto front of both GS and LS stages

A two-stage optimization procedure is used here to save the running time which consists of first step called global search (GS) and a refined step called local search (LS). This approach was first suggested in [87]. During the GS process, 10000 candidates are involved (100 individuals in one population over 100 generations). Each candidate is evaluated by 31 FEA simulations for 31 rotor positions distributed evenly over one slot pitch. Then cogging torque is defined as the difference between maximum and minimum torque values.  $\lambda_m$  is the mean flux linkage value along with d axis of total 31 simulations. Then the maximum torque capability is calculated by (2.13) and reported as a negative value. After 16-hour parallel computing processing in a standard desktop computer (Intel i7, 4-core, 16 GB RAM), the Pareto front is obtained. One promising solution is selected as the base design for the subsequent LS stage. The search bounds of the LS optimization are  $\pm 5\%$  of base model data input. Then another 200 refined candidates are evaluated in 30 minutes. The final Pareto front consists of both GS and LS stage is reported in Fig. 3.18.

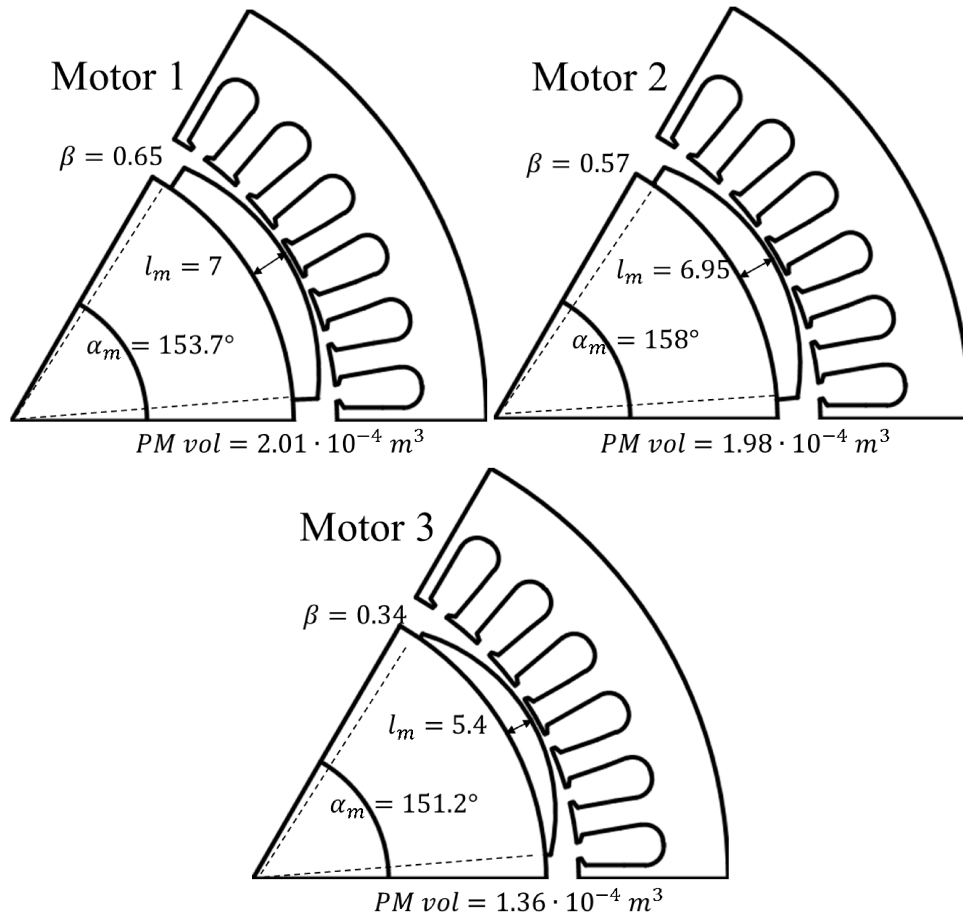


Fig. 3.19 Three different machines cross-sections from Pareto front

The optimization result consists of 208 machines from the evolution process. From Fig. 3.18, it is reported that the lowest cogging torque is around 0.4 Nm in this research. However the machine with lowest cogging torque is not able to generate adequate maximum torque (blue circle, Motor 3). Conversely, the one can produce highest torque has a worst cogging torque situation (green circle, Motor 1). The machine located at left bottom of Pareto front (red circle, Motor 2) is the one with best trade-off between cogging torque and torque producing capability. The cross-sections of three machines are shown in Fig. 3.19 with their relative magnet parameters.



Table 3.4 Analytical and FEA results comparison on magnet edge

		$B_m(\xi = \frac{\alpha_m}{2})$ [T]	$B_{g,s}$ [T]	$B_{min}$ [T]
Motor 1	Analytical	0.63	0.23	0.4
	FEA	0.65	-	0.49
Motor 2	Analytical	0.55	0.2	0.35
	FEA	0.61	-	0.46
Motor 3	Analytical	0.33	0.14	0.19
	FEA	0.39	-	0.31

The detailed cogging torque waveforms of three machines over two slot pitches are presented in Fig. 3.20. The zero rotor position is defined as the line where the PM center aligned with the tooth center as the same position shown in Fig. 3.19. Although the cogging torque performance of Motor 3 is the best solution among the Pareto front, the torque production is considerably lower than others. The red model is chosen as the optimal solution to be a prototype since it can achieve the maximum torque target (56 Nm) with relatively low cogging torque. The torque waveforms for the three machines over an entire period under maximum current condition are presented in Fig. 3.21. The average torque outputs from FEA are matched with the analytical results obtained from (1). Moreover, it also illustrates that the torque ripples of the three machines have the same trend of their cogging torque results. The torque ripple has been reduced while the edge length of magnet becomes shorter (from Motor 1 to Motor 3). Considering the cost, a larger amount of magnets is used in Motor 1. Compared with Motor 1, Motor 2 is also the cost-optimal one, shown in Fig. 3.19.

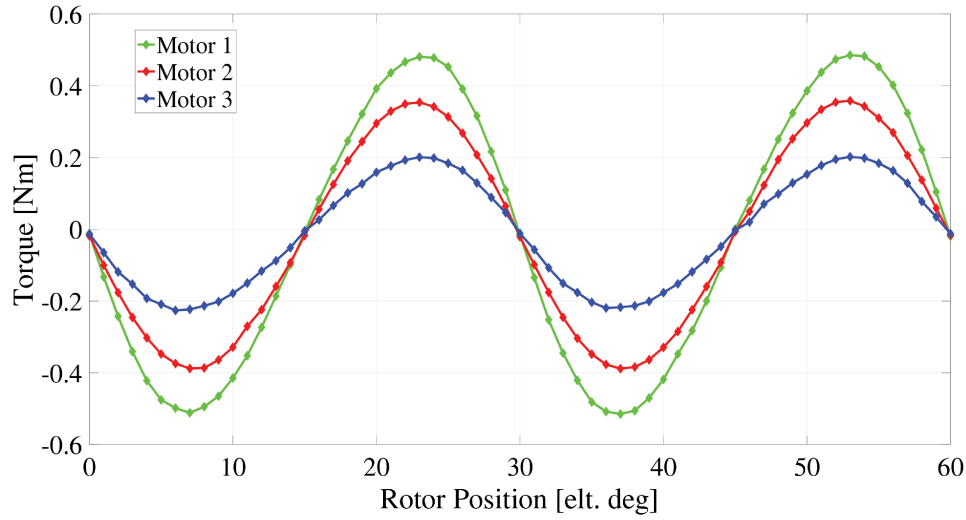


Fig. 3.20 Cogging torque waveforms of three motors

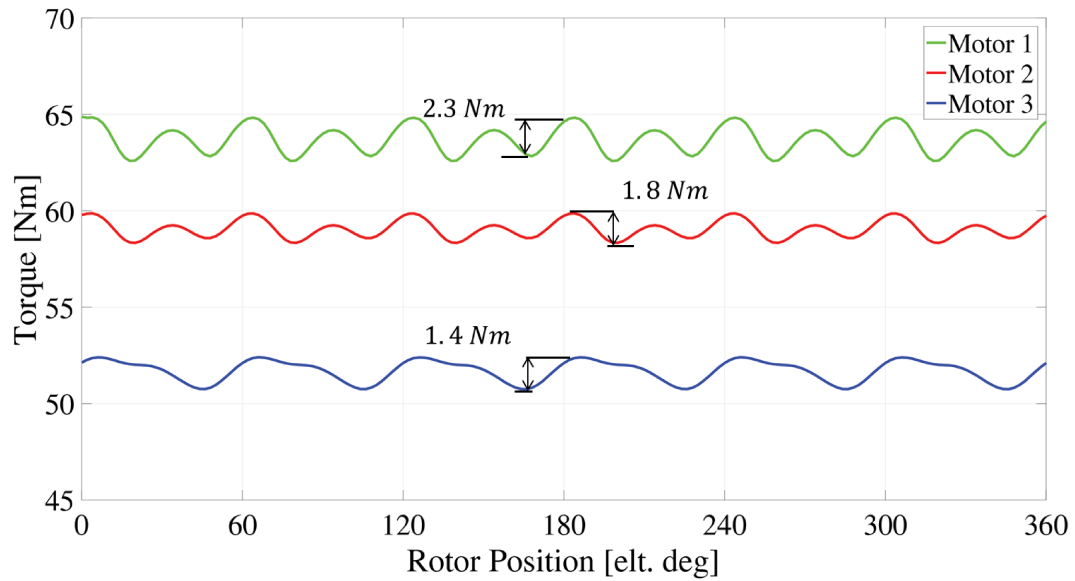


Fig. 3.21 Torque waveforms of the three motors

Considering the demagnetization limit, the minimum flux density on PM edge from analytical and FEA results of the three machines are reported in Table 3.4. The FEA results on  $B_{min}$  are higher than those from analytical calculation since the current is not applied along  $q$  axis. The FEA results present that the PMs are prevented from demagnetizing risk.

### 3.2.4 Design Summary

This study presented a design procedure to optimize the PM shape of rounded SPM machines to find an optima trade-off between torque and cogging torque behaviors. Both torque and cogging torque calculation through magnet shaping method is analyzed. Dependent on demagnetization limit and optimal magnet span calculation, the magnet bounds in optimization process are obtained. The cogging torque and maximum torque waveforms of three different machines on Pareto front are shown, which is obtained by MODE optimization and FEA simulations. One optimum machine is selected as the best trade-off machine among PM volume, torque and cogging torque behaviors.

## Chapter 4

# Parametric Design Procedure for SPM Machines

Besides automatic design procedure, SyR-e also includes another effective machine design method, which is called parametric design procedure. The whole development process of parametric design procedure for SPM motors is addressed in this chapter. This machine design method for SPM motors has been developed in three following steps.

The parametric design procedure is based on a parametric design plane, which at the beginning, it is established based on  $(x, b)$ . The two parameters  $x$  and  $b$  represent the rotor split ratio and magnetic loading factor, respectively. A CW-SPM motor is designed via this process for traction application. The whole flowchart is presented in Section 4.1.

Later in order to simplify and make the parametric plane more useful and insightful,  $(x, b)$  plane is modified into  $(x, l_m/g)$  plane. The later parameter  $l_m/g$  is the magnet-airgap length ratio, addressing the airgap flux density magnitude directly. Moreover, SPM motors with profiled PM shape can be also created by the parametric design method. The related design process is describes in Section 4.2.

At the first and second steps, the sizing equations on teeth width and length are referring to the average airgap flux density along one pole pitch produced by PMs. Then, more accurate sizing equations are embedded into the design process by applying subdomain analytical model. The current sizing equations are only

considering the flux density passing into the most loaded tooth in one slot pitch. The detailed analysis is given in Section 4.3.

## 4.1 Parametric Design Procedure Based on $(x, b)$ Plane

Part of the work described in this chapter has been previously published in [120].

### 4.1.1 Design Background

This study aims at simplifying the design approach by using the nominal power factor (PF) of the machine as the metrics for achieving an optimal trade-off between starting torque and flux weakening capability.

A parametric design approach is introduced, inspired to the general design approach used in [81] for machines with high numbers of poles. Torque and PF at rated current loading are evaluated in the  $(x, b)$  parametric plane, where  $x$  is the rotor / stator split and  $b$  is per unit magnetic loading. The  $(x, b)$  plane thus represents a continuum of machines with different rotor and stator geometries, all within the same stack envelope. A parametric plane established based on rotor split ratio  $x$  and per unit magnetic loading  $b$  is obtained since  $(x, b)$  can quickly get access to the trade-off between torque and PF.

Among all solutions, the one with PF equal to  $1/\sqrt{2}$  and maximum torque is selected, being the one with the highest torque among the ones with infinite flux weakening capability, as shown in the study. The characteristic current condition is the pivot of this analysis: all advisable designs will have the nominal current equal to their characteristic current [50].

### 4.1.2 Design Procedure

This study uses two key design specifications for the design of the electric motor for traction: 1) nominal torque, under the base speed, and 2) nominal power at maximum speed. The key design parameter is the characteristic current of the PMSM, as all investigated designs will respect the condition of having the nominal current equal to the characteristic current:

$$I_{ch} = \frac{\lambda_m}{L_d} = I_n \quad (4.1)$$

Such design condition turns into an asymptotically flat power versus speed profile in voltage and current limited conditions, shown in Fig. 4.1 (a).

$$P_{nmax} = P_{ch} = \frac{3}{2} V_{max} \cdot I_{ch} \quad (4.2)$$

The base speed is where flux weakening starts, i.e. when the inverter voltage limit kicks in. Base speed is not an explicit design input in this analysis, as it comes as a consequence of the two key design goals of torque and power, as said. At base speed, output power is:

$$P_{base} = T_n \cdot \omega_{base} = \frac{P_{ch}}{\sqrt{2}} \quad (4.3)$$

The proposed design flowchart targets power curves of the kinds depicted in Fig. 4.1: the continuous curve refers to strict respect of (4.1), whereas the sharper power curve in dashes is obtained imposing  $I_n > I_{ch}$  by design (in the example  $I_{ch}$  is same as before and  $I_n$  is 170% of  $I_{ch}$ ). In this second case the starting torque is higher, the power profile sharper, and this can be useful, if required by the application.

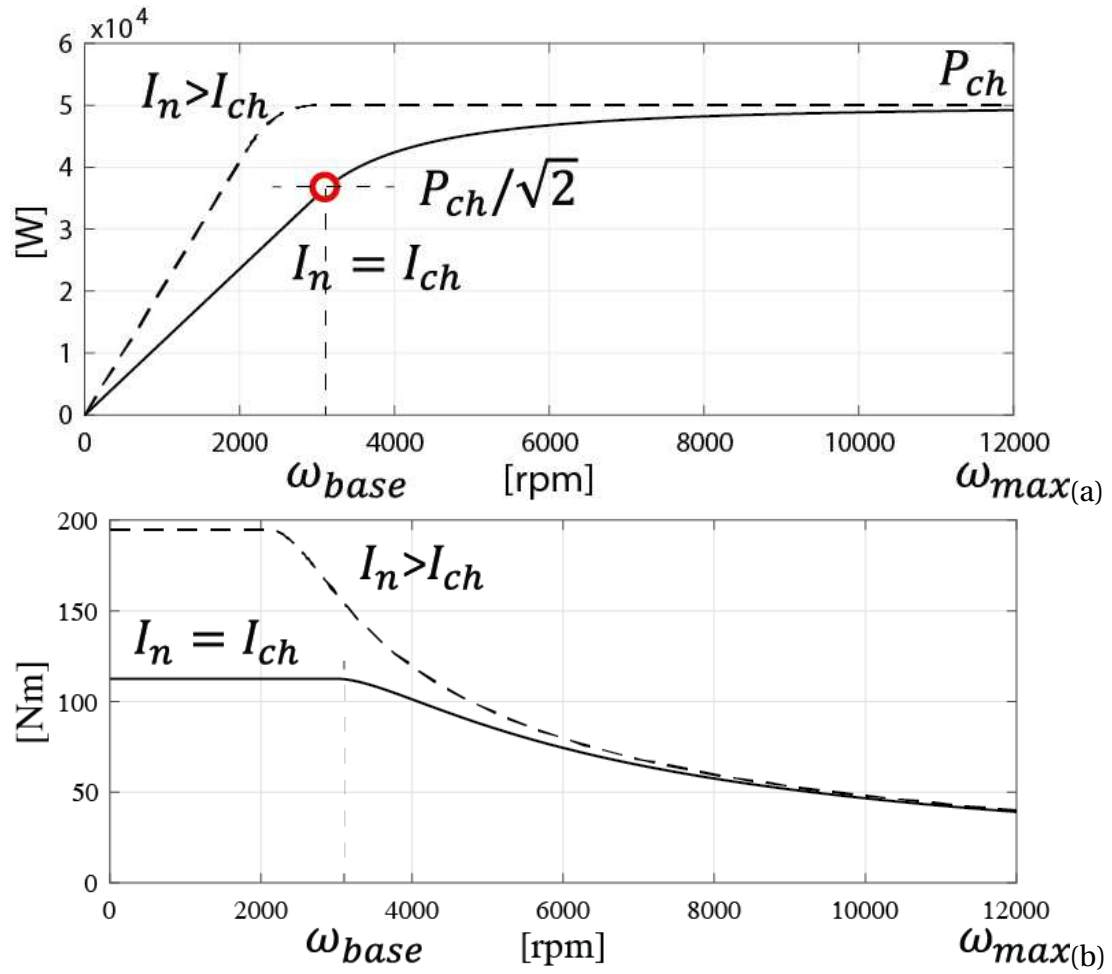


Fig. 4.1 Torque and power versus profiles under characteristic current and limited inverter voltage conditions. Two designs are reported: one with rated current equal to  $I_{ch}$  (continuous line) and rated current greater than  $I_{ch}$  (dashed line)

#### 4.1.2.1 Nominal PF as the Metrics of the Flux Weakening Range

When the SPM machine is fed with its characteristic current, the vector diagram is the one in Fig. 4.2. Neglected the stator resistance voltage, when the current vector aligned to the  $q$  axis, the (nominal) power factor is equal to  $1/\sqrt{2}$  [50].

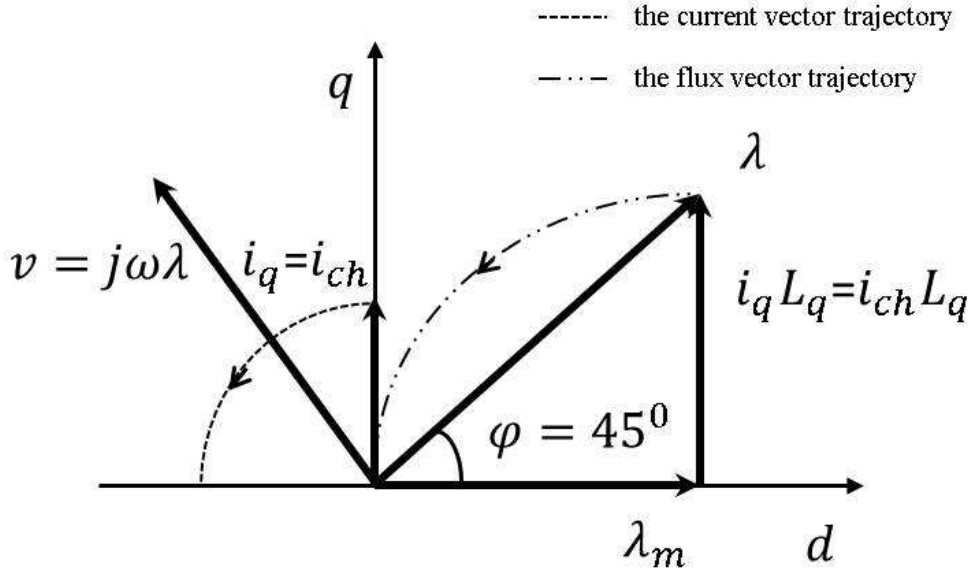


Fig. 4.2 Vector diagram of the CW-SPM machine with  $I_{ch}$  applied on the  $q$  axis

The flux weakening trajectories of the vectors are shown, with the current vector rotated counter-clockwise and the flux linkage trajectory eventually collapsing into the origin, producing the ideal power versus speed curve described above (Fig. 4.1). Therefore, the design condition  $(PF)_n = 1/\sqrt{2}$  gives important insights on the flux weakening capability of one motor design. The design of a CW-SPM machine having a  $PF = 1/\sqrt{2}$  at rated torque, condensates the twofold design specs (torque at low speed and power at high speed) into a single operating point, easy to define (current on the  $q$  axis). Roughly speaking, the torque target will define the machine size, given the cooling capacity, then the  $PF = 1/\sqrt{2}$  condition will guide the trade-off between PM flux linkage and armature inductance optimizing the flux weakening properties of the machine. In turn:

$$(PF)_n = \frac{1}{\sqrt{2}} \rightarrow I_{ch} = I_n \quad (4.4)$$

$$(PF)_n < \frac{1}{\sqrt{2}} \rightarrow I_{ch} < I_n \quad (4.5)$$

Designing the machine after condition (4.4) produces torque and power profiles like the ones in Fig. 4.1 (continuous). Designing after (4.5) produces the profiles represented with dashed lines.



#### 4.1.2.2 Design Input

The two design goals are torque at standstill and power at maximum speed, in nominal current conditions. With reference to the machine's ratings reported in Table 4.1, the parameters defined offline, prior to the design are:

- Stack dimensions  $D$ ,  $L$  and airgap length  $g$ .
- Pole pairs  $p$ , and winding type  $q$ .
- PM remanence  $B_r$  and peak flux density in steel  $B_{fe}$ .
- Thermal loading  $k_j$ .

The value of  $k_j$  is selected from typical values for the type of cooling in use and verified with the help of a thermal network. A value of  $12.1 [kW/m^2]$  was chosen here, considered typical of water cooling in automotive environment.

#### 4.1.2.3 Parametric Design Plane $(x, b)$

The torque-PF design plane is defined after the two normalized design factors  $x$  and  $b$ :

$$x = \frac{r + l_m}{R} \quad (4.6)$$

$$b = \frac{B_{g1}}{B_{fe}} \quad (4.7)$$

The definition is reported in Fig. 4.3. Here  $B_{g1}$  is obtained from (2.8). The former is easily defined as the rotor/stator split ratio, being  $r$  the rotor radius and  $R$  the stator outer radius. The latter factor  $b$  is the ratio of the airgap peak of the fundamental flux density  $B_{g1}$  and the iron peak flux density  $B_{fe}$ .

The airgap flux density  $B_g$  (assumed to be constant under each pole) and the peak of the fundamental are related through the shape factor ( $k_b$ ), defined as in [127]:

$$k_b = \frac{B_{g1}}{B_g} = \frac{4}{\pi} \cdot \sin\left(\frac{\pi}{2} \cdot \alpha_m\right) \quad (4.8)$$

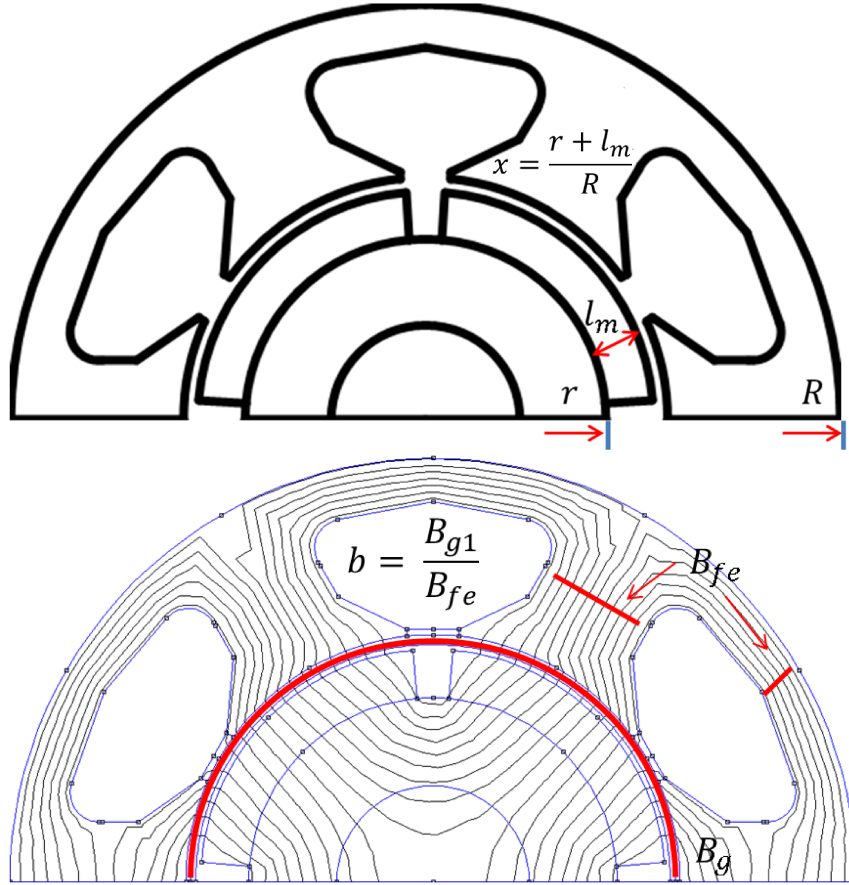
Fig. 4.3 Definition of  $x$  and  $b$

Table 4.1 Ratings of the CW-SPM motor

Machine type	Unit	CW-SPM
Pole pairs ( $p$ )		2
Stator slots		6
Torque target	Nm	120
Maximum speed	rpm	12000
Power target at max. speed	kW	45
Stator diameter ( $D$ )	mm	216
Motor Length ( $L$ )	mm	170
Copper Loss	W	1400
thermal loading ( $k_j$ )	$kW/m^2$	12.1
Airgap	mm	1.5
Copper filling factor		0.55
Steel grade		M250-35A
Steel loading ( $B_{fe}$ )	T	1.5
PM type		BMN-38EH
Remanence ( $B_r$ )	T	1.02 T at 150 $^{\circ}C$
Converter voltage	V pk	173
Converter current	A pk	360
Rotor temperature	$^{\circ}C$	150
Winding temperature	$^{\circ}C$	150

Where  $\alpha_m$  is the magnet pole arc expressed in electrical radians, defined in Fig. 4.4. In this research,  $\alpha_m$  is set to  $5/6\pi$ , for simplicity.

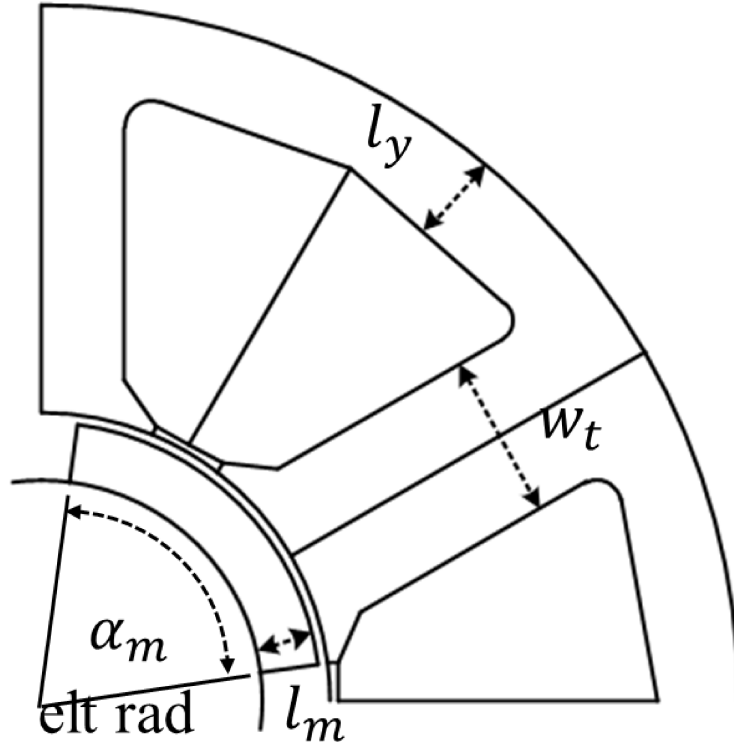


Fig. 4.4 Definition of  $w_t$ ,  $l_y$  and  $l_m$  as a function of design parameters  $x$ ,  $b$

After  $B_{fe}$  is set (for example 1.5 T stands for standard silicon steel sheets), the factor  $b$  defines  $B_{g1}$  and therefore the tooth and back iron widths  $w_t$  and  $l_y$ :

$$w_t = 4\sqrt{2} \cdot 0.5 \cdot D \cdot x \cdot b / (6 \cdot p \cdot q) \quad (4.9)$$

$$l_y = 0.5 \cdot \frac{D}{p} \cdot x \cdot b \quad (4.10)$$

Given the airgap length and the PM remanence, the factor  $b$  also defines the PM length  $l_m$  [80],

$$l_m = k_c \cdot \mu_r \cdot g / \left( \frac{k_b B_r}{B_{fe} b} - 1 \right) \quad (4.11)$$

#### 4.1.2.4 Torque and PF Expressions

Torque and  $PF$  are expressed in terms of the two parameters  $x, b$ , using analytical expressions mutated mostly from [60, 16], reviewed in the following. At low speed the current vector is controlled on the  $q$  axis, in quadrature with the PM flux linkage ( $\lambda_m$ , along the  $d$  axis). Therefore torque is:

$$T = \frac{3}{2} \cdot p \cdot \lambda_m \cdot i_q = \frac{3}{2} \cdot p \cdot \lambda_m \cdot I \quad (4.12)$$

Where  $I$  is the current amplitude. The magnet flux  $\lambda_m$  expressed in terms of  $x$  and  $b$  is:

$$\lambda_m = \frac{\pi \cdot D_{is}/2 \cdot L \cdot N_s \cdot B_{fe}}{\sqrt{3} \cdot p} \cdot x \cdot b \quad (4.13)$$

The current amplitude is a function of the loading factor, the dimensions and the number of turns:

$$i_q = I = \frac{1}{N_s} \sqrt{k_j \cdot \frac{k_{cu}}{\rho} \frac{L}{L + L_{end}} \cdot 2\pi D \cdot A_{slots}} \quad (4.14)$$

Where  $A_{slots}$  is dependent on both  $x$  and  $b$ : when  $x$  becomes larger, the stator area turns to smaller, which means  $A_{slots}$  is lower. The same is valid for  $b$ : a larger  $b$  means thicker teeth and yoke, so smaller slots.  $l_{end}$  in (4.14) is the length of the end turns, that is dependent on  $x$ ,

$$l_{end} = 2l_t + \left( \frac{D_{is} + l_t}{2} \right) \frac{\pi}{p} \quad (4.15)$$

With the current on the  $q$  axis, then  $PF$  is defined as:

$$PF = \cos(\varphi) = \frac{\lambda_m}{\sqrt{\lambda_m^2 + (L_q \cdot i_q)^2}} \quad (4.16)$$

Where  $L_q = L_d = L_s$ , for SPM motor, can also be expressed as a function of  $x$  and  $b$ . The inductance consists of magnetizing inductance  $L_m$  [60], slot leakage

inductance  $L_{slot}$ , and tooth tip leakage inductance  $L_{tip}$ , which are given in (2.23), (2.26), and (2.28).

Then  $L_q$  is the sum of the three portions,

$$L_q = L_m + L_{slot} + L_{tip} \quad (4.17)$$

Finally, the torque and  $PF$  contours are built in the  $x, b$  design plane, using the parametric expressions  $T(x, b)$  (4.12) and  $PF(x, b)$  (4.16). The chart is reported in Fig. 4.5. The subdomain of those solutions in the area with  $PF = 1/\sqrt{2}$  is considered here, highlighted in green in Fig. 4.5. All machines in the green band have a flat power curve and infinite constant power speed range at nominal current. Among those, the ones with a higher torque in the chart will also produce higher output power at high speed. For example, Motor 1 in Fig. 4.5 will give slightly less torque and power than Motor 3.

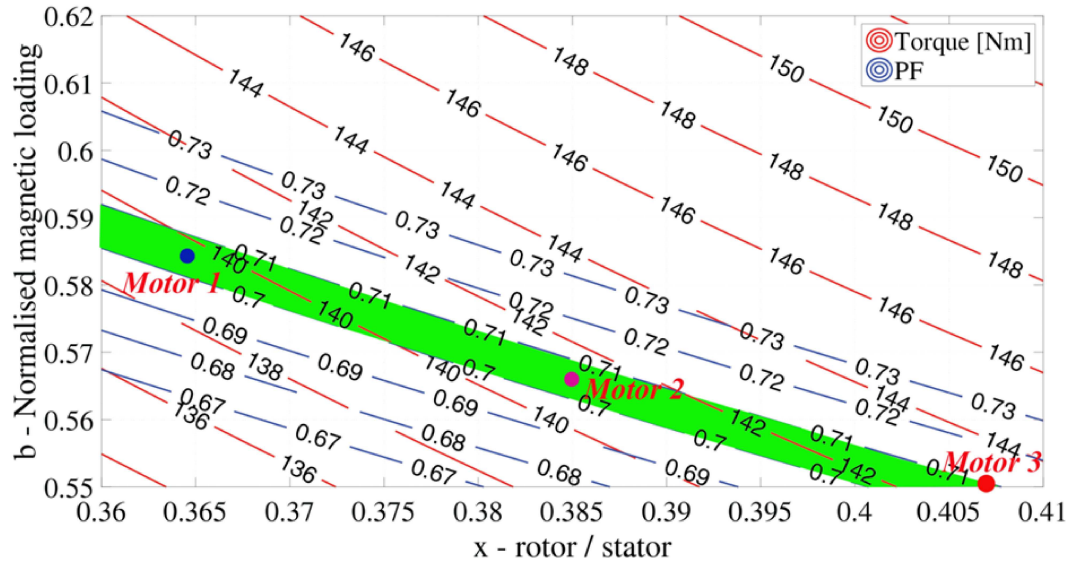


Fig. 4.5  $T(x, b)$  and  $PF(x, b)$  design plane

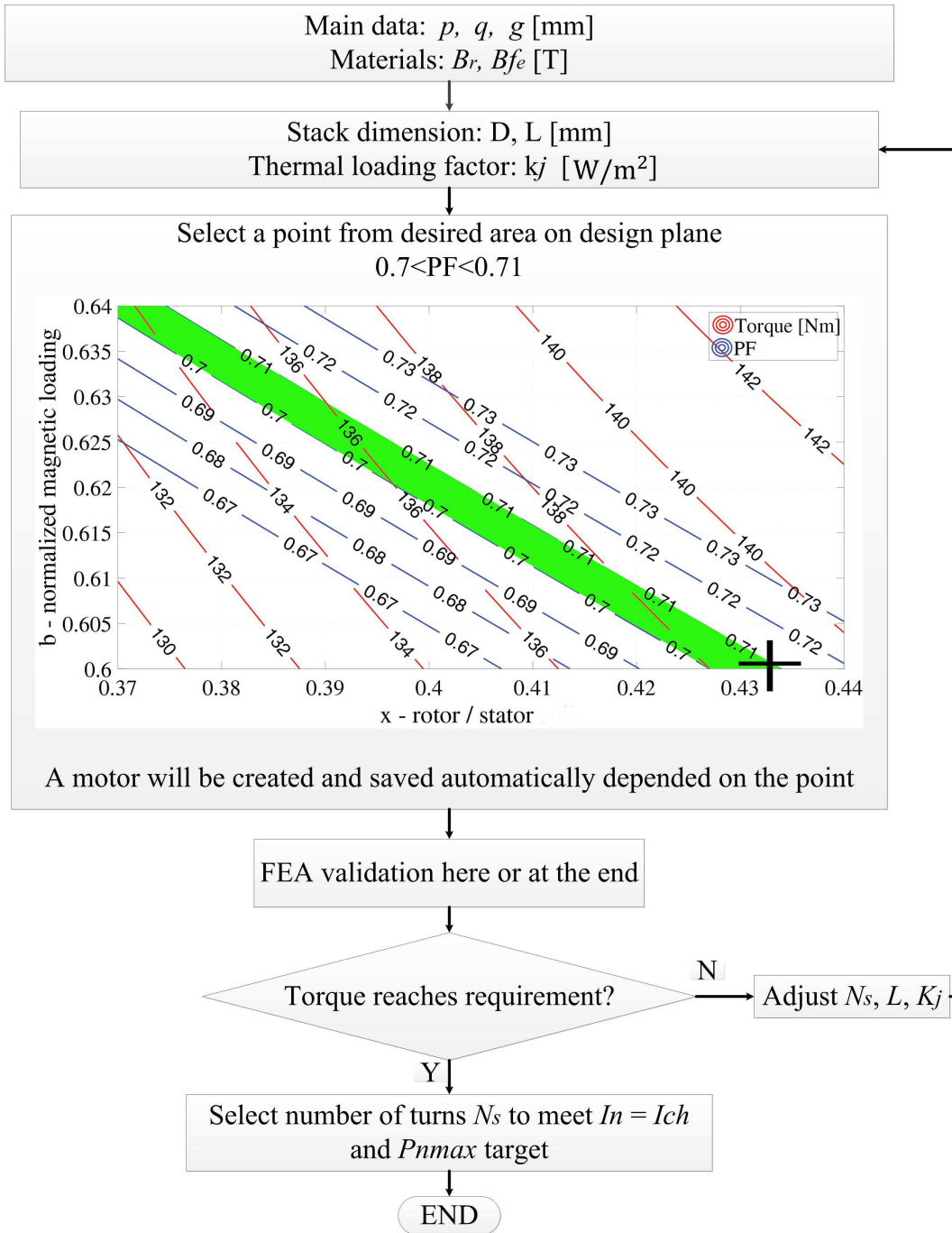


Fig. 4.6 Flowchart of the design procedure for traction motors

#### 4.1.2.5 Design Flowchart

The airgap length is lower-limited by mechanical design considerations [60]. The number of pole pairs is set to two in order to limit the iron and PM losses at high speed. The choice of  $q = 0.5$  is compatible with  $p = 2$ , because other effective fractional slot combinations (e.g.  $q = 2/5, 2/7$ ) would require  $p > 2$  and thus higher rotational loss.

From the aggregate of the inputs, the  $T(x, b) - PF(x, b)$  design plane is built. The region  $0.7 < PF < 0.71$  is the target design area, around the condition  $PF = \sqrt{2}$ . Within this region, the higher torque producing capability can be read from  $T(x, b)$ .

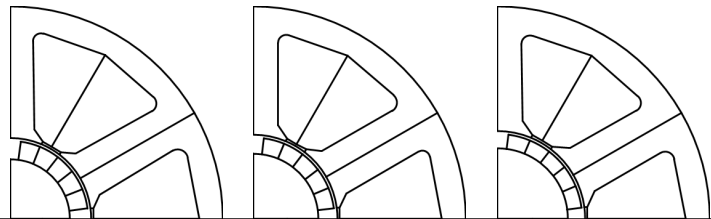
Three feasible designs are selected and analyzed further (motors 1 to 3 indicated in Fig. 4.6). The adopted design software (Syr-e [34]) runs the  $x, b$  procedure and can build the FEA model of any motor seamlessly. A comparison between model and FEA is reported in Table 4.2, showing pretty good agreement. Saturation plays a role in these machines, but do not harm the accuracy of the model. The fulfillment of the torque target can be FEA verified at this moment or at the end. If the target torque is not met, either the stack size ( $D, L$ ) or the loading ( $k_j$ ) should be modified and the process iterated.

After the torque target is met, the tuning of the output power to the target comes very easily through the design of the number of turns  $N_s$ . As shown in (3.5), the loading input  $k_j$  determines the Ampere-turns product  $N_s I$  altogether, but not the number of turns and neither the current alone. Therefore,  $N_s$  is adjusted so that the motor current equals the nominal value coming from (4.1) and (4.2).

$$I_n = P_{nmax} / \frac{3}{2} V_{max} \quad (4.18)$$



Table 4.2 Comparison between estimated and FEA results

Motor Number	1		2		3	
$(x, b)$	(0.363, 0.585)		(0.385, 0.57)		(0.404, 0.55)	
Structure						
$l_m$	11.54		9.41		8	
	Model	FEA	Model	FEA	Model	FEA
Torque	139.6	129.5	141.2	131.1	143	131.3
PF	0.705	0.71	0.706	0.707	0.71	0.701

#### 4.1.2.6 Demagnetization Limit

Magnet thickness must be lower and upper limited to avoid the risk of demagnetization, on the one side, and excess of PM loss, on the other side. If PMs are too thin they tend to demagnetize early with load, whereas if they are too thick the eddy current loss increase without any torque or power output advantage.

The flux density of PM  $B_m$  is assumed to be equal to  $B_g$ . Therefore,

$$B_m \approx B_g = \frac{B_r}{k_b + k_b \cdot k_c \cdot \mu_r \cdot \frac{g}{l_m}} \quad (4.19)$$

From (4.7), (4.8) and (4.19), the ratio  $l_m/g$  determines the airgap flux density and the loading of the magnet. It is:

$$l_m/g = k_c \cdot \mu_r / \left( \frac{B_r}{B_{fe} \cdot b - 1} \right) \quad (4.20)$$

If  $l_m/g$  is limited between 3.5 and 6.5, this turns into a limitation of the range of  $b$ , according to (4.20). With  $B_r = 1.02 \text{ T}$ . This turns into:

$$\frac{1.02}{\frac{k_c \dot{\mu}_r \cdot B_{fe}}{3.5} + B_{fe}} < b < \frac{1.02}{\frac{k_c \dot{\mu}_r \cdot B_{fe}}{6.5} + B_{fe}} \quad (4.21)$$

### 4.1.3 Results

#### 4.1.3.1 Design Examples

Three designs were chosen from the  $(x, b)$  plane of Fig. 4.5, they are shown in Table 4.2. Comparison between model and FEA results is reported in the table. Motor 3 was selected as the best candidate because:

- it has the highest torque forecast.
- It has the largest  $x$  value, therefore the biggest rotor, and the shortest teeth and, ultimately, less copper and shorter end connections. Moreover, it eases thermal exchange from copper to coolant.
- The volume of magnet is the smallest among the three.

The FEA calculated power and torque envelopes of Motor 3 are presented in Fig.4.7. It is shown how the number of turns  $N_s$  modifies the height of the power plateau and not nominal torque. The Ampere-turns product  $N_s I$ , coming from the design input  $k_j$  is the same, so torque is the same. As  $N_s$  decreases, the characteristic current, characteristic power, and base speed all grow (Fig. 4.7). The power requirement is met here when the number of turns decreases from 48 to 40 (45 kW).

## 4.1.3.2 Power and Torque Envelopes

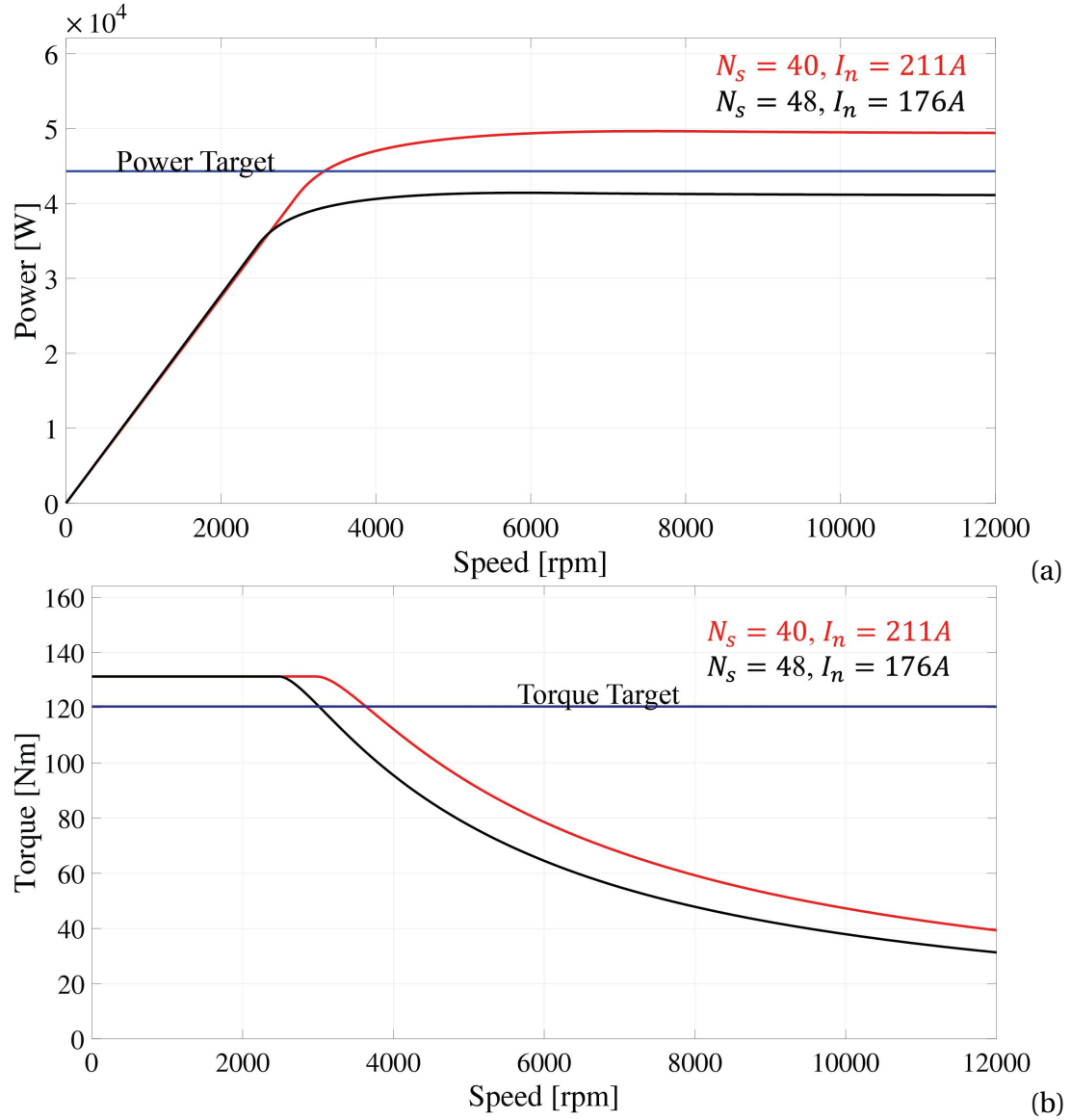


Fig. 4.7 Power (a) and torque (b) profiles of Motor 3, for same  $k_j [W/m^2]$  and different number of turns

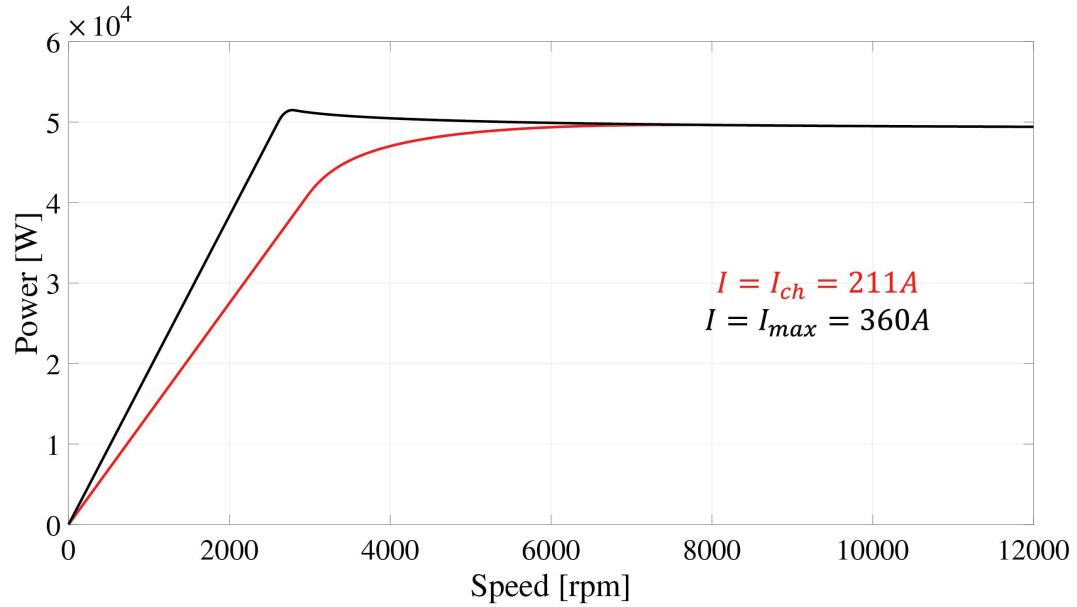


Fig. 4.8 Power profile for Motor 3

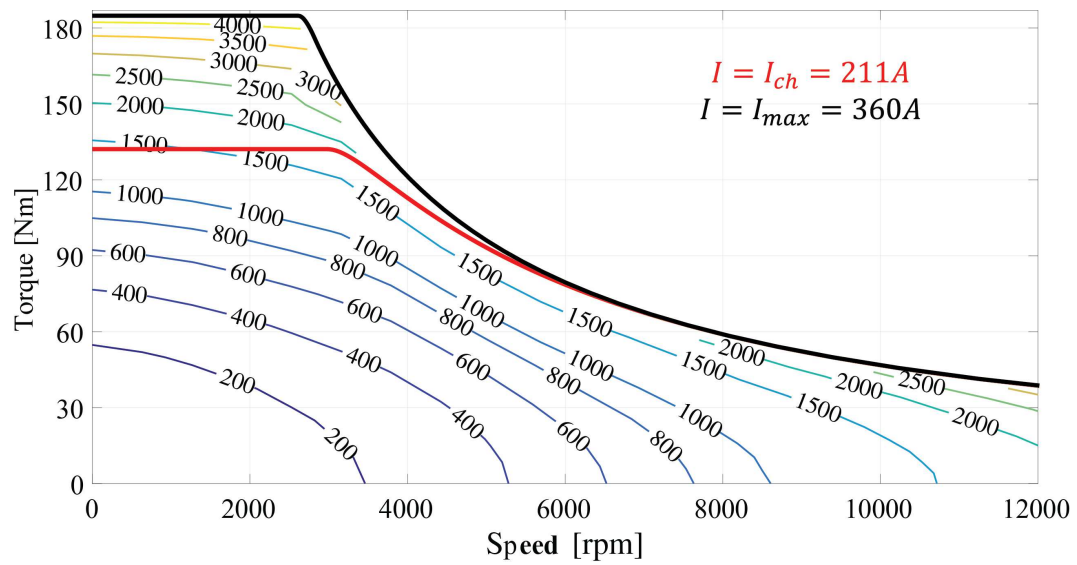


Fig. 4.9 Loss map and torque profile of Motor 3

Although the over-load capability is nearly none, the losses from over-load condition are much higher than those from characteristic or below characteristic conditions (Fig. 4.9). The over-load losses may be more than double the losses from characteristic condition.

Fig.4.10 reports the FEA calculated efficiency map of the final design. Segmentations ( $5 \times 5$ ) are applied for PMs in both circumferential and axial directions to reduce the eddy current effects on PMs. The motor achieves high efficiency over a large proportion of the operating area. Nevertheless, burdened with heavy losses, the efficiency drops under over-load condition or in high speed operating region.

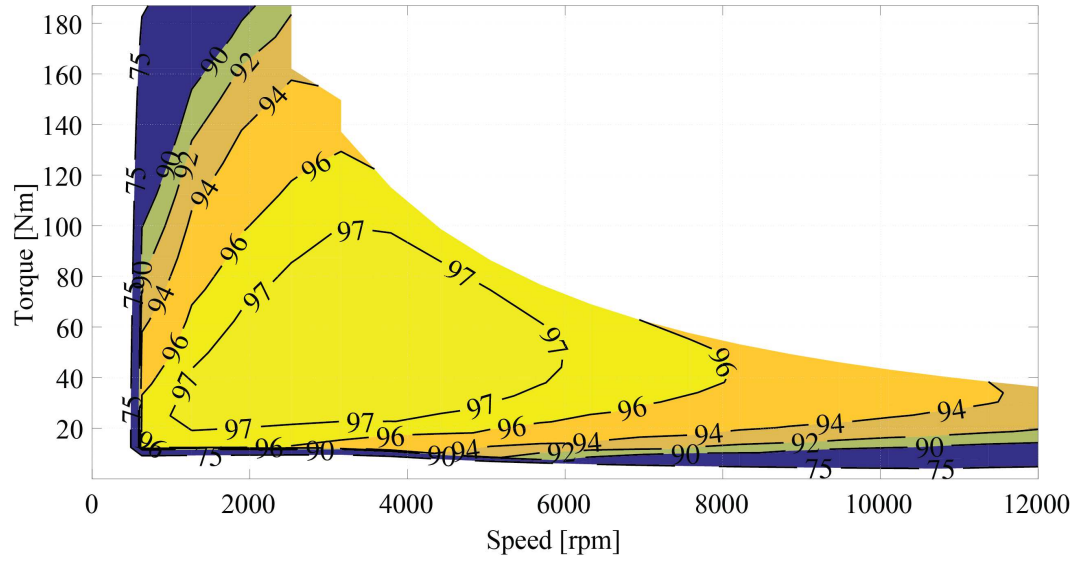


Fig. 4.10 Efficiency map of Motor 3

#### 4.1.4 Design Summary

A straightforward design approach is presented, for CW-SPM machines for traction applications. The  $(x, b)$  design plane is introduced, to match torque requirement and the key design condition of power factor equal to  $1/\sqrt{2}$ . All designed machines have infinite speed flux weakening range. The illustrated design method for CW-SPM machines simplifies the design process, compared with general design procedures. The model used for the parametric design is FEA validated with success. Design equations are comprehensively provided in this research. FEA is also used to characterize the final design and to get to torque/power profiles.

## 4.2 Parametric Design Procedure Based on $(x, l_m/g)$ Plane

Part of the work described in this chapter has been previously published in [128].

### 4.2.1 Design Background

This research proposes a new parametric design method for SPM motors with distributed windings. A new parametric design plane, built on rotor-stator radius split and magnet-airgap length ratio  $l_m/g$ , is introduced. Compared with per unit magnetic loading  $b$ ,  $l_m/g$  is more direct to define the airgap flux density, reported in Fig. 4.12 in next subsection. Moreover, the range span of  $l_m/g$  can easily define the magnet quantity, which also direct relates to the cost.

During the design process, the machine torque capability and power factor (PF) at rated current condition are represented on the parametric plane. The key geometric quantities of the candidate machine are found by selecting the desired torque and PF performance point on the plane. A two-dimensional machine model will be automatically built, ready for FEA verification. In addition, the new method is also suitable for motors with modified PM shape [132] by introducing a magnet shaping factor, resulting in the possibility of torque ripple and cost optimization. The demagnetization limit at the edges of PMs is analyzed. Besides, PM quantity is also considered to decrease the cost. The parametric design procedure simplifies the machine design process for SPM motors, including rounded PM shape, covering abundant magnetic calculations.

The torque smoothness is essentially demanded when the electrical machines are used in precise motion control application [116]. In [131], magnet shaping method was introduced as an effective solution to reduce the torque fluctuation. However, while the magnet length drops at the PM edge, the demagnetization risk is reversely surged. The decrease of electric loading due to the demagnetization issue is not considered in the PM shaping models in [133–135]. In this study, a magnet shaping factor is introduced to define the PM ends length, which is also a straightforward insight to the maximum electric loading against demagnetization task. In addition, the new parametric design method is also suitable for motors with modified PM shape [132], resulting in the possibility of torque ripple and cost

optimization. The demagnetization limit at the edges of PMs is analyzed. Besides, PM quantity is also considered to decrease the cost.

The new parametric design procedure simplifies the machine design process for DW-SPM motors, skipping abundant magnetic calculations. The proposed design method is integrated in machine design software available online, which contains sizing equations, structural analysis, thermal estimation and magnetic static FEA.

In this research, a comprehensive parametric design flowchart is presented. Four SPM motors are designed via the presented parametric method. Two of them have standard radial PMs, and the other two have rounded profiled shapes, respectively. The demagnetization issue of rounded profiled motor is considered. The motor performance results are validated through FEA simulations. Experimental results are presented and compared with FEA outputs for one of the optimized designs. The detailed experimental procedure is also addressed. The main contributions of this research are as follows:

- 1). The design procedure based on the parametric design plane and related design equations.
- 2). The accurate description of the machines with profiled magnets.
- 3). The unified approach to profiled and non-profiled radial magnets, within the same framework, including the demagnetization study.

## **4.2.2 Design Procedure**

### **4.2.2.1 Machine Specification**

This study uses the same stack dimensions and slots-poles combinations as the previous work [132]. The key specifications are reported in Table 4.3.

Table 4.3 Ratings of the DW-SPM machine

Machine type	Unit	DW-SPM
Pole pairs ( $p$ )		3
Stator slots		36
Stator diameter ( $D$ )	mm	175
Motor Length ( $L$ )	mm	110
thermal loading ( $k_j$ )	$kW/m^2$	9.1
Mimimum airgap	mm	1
Copper filling factor		0.532
Steel grade		M600-50A
Steel loading ( $B_{fe}$ )	T	1.6
PM type		NdFeB 32 MGOe
Remanence ( $B_r$ )	T	1.16 T at 20 °C
Rated current	A	25
Number of turns per phase ( $N_s$ )		120

#### 4.2.2.2 Rotor Geometry

Conventionally, the PM length is kept uniform at the airgap. When output torque smoothness is required, the magnet outer profile can be modified as ‘rounded’ to reduce the magnet length at ends. The cross section view of an SPM rotor with rounded magnets is reported in Fig.4.11. The outer profile of the PM is rounded shaped and follows the set of parameters defined in the figure.  $l_m$  is the maximum magnet length at the center of the pole (along with  $d$  axis),  $r$  is the rotor core radius,  $\beta$  is the magnet length at the magnet edge, in  $p.u.$  of  $l_m$ . When  $\beta$  equals to 1, the magnet length at edge equals  $l_m$  and the PM shape becomes uniform.  $\alpha_m$  is the magnet angular span,  $\xi$  is the rotor angular coordinate, starting from the magnet center line,  $g(\xi)$  is the airgap length function of  $\xi$  and  $r_c$  is the radius of the outer rounded magnet profile. After defining the magnet parameters ( $\alpha_m$ ,  $l_m$  and  $\beta$ ), the magnet length distribution  $l_m(\xi)$ ,  $g(\xi)$ ,  $r_c$  and central position  $O'$  of rounded profile are calculated.



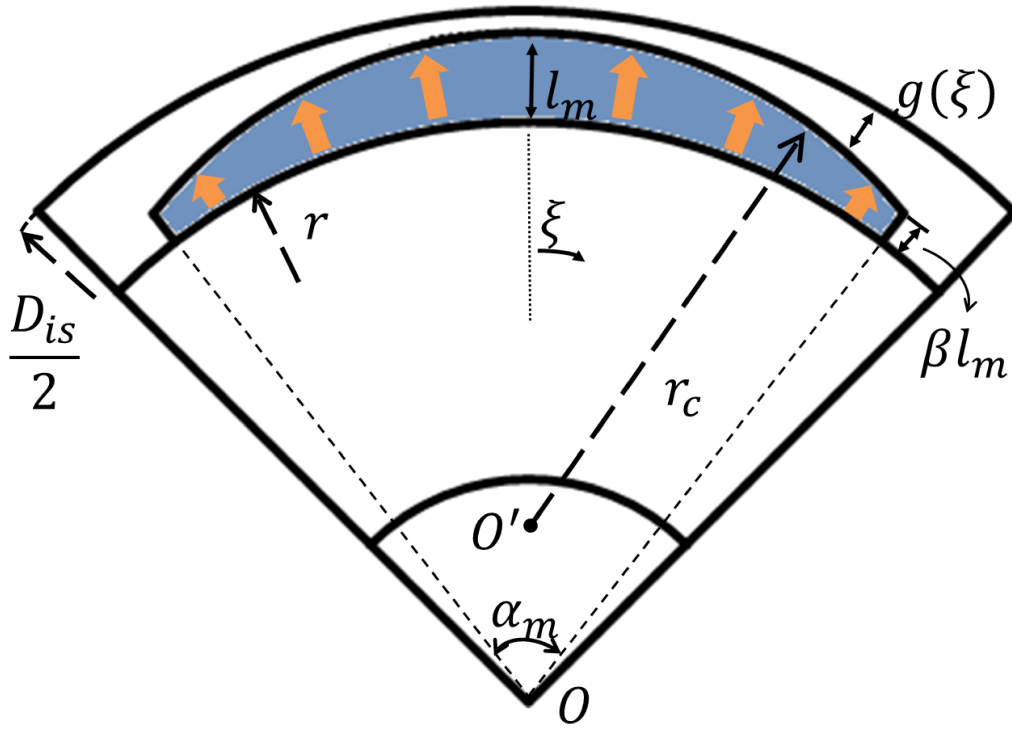


Fig. 4.11 Definition of design parameters for SPM machines

#### 4.2.2.3 Airgap Flux Density

Assuming that the cross sectional areas of PMs and external circuit are equal [60], for a slotless machine with radially magnetized PMs, it is obtained that,

$$B_g(\xi) \approx B_m(\xi) = \frac{l_m(\xi)/g(\xi)}{l_m(\xi)/g(\xi) + k_c \cdot \mu_r} \cdot B_r \quad (4.22)$$

Here  $B_m(\xi)$  is the magnet flux density function. When the PM length is uniform, the average airgap flux density  $B_{g\_avg}$  from (4.22) and one from FEA are compared in Fig. 4.12.

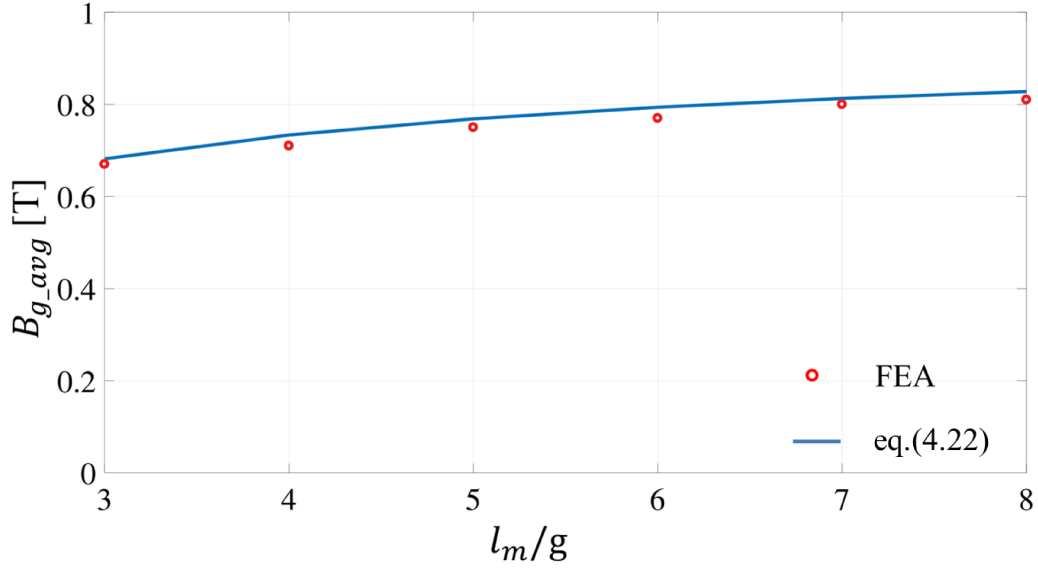


Fig. 4.12  $B_{g\_avg}$  comparison between (4.22) and FEA results

From the figure, the agreement of analytical  $B_{g\_avg}$  and FEA ones also clearly indicates that  $l_m/g$  directly refers to the magnitude of  $B_{g\_avg}$ . When the magnet shaping means is carried out, according to the magnet parameters input ( $l_m$ ,  $\alpha_m$  and  $\beta$ ), the radius of rounded magnet shape  $r_c$  can be achieved as,

$$r_c = \frac{(2r^2 + 2l_m r(\beta + 1))(1 - \cos \frac{\alpha_m}{2}) + (\beta^2 + 1 - 2\beta \cos \frac{\alpha_m}{2}) \cdot l_m^2}{2(r(1 - \cos \frac{\alpha_m}{2}) + l_m(1 - \beta \cos \frac{\alpha_m}{2}))} \quad (4.23)$$

Then, the magnet length expression  $l_m(\xi)$  can be got according to the PM positions,

$$l_m(\xi) = (r + l_m - r_c) \cos \xi - r + \sqrt{r_c^2 + ((r + l_m) \sin \xi - r_c \sin \xi)^2} \quad (4.24)$$

The relationship among stator inner diameter  $D_{is}$ ,  $l_m(\xi)$  and  $g(\xi)$  is given as,

$$l_m(\xi) + g(\xi) + r = D_{is}/2 \quad (4.25)$$

Then substituting (4.24) into (4.25), the airgap length function is then calculated as,

$$g(\xi) = D_{is}/2 - (r + l_m - r_c) \cos \xi - \sqrt{r_c^2 + ((r + l_m) \sin \xi - r_c \sin \xi)^2} \quad (4.26)$$

Combining equations (4.24) to (4.26), the airgap flux density expression  $B_g(\xi)$  can be expressed as,

$$B_g(\xi) = \frac{[(r + l_m - r_c) \cos \xi - r + \sqrt{r_c^2 + ((r + l_m) \sin \xi - r_c \sin \xi)^2}] \cdot B_r}{(1 - k_c \mu_r)(r + l_m - r_c) \cos \xi - r + \frac{k_c \mu_r D_{is}}{2} + (1 - k_c \mu_r) \sqrt{r_c^2 + ((r + l_m) \sin \xi - r_c \sin \xi)^2}} \quad (4.27)$$

Three cases of airgap flux density distribution  $B_g(\xi)$  waveforms are reported in Fig. 4.13. The analytical results are presented in continuous lines and the circle marked points represent the FEA results. It can be seen that the analytical results agree with the FEA results along with the PM areas. Nonetheless, influenced by fringing effect, in the regions without PMs, the flux density cannot vanish, as indicated by the FEA results. The proposed mathematical model (4.27) assumes the airgap flux density to be zero off the magnet pole, with minor effect on torque and  $PF$  prediction.

The fundamental component's amplitude  $B_{g1}$  is obtained by Fourier transform of the analytical flux density distribution  $B_g(\xi)$  over one pole pair. The magnet flux linkage  $\lambda_m$  is evaluated considering the fundamental component of the airgap flux density and neglecting higher order harmonics. Then  $\lambda_m$  is calculated by (4.28).

$$\lambda_m = \frac{2(r + l_m + g) L N_s k_w B_{g1}}{p} \quad (4.28)$$

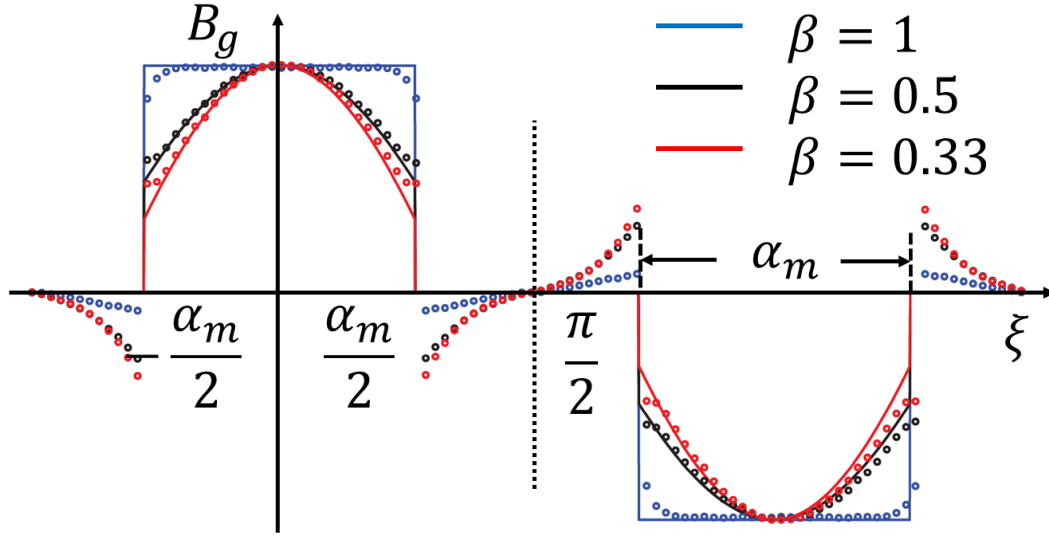


Fig. 4.13 Airgap flux density distribution of a slotless motor, analytical results: continuous lines; FEA results: circle marked

The spectrum of  $B_g$  on different  $\beta$  values from FEA results are reported in Fig. 4.14. As  $\beta$  decreases, the higher harmonics content reduce significantly. On the other hand,  $B_{g1}$  also shrinks as  $\beta$  goes down, implying the reduction on torque production, which will be discussed later. Table 4.4 summarizes the difference between analytical and FEA results on both  $B_{g1}$  and  $\lambda_m$ . The agreement of the results is reasonably good for all considered values of the parameter  $\beta$ .

Table 4.4 Comparison between analytical model and FEA

$l_m = 4.5mm$				
$g_{min} = 1mm$				
$\alpha_m = 171^\circ$				
$B_{g1}[T]$	Model	0.93	0.98	1.14
	FEA	0.93	0.97	1.07
	Error	0 %	1%	6%
$\lambda_m[Vs]$	Model	0.45	0.47	0.54
	FEA	0.46	0.48	0.53
	Error	-2 %	-2%	2%

As  $\beta$  decreases, both fundamental and subharmonics are reduced. The spectrum of three  $B_g$  situations on different  $\beta$  are reported in Fig.4.14

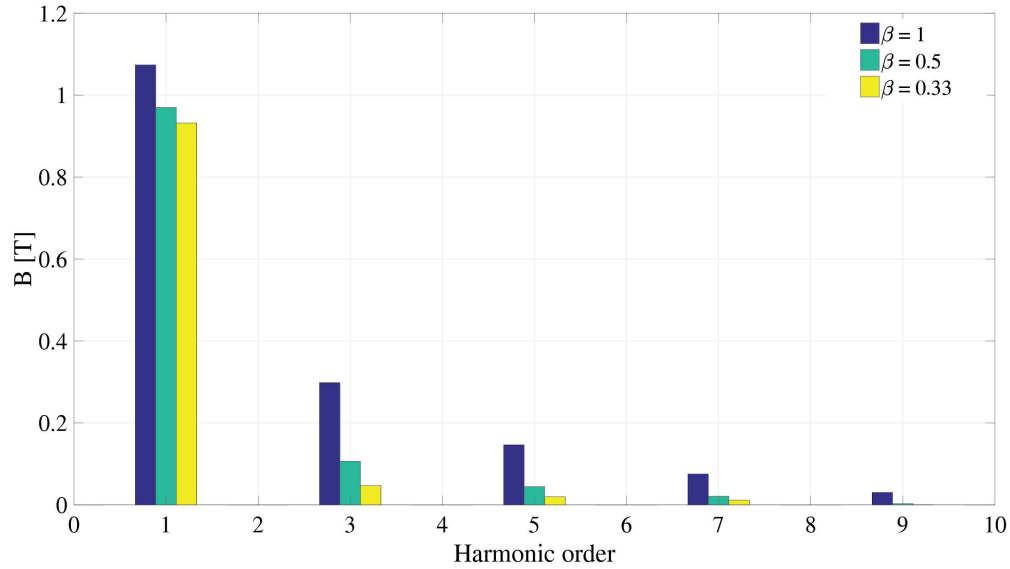


Fig. 4.14  $B_g$  spectrum of different  $\beta$

#### 4.2.2.4 Design Input

The slot-pole combination is constant in this study and the initial design inputs are:

- Number of pole pairs  $p$ .
- Number of slots per pole per phase  $q$ .
- Stack dimensions  $D$ ,  $L$  and airgap length  $g$ .
- PM remanence  $B_r$  and peak flux density in steel  $B_{fe}$ .
- Thermal loading  $k_j$ .

#### 4.2.2.5 Parametric Design Plane $(x, l_m/g)$

The torque- $PF$  design plane is defined after the two key factors of SPM motor,  $x$  and  $l_m/g$ .  $x$  is defined as the split ratio of the machine, shown in (4.6).

From (4.22), the airgap flux density distribution  $B_g(\xi)$  directly refers to the magnet on airgap ratio  $l_m/g$ . Therefore,  $x$  and  $l_m/g$  together determine  $B_g(\xi)$ ,  $B_{g1}$  and  $\lambda_m$ , according to (4.27) and (4.28).

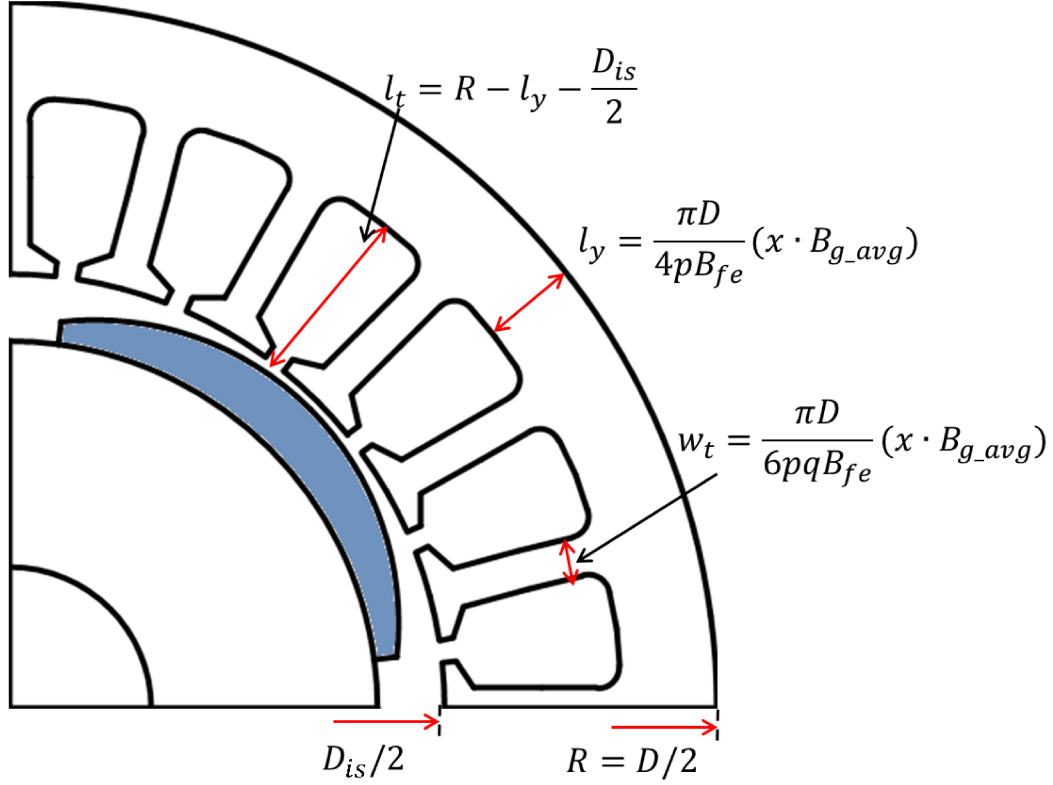


Fig. 4.15 Stator geometry definition

Afterwards, the stator geometry is dependent on the ratio of  $B_g(\xi)$  to steel loading  $B_{fe}$ . Since  $B_{fe}$  is defined at the beginning (1.5 T for standard silicon steel type), the dimension of tooth width and yoke length can be achieved as the product of average  $B_g(\xi)$  and  $x$ ,

$$w_t = \frac{\pi \cdot D}{6 \cdot p \cdot q \cdot B_{fe}} \cdot (x \cdot B_{g\_avg}) \quad (4.29)$$

$$l_y = \frac{\pi \cdot D}{4 \cdot p \cdot B_{fe}} \cdot (x \cdot B_{g\_avg}) \quad (4.30)$$

The detailed stator geometry definition is shown in Fig.4.15.

### 4.2.2.6 Torque and PF Expressions

The torque,  $PF$ , magnet flux density, inductance, current and end length definition are same as  $(x, b)$  plane, shown in (4.12), (4.16), (4.17), (4.13), (4.14), and (4.15).

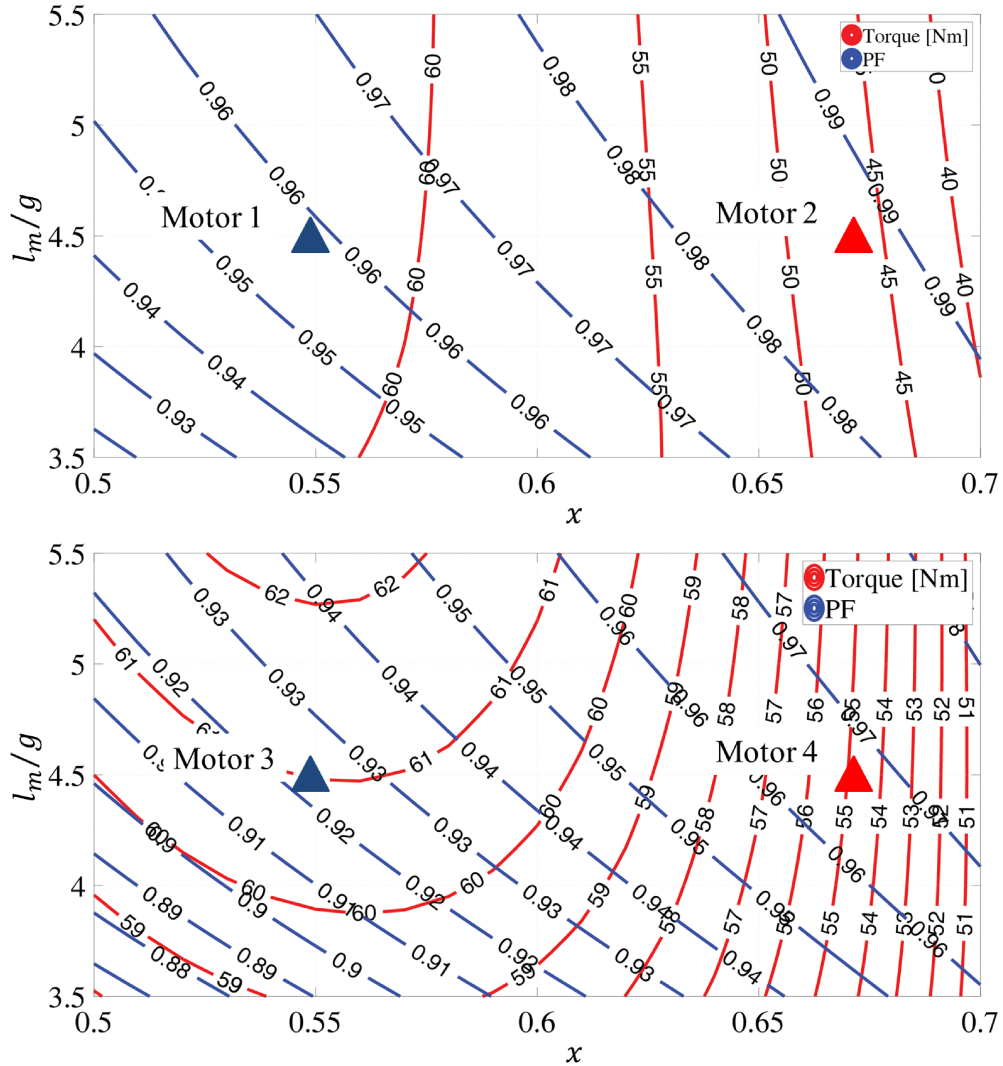


Fig. 4.16 Torque and PF design plane,  $\alpha_m = 171^\circ$ , (a).  $\beta = 1$ , (b).  $\beta = 0.33$

### 4.2.2.7 Flowchart

Two plane examples are reported in Fig. 4.16. Subcase (a) refers to radial magnets with uniform length ( $\beta = 1$ ), case (b) has  $\beta = 0.33$ . For both planes,  $\alpha_m$  is set as  $171^\circ$ . Each point on this plane represents one motor design. One design can be

selected according to the desired torque and  $PF$  output. After one point is picked from the plane, one motor model will be automatically built, on the basis of the equations described above. FEA validation follows, to verify whether the motor is in line with the specified performance. The detailed design flowchart is reported in Fig. 4.17.

After FEA validation at rated current condition, if the torque result is not adequate for the target, stack size or thermal loading can be improved to increase the torque generation. Meanwhile, if the torque ripple is still high, reducing  $\beta$  or finding better PM angular span  $\alpha_m$  is needed. Then the process is repeated.

The PM ends should not be too thin to prevent fractures in the manufacturing process and demagnetization. The PM ends are vulnerable to demagnetization risk, compared with PM center both for their reduced length and for the effect of the stator current aligned with the  $q$  axis, whose magneto motive force (mmf) has the peak value in the area of minimum magnet thickness. Therefore, the edge length must be lower constrained by means of the parameter  $\beta$ . The maximum airgap flux density produced by current alone at the magnet's edges is,

$$B_{g,iq} = \frac{F_p \mu_0}{g} \frac{4}{\pi} \frac{\mu_0 k_w N_s i_q}{2p[l_m(\xi = \frac{\alpha_m}{2}) + \mu_r k_c g(\xi = \frac{\alpha_m}{2})]} \quad (4.31)$$

To protect the PMs, they must be designed so that the flux density (4.31) is equal or larger than the minimum allowed flux density of the PMs  $B_d$ , corresponding to the knee point of the magnet demagnetization curve. Hence,

$$B_m(\xi = \frac{\alpha_m}{2}) \geq B_{g,iq} + B_d \quad (4.32)$$



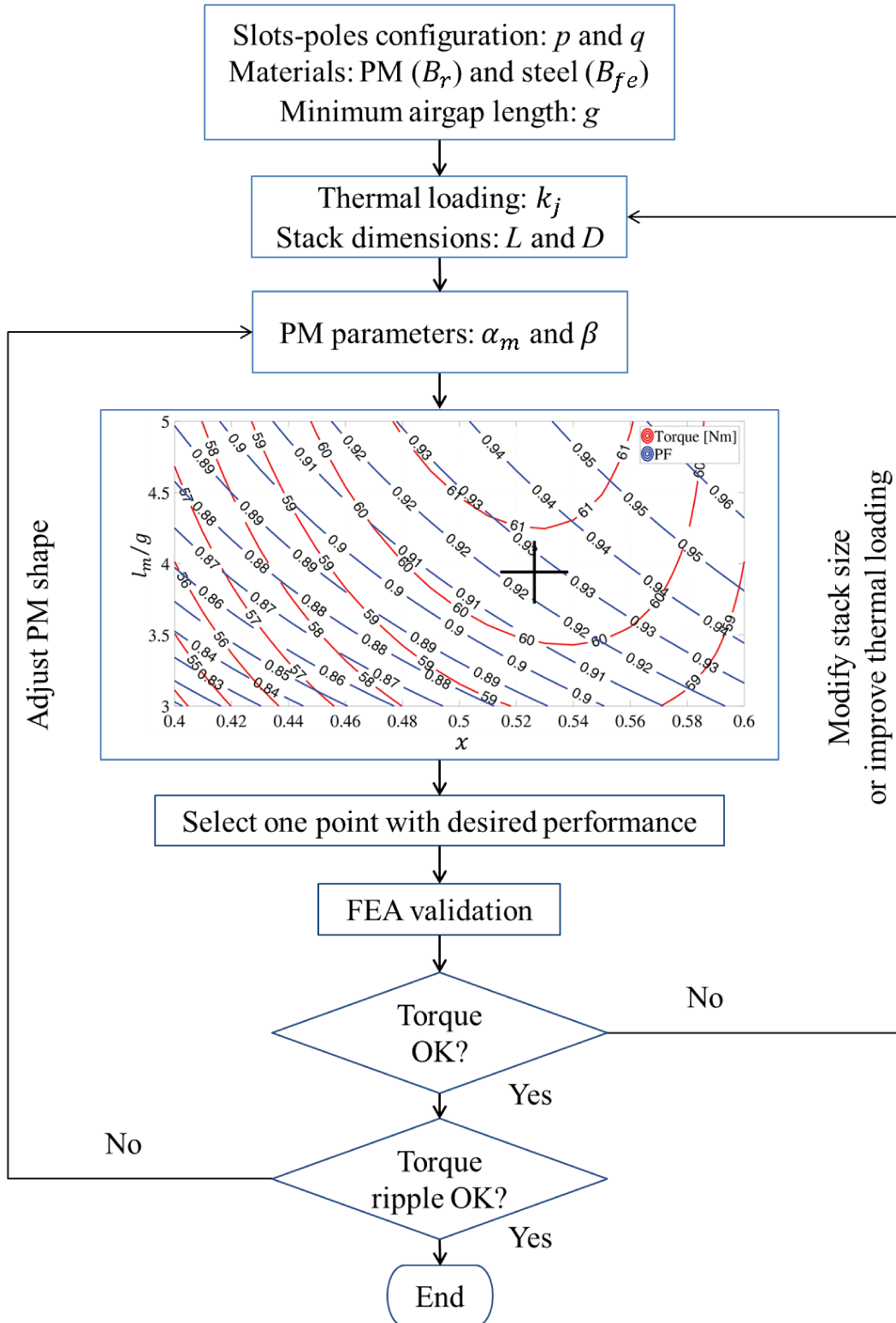


Fig. 4.17 Flowchart of the design procedure

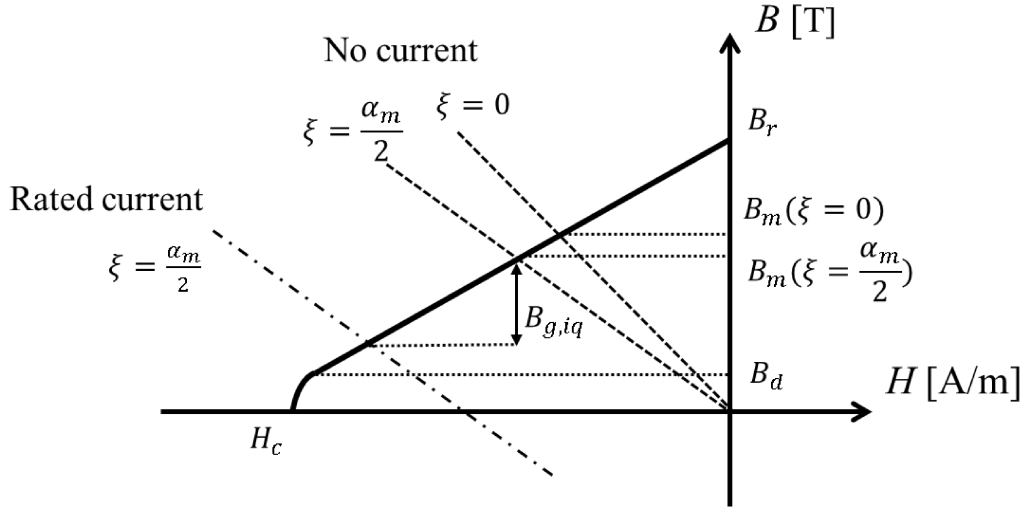


Fig. 4.18 Operating point determination with demagnetization limit (NdFeB 32 MGOe at 80 °C)

The  $B$ - $H$  curve and the relationship (4.32) are graphically associated in Fig. 4.18. In this study,  $B_d$  is 0.1 T and the maximum allowed current  $I_{max}$  is 26 A. Moreover, Fig. 3.16 represents the relationship among maximum allowed current and  $\beta$ , with  $l_m$  as a parameter. The figure illustrates that the maximum current is proportional to the shaping factor  $\beta$  when  $l_m$  is fixed. For this design, acceptable values of  $\beta$  are above 0.33.

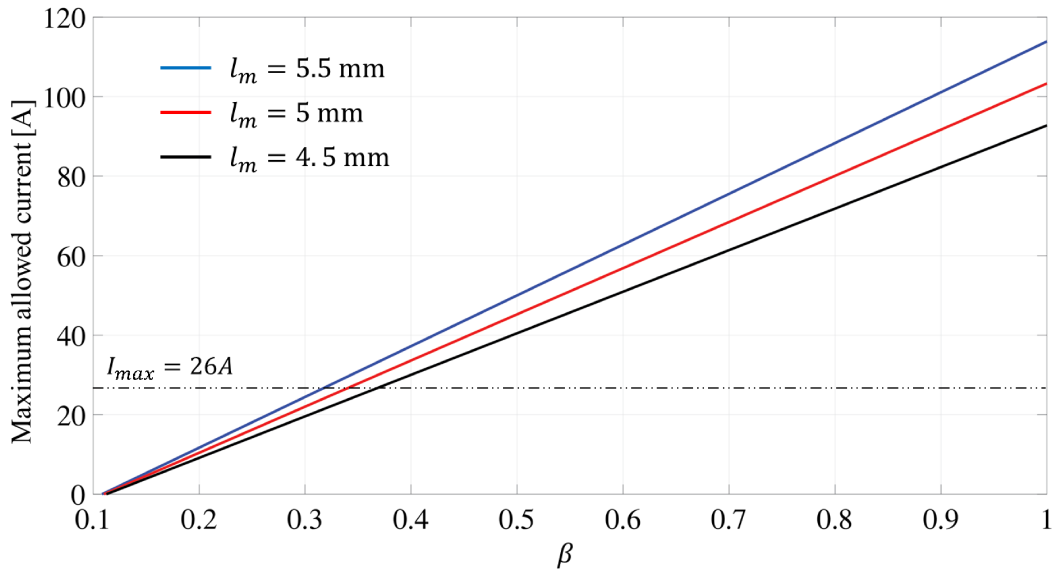


Fig. 4.19 Relationship among  $\beta$ ,  $l_m$  and maximum allowed current

### 4.2.3 Results

The proposed parametric method is tested here by comparing the outcome of analytical calculation in the parametric plane (Fig. 4.16) with FEA simulation and experimental results. Starting from the data reported in Table 4.3, two machines are designed from Fig.4.16a, having uniform magnet length. Other two designs are created from Fig. 4.16b, with rounded magnet shape ( $\beta = 0.33$ ), using the same  $x$  and  $l_m/g$  combinations used for the previous designs, with uniform length. All the motors are parallel magnetized.

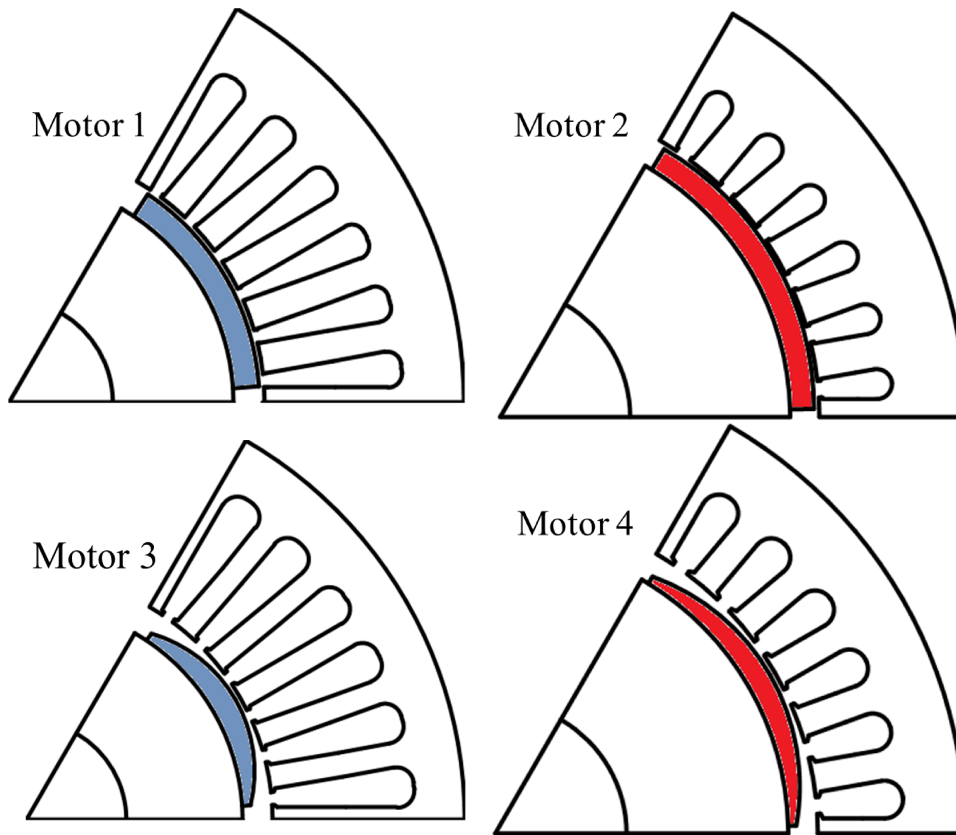


Fig. 4.20 Model view from parametric planes in Fig.4.16

#### 4.2.3.1 Design Examples

Fig. 4.20 presents the structure of the four models selected from each design plane reported in Fig. 4.16. It is obvious from Fig. 4.20 that as  $x$  grows up, slot area becomes smaller when  $l_m/g$  is kept constant (from Motor 1 to Motor 2, and Motor

3 to Motor 4). Considering the same  $x$  and  $l_m/g$  combination, rounded motors will have shorter stator yoke and tooth width, since their  $B_{g1}$  are less than those of uniform length motors (comparing Motor 1 with Motor 3, or Motor 2 with Motor 4). It is emphasized here that although the PM quantity is reduced from Motor 2 to Motor 4 due to the magnet shaping, the slot area is increased. Consequently, the nominal torque produced by Motor 4 is greater than Motor 2, despite of lower PM volume. The entire rotor view of Motor 4 is shown in Fig. 4.21.

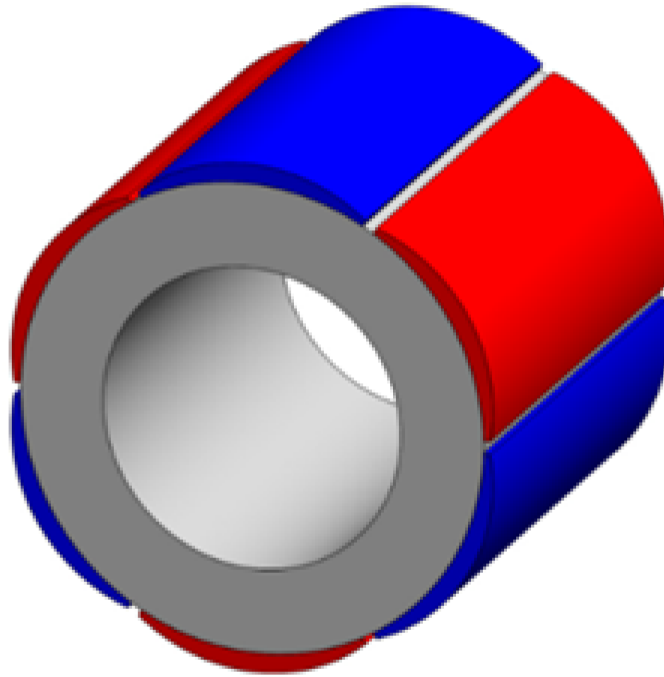


Fig. 4.21 Rotor view of Motor 4

#### 4.2.3.2 FEA Simulation Results

All the models are evaluated under each rated condition via FEA simulations. Results comparison between parametric model and FEA results are reported in Table 4.5, the torque ripple is measured by peak-peak value.

Table 4.5 illustrates that the models built from parametric plane have good agreements with FEA results in terms of both torque and PF, which, in return, validates the analytical equations used in the design stage. Since the rounded shape motor has an approximate sinusoidal airgap flux distribution, the torque

ripple has been significantly reduced, compared with uniform PM length motors. It is emphasized that the nominal rated current of Motor 3 from the design plane is 33 A, however, due to the demagnetization limit, the maximum allowed current cannot be beyond 26 A. At the same current level with Motor 4 ( $i_q = 25\text{ A}$ ), the torque output of Motor 3 is limited. The demagnetization validation process is skipped during the design procedure for uniform PM shape motors. The torque waveforms of four motors over one entire electric period at each nominal rated or allowed current condition are presented in Fig.4.22.

Table 4.5 Comparison between parametric and FEA results

$l_m/g = 4.5$		Torque [Nm]	PF	$i_q$ [A]	Torque ripple [Nm]	
$\beta = 1$	$x = 0.55$	plane	61	0.96	28	-
		FEA	58	0.96	28	5.5
	$x = 0.67$	plane	52	0.98	19	-
		FEA	50	0.99	19	5.3
$\beta = 0.33$	$x = 0.55$	plane	59	0.93	33	-
		FEA	43	0.96	25	1
	$x = 0.67$	plane	55	0.96	25	-
		FEA	52.3	0.96	25	1.8
		exp.	52.2	0.95	25	3.9

Motor 4 was selected as the motor candidate since it has much better torque ripple performance at rated current condition and lower PM quantity (i.e. cost) compared with uniform PM thickness machines (Motor 1 and Motor 2); and it is more robust to demagnetization risk and it has less copper quantity (so, lower cost), compared with Motor 3.

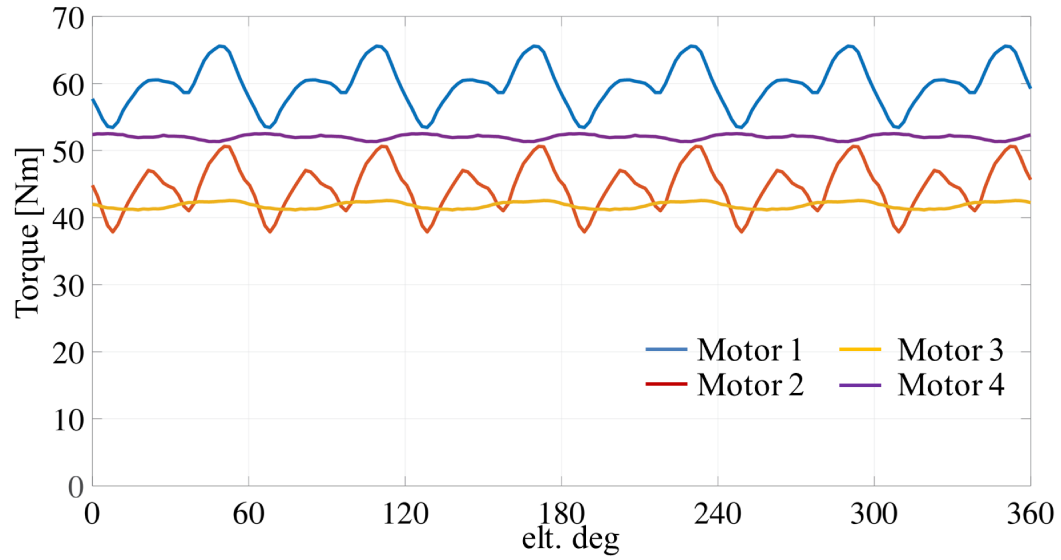


Fig. 4.22 Torque waveforms of the four motors

#### 4.2.3.3 Experimental Validation

The candidate of rounded SPM motor (Motor 4) has been built and tested. Fig. 4.24 shows the test rig setup: it is composed by a speed control driving machine (DM), the current controlled candidate machine under test (MUT) and a data recorder, which stores the status of current, voltage, torque (measured by a torque meter) and speed information of MUT. The setup of experimental scheme is reported in Fig. 4.23.

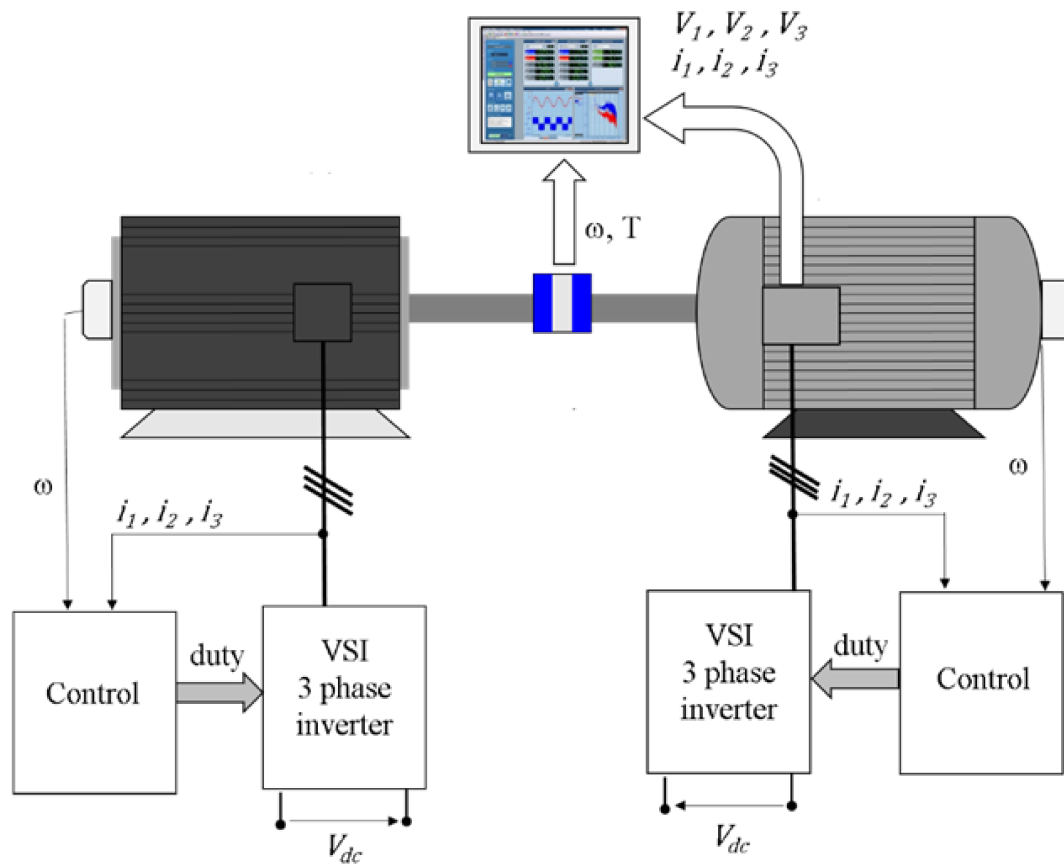


Fig. 4.23 Experimental scheme

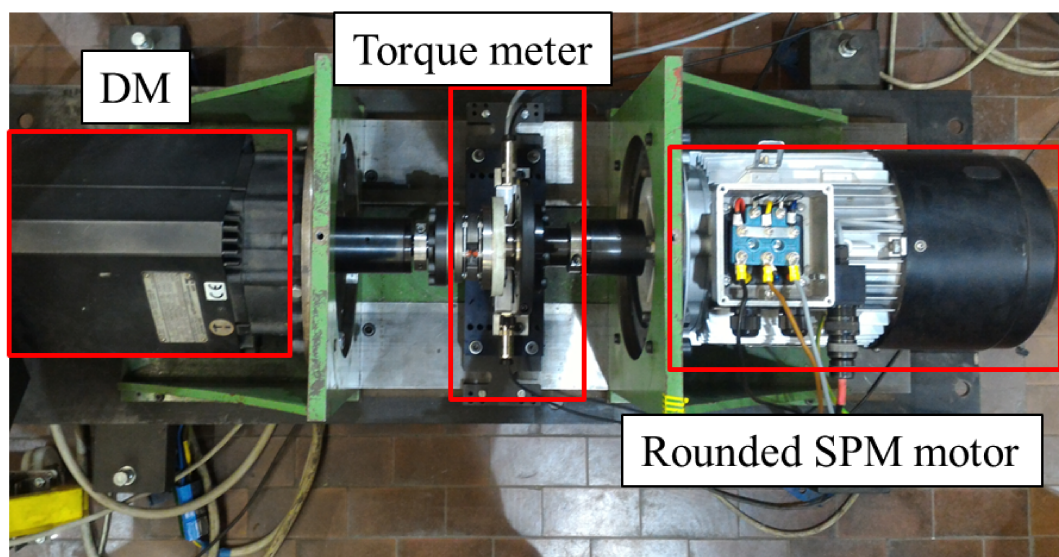


Fig. 4.24 Test bench for rounded SPM motor

Magnetic model identification is performed, with the procedure described in [136]. During the test, also the torque over entire current domain is measured, for validation purpose. At the end of the test, the torque-current curve along Maximum Torque per Ampere (MTPA) trajectory is obtained and compared with FEA simulations and the parametric plane estimation. This comparison is reported in Fig. 4.25.

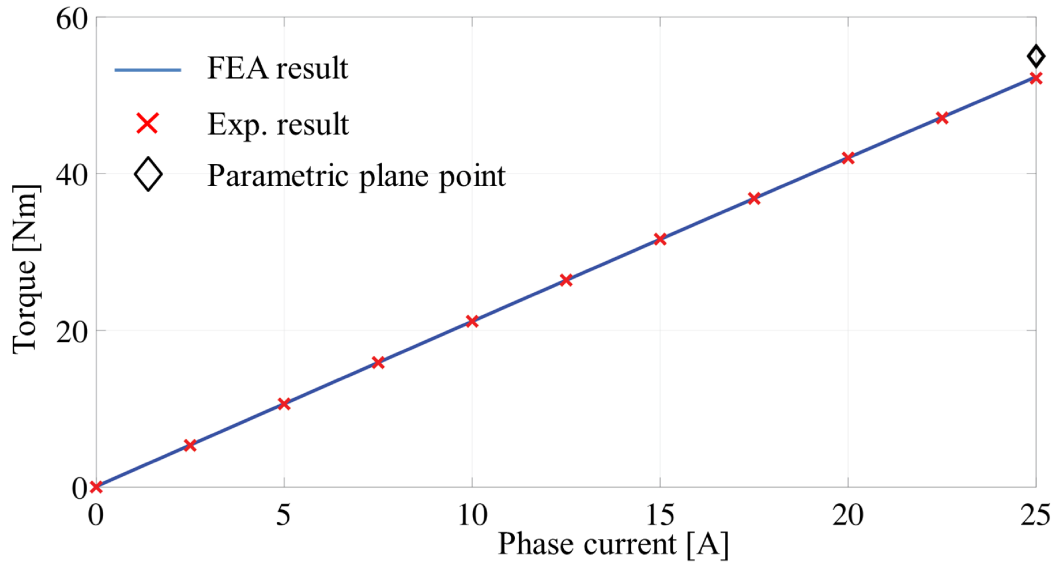


Fig. 4.25 Torque-current curve along MTPA route comparisons among FEA, experimental results and design plane

The torque and PF contours from experimental validation are reported in Fig. 4.26.  $i_d$  current ranges from -25A to 25A and  $i_q$  is from 0 to 25A. The MTPA route are presented in both figures.

Table 4.5 shows the analytical, FEA and experimental results. The expected performances of torque and  $PF$  are confirmed by both FEA and experimental measurements.



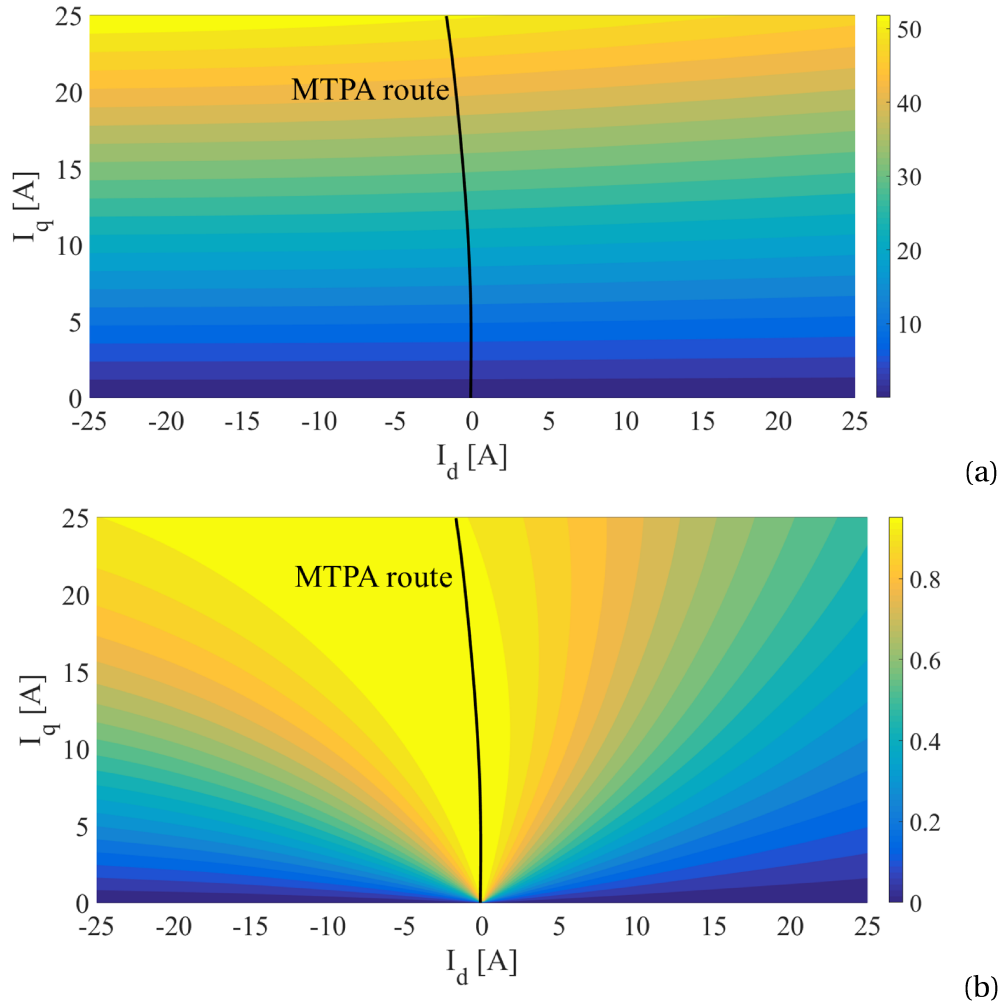


Fig. 4.26 Torque (a) and PF (b) maps the from experimental test

The torque ripple results from both FEA and experiment are reported in Fig. 4.27, at three different current levels, i.e. 12.5 A, 18.8 A and 25 A. The black continuous curves represent FEA results over one entire electrical period and the colored waveforms are obtained by the torque meter shown in Fig. 4.24. The machine speed is at 10 rpm for torque ripple test. The sampling frequency is 100 kHz. At 25 A level, the torque ripple from experiment is 3.9 Nm, which is larger than FEA simulation results. At other current levels, the ripples from test are also more obvious than FEA results, since the sensitivity of the torque meter cannot be as precise as FEA.

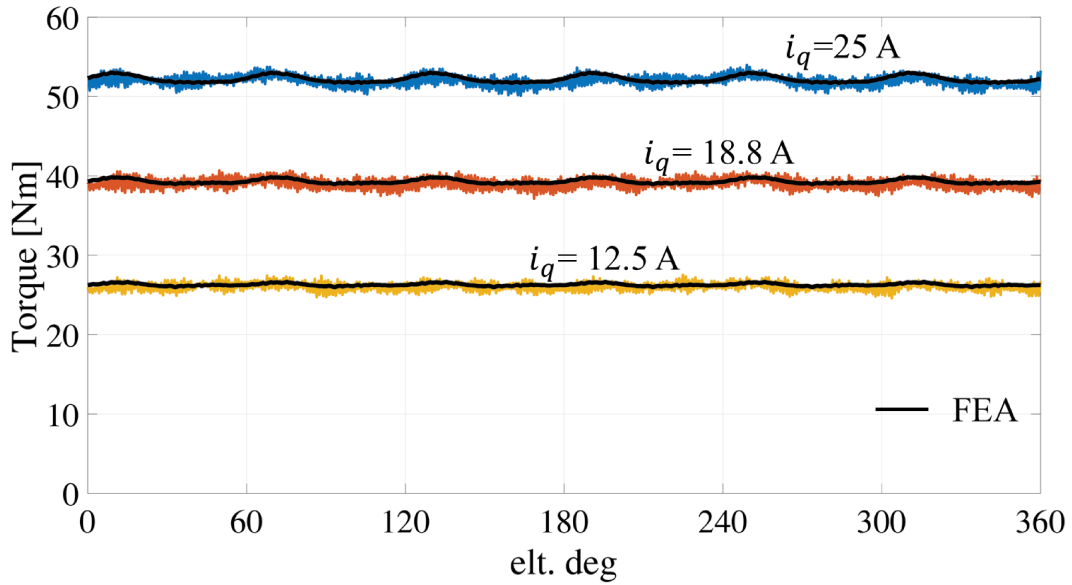


Fig. 4.27 Torque ripple results

#### 4.2.4 Design Summary

A new parametric design method for SPM motors has been presented. The presented method applies to magnets of radial shape and also to rounded shape magnet, for cogging and torque ripple minimization.

A straightforward outer rounded magnet model is presented; the demagnetization study on the magnet ends length is discussed. Two motor models of each uniform and rounded SPM machines are selected as examples and validated by FEA simulation results, showing good agreement with estimated performance. Concerning about demagnetization risk, the parametric design method on rounded SPM machines needs more attention on the limited electric loading. One qualified rounded machine is tested. The experimental measurements on torque and PF performance of the rounded shape SPM motor prototype are presented. The torque ripple test is also presented.

## 4.3 Parametric Design Procedure Based on Subdomain Model

### 4.3.1 Design Background

Analytical calculation on airgap flux distribution of PMSMs has been highly developed during last decades [129]. An analytical model for magnetic field solution for the slotless SPM machine is introduced in [137]. The interaction effect between the pole transitions and slot openings is included in [138, 139]. Accurate subdomain models for magnetic field calculation for SPM motor through scalar and vector potential distributions methods based on 2-D model are presented [140, 141]. According to vector potential distribution model, winding losses at no load condition are calculated in [142, 143].

In order to reduce the cogging torque of SPM machines, magnetic field distributions with subdomain model of shaped magnet model of SPM machines are also shown in [135, 144, 145]. Beside magnet shaping method, analytical solution on auxiliary and skewed slots are also introduced [146, 147]. Except SPM machines, subdomain model is also applied to surface inset permanent magnet machine in case that high saliency and wide speed range are pursued [148, 43].

In view of the design process of the SPM machines, a general design approach for SPM machines has been illustrated in [81]. A parametric design technique for SPM machines with both distributed and concentrated windings has been proposed in [120, 128]. In these papers, a parametric design plane, built on rotor-stator radius split and magnet-airgap length ratio, are introduced. During the design process, the machine torque capability and PF at nominal rated current condition are represented on the parametric plane. The key geometric quantities of the candidate machine are found by selecting the desired torque and PF performance point on the plane. Then, a 2-D machine model will be automatically built, ready for FEA verification. In the parametric design process, steel loading  $B_{fe}$  is set at initial step to define stator sizing, including tooth width and stator yoke length.

The analytical solution for the SPM machines is used on computing airgap flux distribution on the existed motor models. This study focuses on combining parametric design process with subdomain models and implementing the

analytical model in the design process to increase the steel loading accuracy on both stator teeth and yoke, in return, improving both stator sizing accuracy and motor efficiency. The new method highly increases the accuracy of the parametric plane without consuming redundant time. Both CW and DW SPM machines with different pole-slot combinations are discussed and validated by FEA. The design procedure can be easily followed and repeated on SyR-e.

### 4.3.2 Design Procedure

#### 4.3.2.1 Airgap Flux Model

In [60], a simplified formula to get the maximum airgap flux density of a slotless machine is expressed as,

$$B_g = \frac{l_m/g}{l_m/g + \mu_r} B_r \quad (4.33)$$

From the expression, it can be seen that the airgap flux density distribution is mainly dependent on the magnet-airgap length ratio  $l_m/g$ .

An improved slotless SPM model has been illustrated in [137], for both parallel and radial magnetization. In this model, the airgap flux density distribution  $B_g$  along one pole pair is introduced. Base on magnet-airgap length ratio  $l_m/g$ , the calculated maximum airgap flux densities are accurate, for both simplified and improved models, compared with FEA results, shown in Fig. 4.28.

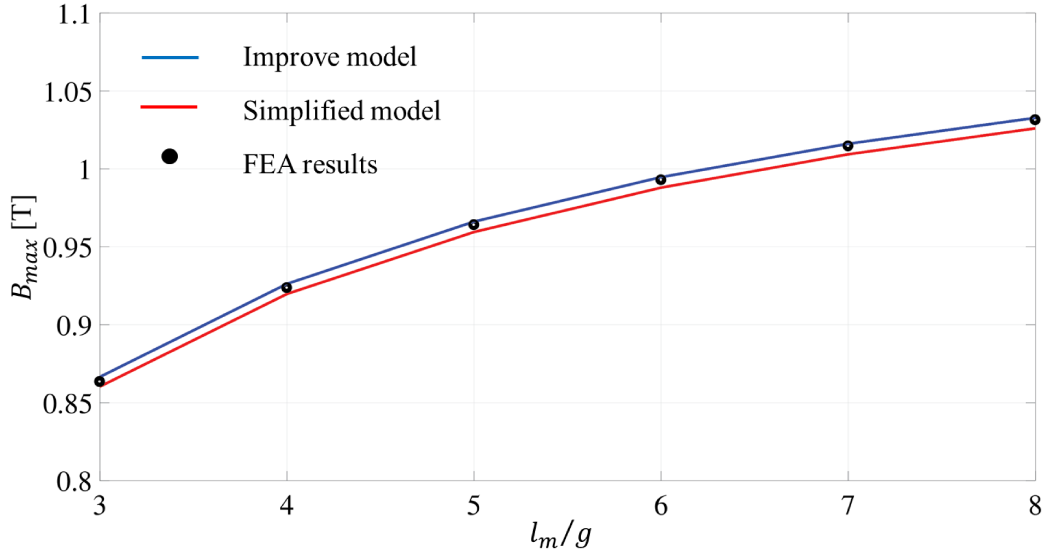


Fig. 4.28 Comparisons among simplified, improved models and FEA results on maximum airgap flux density, parallel magnetization

When the slot effect is taken into account, Carter coefficient  $k_c$  is introduced into (4.33) to consider flux density reduction on the slots. Then the simplified model (4.33) is modified as,

$$B_g = \frac{l_m/g}{l_m/g + k_c \cdot \mu_r} \cdot B_r \quad (4.34)$$

Since the airgap flux density reduction in each slot is not equal, (4.34) is only suitable for average  $B_g$  over one pole rather than the maximum one.  $B_g$  distribution along each slot pitch cannot be achieved in this model.

#### 4.3.2.2 Subdomain Model

To obtain more accurate  $B_g$  distribution based on different rotor positions and slot effect, an improved subdomain analytical model is presented and developed in [140–143, 135, 144]. In this model, the machine is divided into four different regions, i.e. PMs, airgap, slot and slot opening. According to the vector potential distribution and boundary conditions, the radial  $B_{gn}$  and tangential  $B_{gt}$  components of  $B_g$  can be obtained for a specific rotor position. A simplified motor

view with 4 poles ( $p = 2$ ) and 6 slots ( $q = 0.5$ , number of slots per phase per pole) is shown in Fig. 4.29. The main process to figure out  $B_{gt}$  and  $B_{gn}$  derived from vector potential equations is presented here.

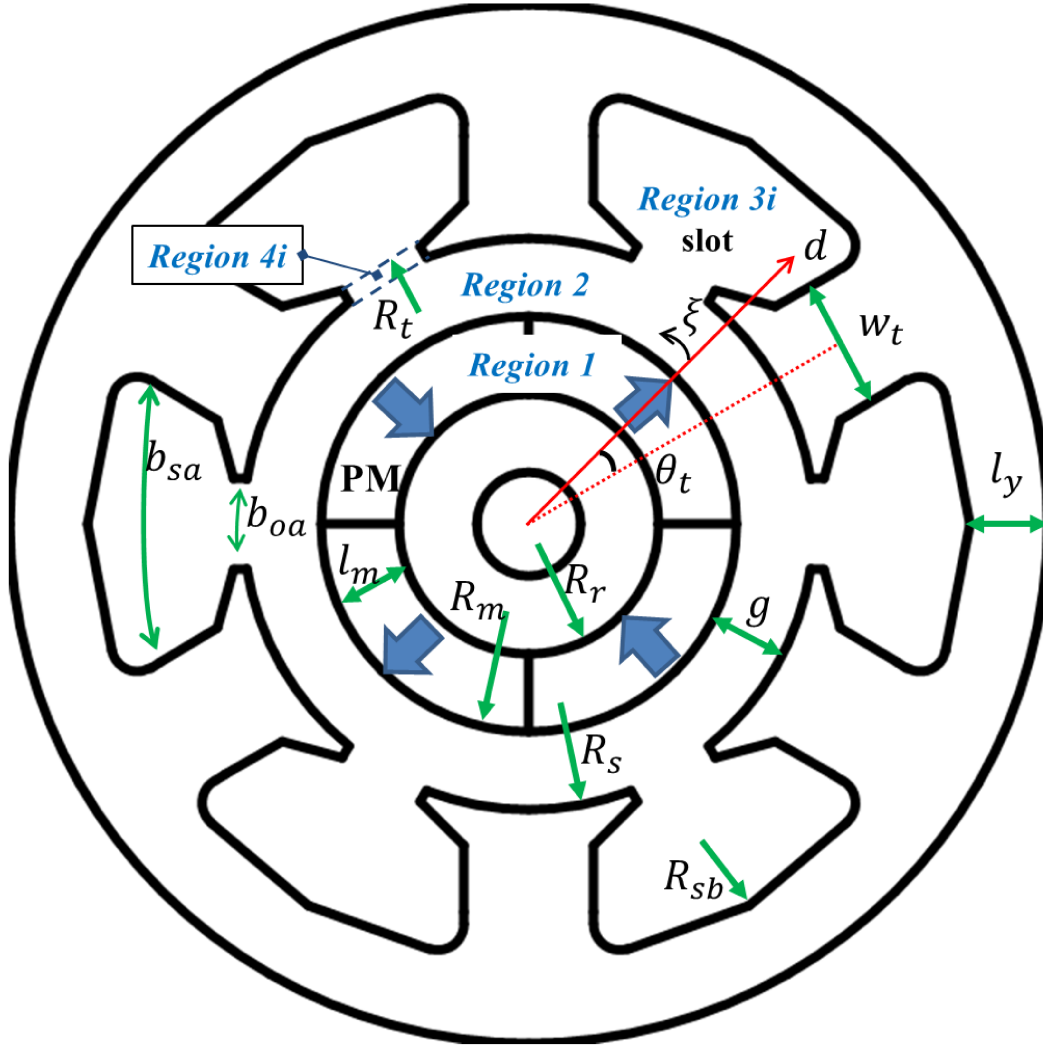


Fig. 4.29 Analytical subdomain model view

The PM, airgap, slot openings, and slots regions are defined as region 1, 2, 3i and 4i,  $i = 1, 2, 3 \dots Q$  is the sequence of the slot number  $Q$ , Then vector potential in each subdomain  $A_{z1}$ ,  $A_{z2}$ ,  $A_{z3}$ , and  $A_{z4}$  are given by,

$$\frac{\partial^2 A_{z1}}{\partial r r^2} + \frac{1}{r r} \frac{\partial A_{z1}}{\partial r} + \frac{1}{r r^2} \frac{\partial^2 A_{z1}}{\partial \xi^2} = -\frac{\mu_0}{r r} \left( M_{\xi} - \frac{\partial M_r}{\partial \xi} \right) \quad (4.35)$$

$$\frac{\partial^2 A_{z2}}{\partial r r^2} + \frac{1}{r r} \frac{\partial A_{z2}}{\partial r} + \frac{1}{r r^2} \frac{\partial^2 A_{z2}}{\partial \xi^2} = 0 \quad (4.36)$$

$$\frac{\partial^2 A_{z3}}{\partial r r^2} + \frac{1}{r r} \frac{\partial A_{z3}}{\partial r} + \frac{1}{r r^2} \frac{\partial^2 A_{z3}}{\partial \xi^2} = 0 \quad (4.37)$$

$$\frac{\partial^2 A_{z4}}{\partial r r^2} + \frac{1}{r r} \frac{\partial A_{z4}}{\partial r} + \frac{1}{r r^2} \frac{\partial^2 A_{z4}}{\partial \xi^2} = -\mu_0 J_i \quad (4.38)$$

Where  $J_i$  is the current density of the  $i$ th slot,  $M_\xi$  and  $M_r$  are the tangential and radial components of the PM magnetization,  $r r$  and  $\xi$  are radial and circumferential position of the rotor. The expressions on  $M_\xi$  and  $M_r$  are given in [140]. Through the periodic boundary of the machine, the general solution to vector potentials in each subdomain is governed as,

$$A_{z1} = \sum_k \left[ A_1 \left( \frac{r r}{R_m} \right)^k + B_1 \left( \frac{r}{R_r} \right)^{-k} \right] \cos(k\xi) + \sum_k \left[ C_1 \left( \frac{r r}{R_m} \right)^k + D_1 \left( \frac{r}{R_r} \right)^{-k} \right] \sin(k\xi) + A_{1p} \quad (4.39)$$

$$A_{z2} = \sum_k \left[ A_2 \left( \frac{r}{R_s} \right)^k + B_2 \left( \frac{r r}{R_m} \right)^{-k} \right] \cos(k\xi) + \sum_k \left[ C_2 \left( \frac{r r}{R_s} \right)^k + D_2 \left( \frac{r}{R_m} \right)^{-k} \right] \sin(k\xi) \quad (4.40)$$

$$A_{z3i} = \sum_n D_{3i} \left[ G_3 \left( \frac{r r}{R_{sb}} \right)^{E_n} + \left( \frac{r r}{R_t} \right)^{-E_n} \right] \cos \left( E_n \left( \xi - \frac{b_{sa}}{2} - \xi_i \right) \right) + A_{3p} \quad (4.41)$$

$$A_{z4i} = \sum_m \left[ C_{4i} \left( \frac{r r}{R_t} \right)^{F_m} + D_{4i} \left( \frac{r r}{R_s} \right)^{-F_m} \right] \cos \left( F_m \left( \xi - \frac{b_{oa}}{2} - \xi_i \right) \right) + A_{4p} \quad (4.42)$$

Here  $R_s$ ,  $R_m$ ,  $R_{sb}$  and  $R_t$  are stator inner, rotor outer slot bottom and slot opening radii,  $A_{1p}$ ,  $A_{3p}$  and  $A_{4p}$  are the particular solutions of the vector potential expressions.  $A_1$ - $D_1$ ,  $A_2$ - $D_2$ ,  $D_{3i}$ ,  $C_{4i}$  and  $D_{4i}$  are the coefficients to be decided by

the continuous boundary conditions on each interface between adjacent subdomains [140].  $k$ ,  $n$  and  $m$  are the harmonic orders.  $b_{sa}$  and  $b_{oa}$  are slot and slot opening angles, respectively.  $E_n$ ,  $F_m$  and  $G_3$  relate to  $b_{sa}$  and  $b_{oa}$  and calculated as,

$$E_n = n\pi/b_{sa} \quad (4.43)$$

$$F_m = m\pi/b_{oa} \quad (4.44)$$

$$G_3 = (R_t/R_{sb})^{E_n} \quad (4.45)$$

By applying the continuous flux density and magnetic field intensity boundary conditions between PM and airgap subdomains, continuous flux density and vector potential boundary conditions among airgap,  $i$ th slot opening and  $i$ th slot subdomains, the magnetic field potential can be solved [140]. The radial and tangential components of  $B_g$  are given as,

$$B_{gr} = \frac{1}{r} \frac{\partial A_{z2}}{\partial \xi} = \sum_k B_{rsk} \sin(k\xi) + \sum_k B_{rck} \cos(k\xi) \quad (4.46)$$

$$B_{gt} = -\frac{\partial A_{z2}}{\partial r} = \sum_k B_{\xi sk} \sin(k\xi) + \sum_k B_{\xi ck} \cos(k\xi) \quad (4.47)$$

Then the magnitude of airgap flux density is calculated as,

$$B_{gm0} = \sqrt{B_{gr}^2 + B_{gt}^2} \quad (4.48)$$

Where  $B_{rsk}$ ,  $B_{rck}$ ,  $B_{\xi sk}$  and  $B_{\xi ck}$  are coefficients and presented as.

$$B_{rsk} = -\frac{k}{r} \left[ A_2 \left( \frac{r}{R_s} \right)^k + B_2 \left( \frac{r}{R_m} \right)^{-k} \right] \quad (4.49)$$

$$B_{rck} = \frac{k}{r} \left[ C_2 \left( \frac{r}{R_s} \right)^k + D_2 \left( \frac{r}{R_m} \right)^{-k} \right] \quad (4.50)$$



$$B_{\xi ck} = -\frac{k}{r} \left[ A_2 \left( \frac{r}{R_s} \right)^k - B_2 \left( \frac{r}{R_m} \right)^{-k} \right] \quad (4.51)$$

$$B_{\xi sk} = -\frac{k}{r} \left[ C_2 \left( \frac{r}{R_s} \right)^k - D_2 \left( \frac{r}{R_m} \right)^{-k} \right] \quad (4.52)$$

Then  $B_{gr}$  and  $B_{gt}$  waveforms over one pole for a DW-SPM motor ( $p = 2, q = 2, l_m = 5 \text{ mm}, g = 1 \text{ mm}$ ) are shown in Fig. 4.30 (black curves).

Since the slot effect is already taken into account in the subdomain model for one given magnet length  $l_{m0}$ , then the airgap flux density expression relating to other magnet lengths can be obtained from the given  $B_{gt0}$  and  $B_{gr0}$  by applying (4.33),

$$B_{gr1} = \frac{l_{m1}(l_{m0} + gu_r)}{l_{m0}(l_{m1} + gu_r)} \cdot B_{gr0} \quad (4.53)$$

$$B_{gt1} = \frac{l_{m1}(l_{m0} + gu_r)}{l_{m0}(l_{m1} + gu_r)} \cdot B_{gt0} \quad (4.54)$$

Where  $B_{gr0}$  and  $B_{gt0}$  is the radial and tangential flux density distribution referring to  $l_{m0}$ .  $l_{m1} = 6 \text{ mm}$  is the magnet length to be considered. The waveforms comparisons on  $B_{gr1}$  and  $B_{gt1}$  between calculated ones (4.53), (4.54), and FEA results are shown in Fig. 4.30.

It can be seen that the calculated  $B_{gr1}$  and  $B_{gt1}$  have a good agreement with FEA results over the entire pole pitch. Therefore, the other  $B_{gr}$  and  $B_{gt}$  referring to all  $l_m/g$  domain can be achieved by combining only one subdomain solution results ( $B_{gr0}$  and  $B_{gt0}$ ) and (4.53)- (4.54).

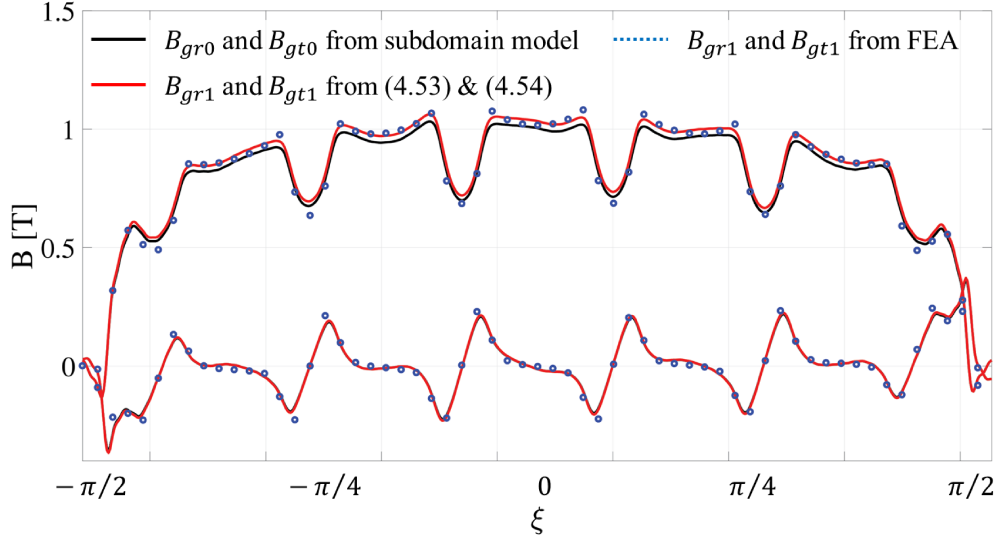


Fig. 4.30  $B_{gr1}$  and  $B_{gt1}$  comparisons between analytical and FEA results over one pole pitch

#### 4.3.2.3 Stator Sizing

In previous work [128], the airgap flux density  $B_g$  is calculated by (4.34), which means the average  $B_g$  rather than the maximum one over one pole is used to define the tooth width  $w_t$  and yoke length  $l_y$ . In return, both sizes are larger than needed. In other word, the steel is not fully loaded as desired ( $B_{fe}$ ) at no load condition. Moreover, larger steel decreases the slot areas  $A_s$ , i.e. reduces nominal rated current  $i_0$  level.

According to the analysis above, the flux density distribution over one slot pitch can be got for entire  $l_m/g$  domain. This also means the most loaded tooth over one pole pitch can be used to define  $w_t$  in a more accurate way. Therefore, one particular rotor position  $\theta_t$  is chosen in the subdomain model. At  $\theta_t$  position, d axis is aligned with the tooth center (4.29).

Since the relative span between PM and tooth width is the key factor to calculate the total flux enters into the tooth, the situations also divide into several main parts.

1) *DW-SPM*: One PM pitch  $\tau_{PM}$  contains more than two slots pitch  $\tau_s$  for the DW-SPM motors. In this case, the tooth width  $w_t$  relates to the average flux density passing into the most loaded slot pitch  $B_{\tau_s-avg}$ . Then  $w_t$  can be given as,

$$w_t = \frac{B_{\tau_s-avg}}{B_t} \cdot \tau_s \quad (4.55)$$

Where  $B_t$  is the desired steel loading for the tooth. In terms of yoke sizing, it is assumed that all the flux produced by PMs entering into stator yoke, then  $l_y$  is,

$$l_y = \frac{B_{PM-avg}}{B_y} \cdot \frac{\tau_{PM}}{2} \quad (4.56)$$

Here  $B_{PM-avg}$  is the average flux density produced by PMs, and  $B_y$  is the needed yoke loading. For both  $B_{\tau_s-avg}$  and  $B_{PM-avg}$ , they are the mean magnitudes coming from the superposition of each radial and tangential components. The corresponding geometry definition is given in Fig. 4.31. The relevant flux densities distribution is reported in Fig. 4.32.

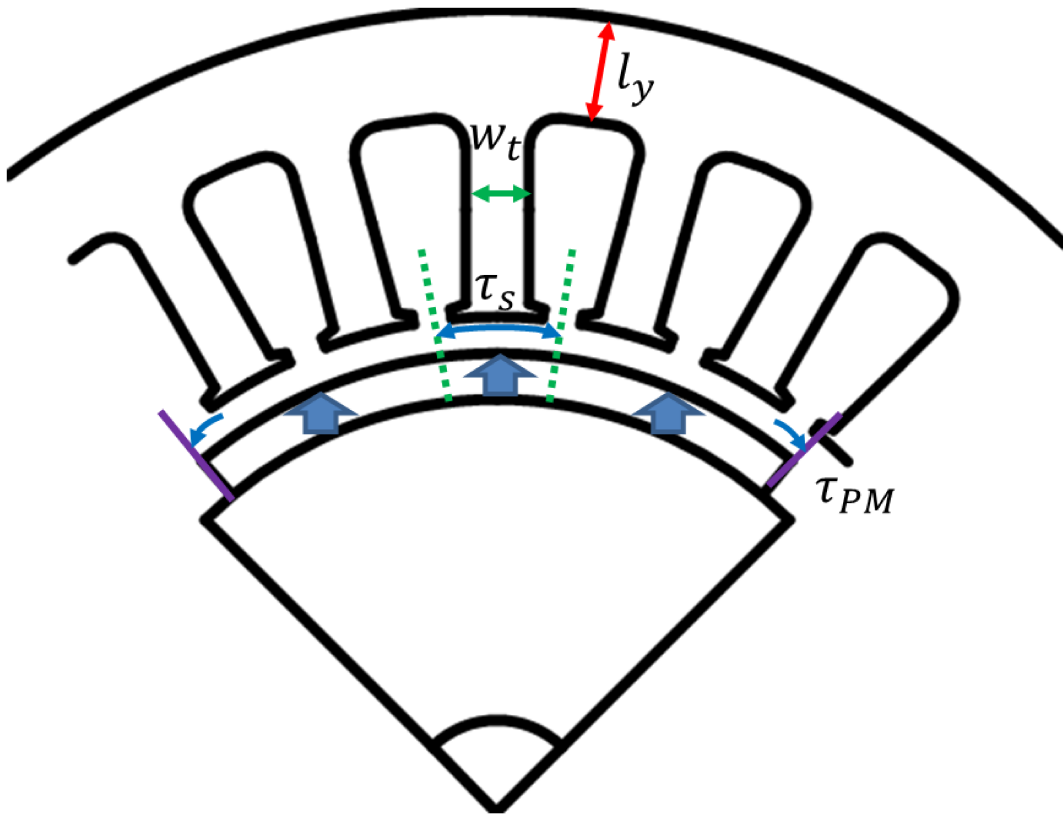
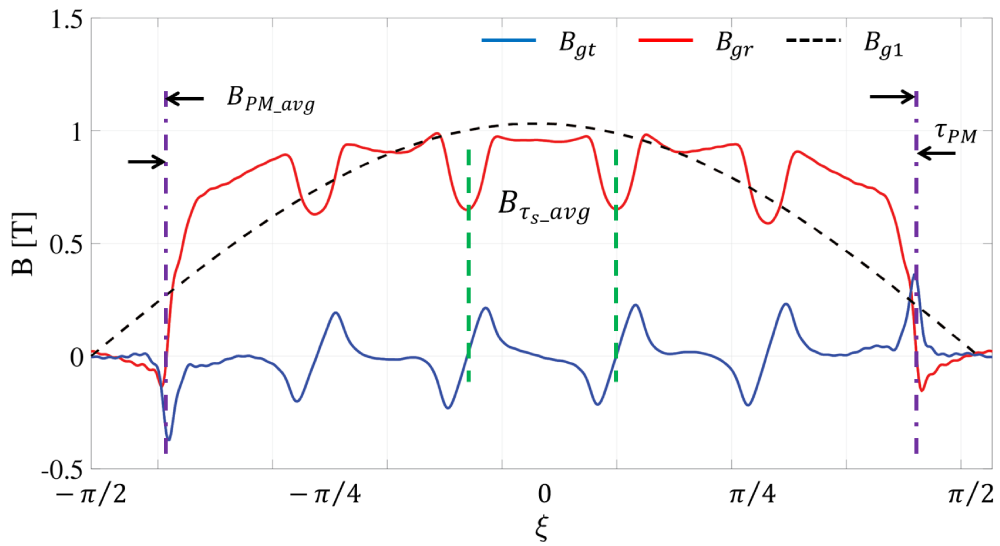


Fig. 4.31 Stator geometry definition for DW-SPM motors

Fig. 4.32  $B_g$  waveforms for DW-SPM motors

2): *CW-SPM, PM pitch less than slot pitch*: the relevant geometry is shown in Fig. 4.33. In this situation, all the flux produced from one PM pole enters into one tooth. Therefore, the area that the airgap flux faces at stator shoe is the entire PM pitch  $\tau_{PM}$ , then  $w_t$  is obtain as,

$$w_t = \frac{B_{PM\_avg}}{B_t} \tau_{PM} \quad (4.57)$$

For most of the CW-SPM motors, the flux separates evenly at stator yoke for both directions. Consequently,

$$l_y = w_t/2 \quad (4.58)$$

The detailed geometry and airgap flux density waveform of this kind of motor is presented in Fig.4.33 and Fig.4.34.

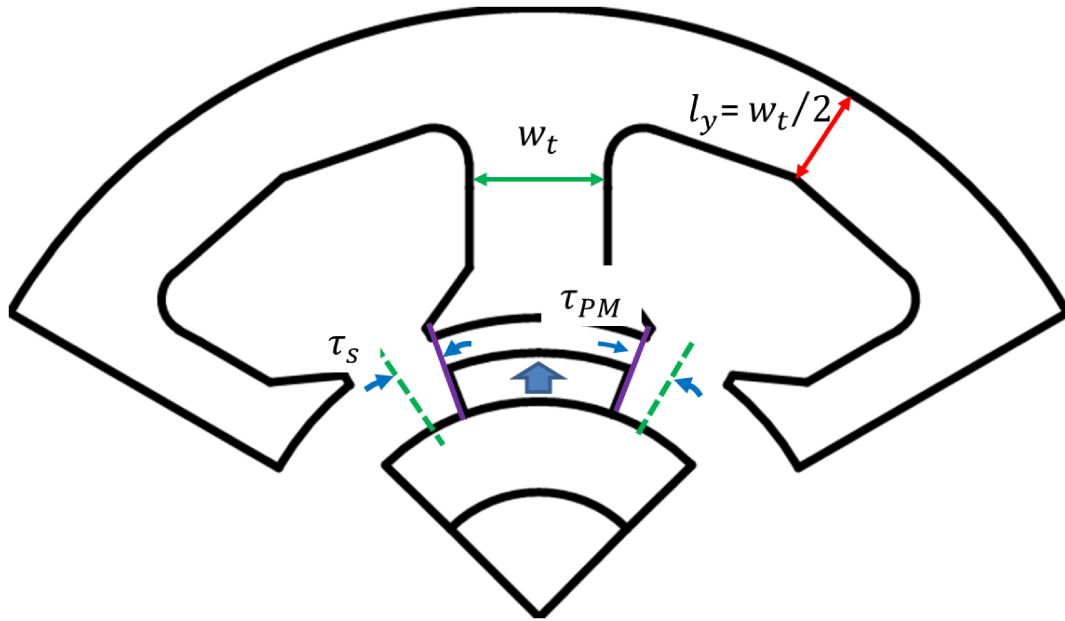


Fig. 4.33 Stator geometry definition for CW-SPM motors when  $\tau_{PM} < \tau_s$

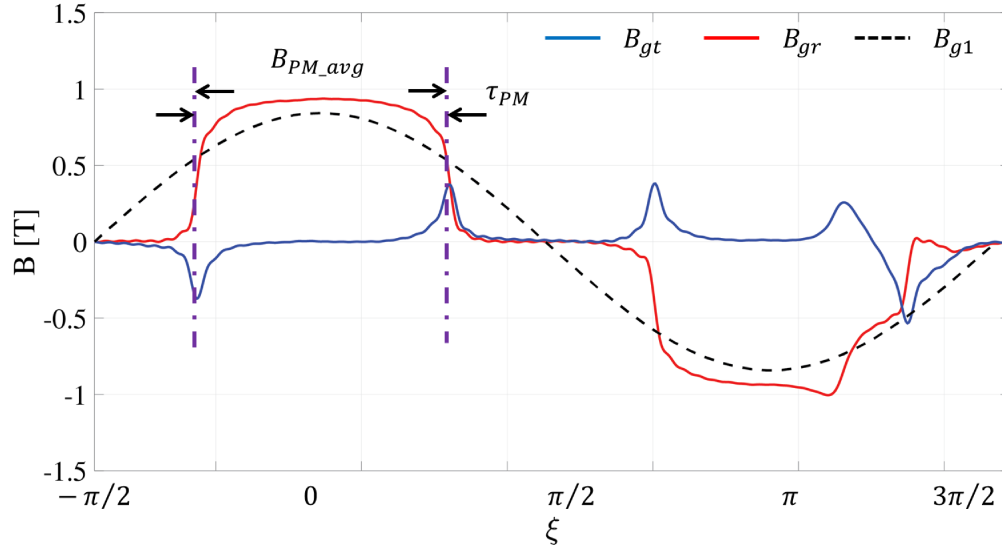


Fig. 4.34  $B_g$  waveforms for CW-SPM motors when  $\tau_{PM} < \tau_s$

3): *CW-SPM, PM pitch less than slot pitch with small PM interval*: different from the situation above, PM interaction occurs between adjacent poles when the two poles are approaching (mainly in motors with more than 10 poles,  $p > 5$ ). Not all the flux produced by one pole goes into the stator because self-circulating happens at the edge the PMs. The geometry is reported in Fig. 4.35. In this case, the airgap flux directly faces at stator tooth shoe is the effective portion. The active PM pitch  $\tau_{PM\_act}$  is the span of one tooth shoe. In this case,  $w_t$  is obtained as,

$$w_t = \frac{B_{PM\_act}}{B_t} \tau_{PM\_act} \quad (4.59)$$

Here  $B_{PM\_act}$  is the average flux density of active PM area and calculated by,

$$\tau_{PM\_act} = (1 - k_{so}) \tau_s \quad (4.60)$$

Here  $k_{so}$  is the slot open ratio in p.u. In terms of  $l_y$ , it can be achieved by (4.58). The related geometry and flux density waveforms are shown in Fig. 4.35 and 4.36.

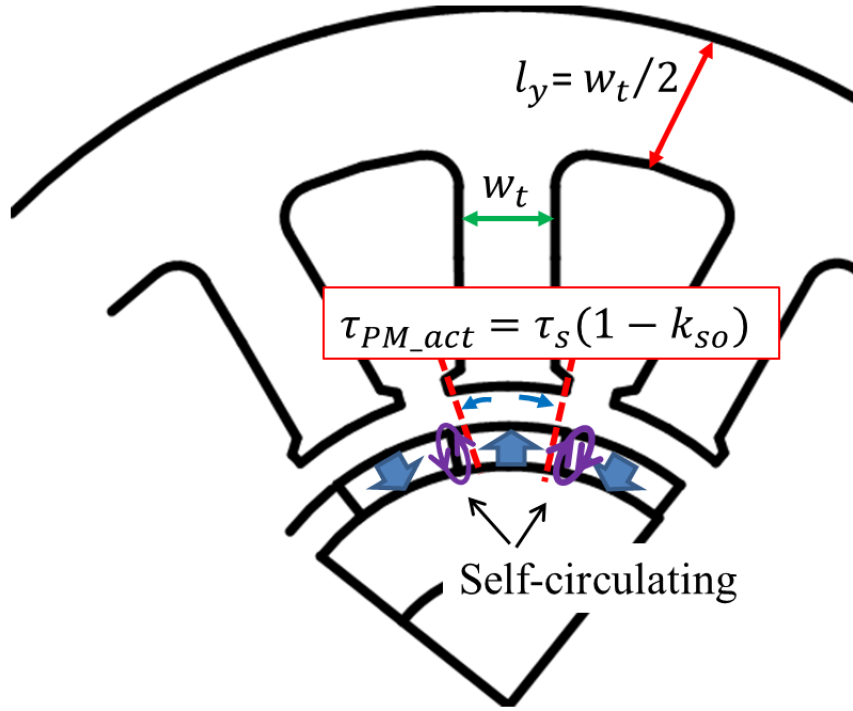


Fig. 4.35 Stator geometry definition for CW-SPM motors when  $\tau_{PM} < \tau_s$  with small PM intervals

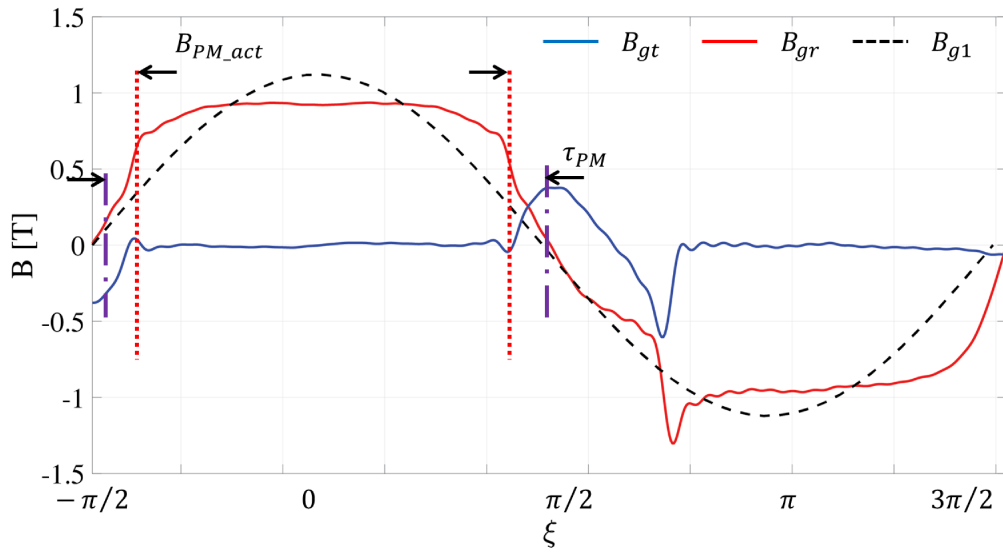


Fig. 4.36  $B_g$  waveforms for CW-SPM motors when  $\tau_{PM} < \tau_s$  with small PM intervals

4) *CW-SPM, PM pitch larger than one slot pitch*: this condition majors in the motors with both small quantity of poles ( $p < 10$ ). Like DW-SPM motor case, just the flux generated near PM center is passing into the tooth. However, differed from DW-SPM case, slot center is not the boundary for the flux going into the most loaded tooth. Due to the high slot leakage, the active PM span is smaller than  $\tau_s$ . Then (4.59) and (4.58) are used to get  $w_t$  and  $l_y$ , respectively. Unlike the case above,  $\tau_{PM\_act}$  is calculated by  $B_{gt} = 0$  points next to the slot center rather than the entire tooth shoe span. The geometry and  $B_g$  waveforms are shown in Fig. 4.37 and 4.38.

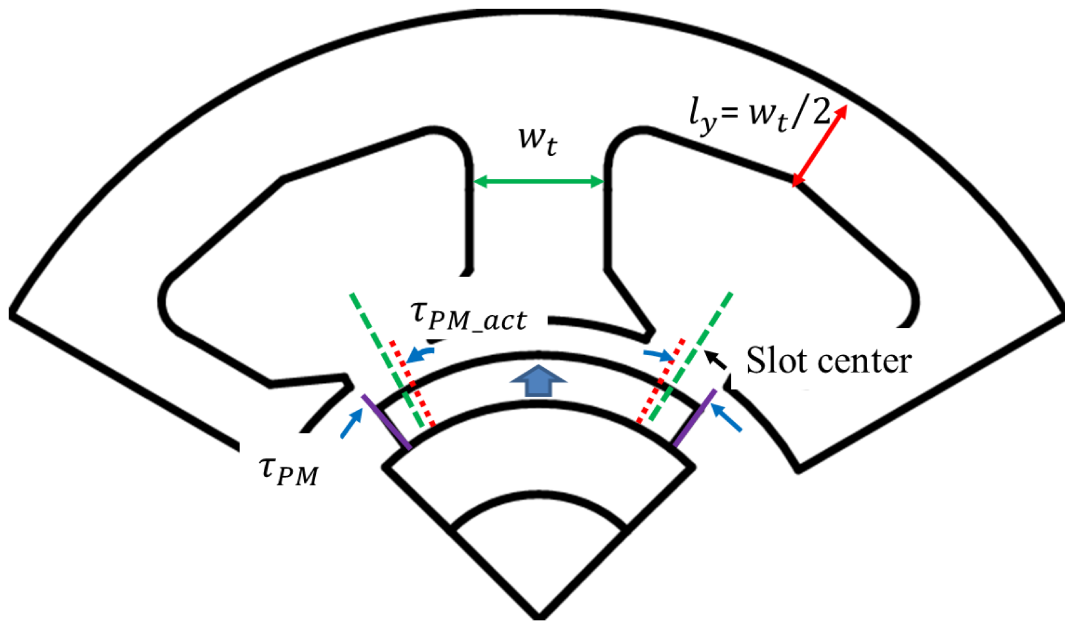


Fig. 4.37 Stator geometry definition for CW-SPM motors when  $\tau_{PM} > \tau_s$

5) *CW-SPM, PM pitch larger than two slot pitches*: motors with large quantity of slots ( $q = 4/5, 4/7, \dots$ ) can be grouped in this case. Similar with DW-SPM motors,  $w_t$  can be controlled by (4.55). The related  $B_g$  waveform to calculate  $w_t$  is similar as Fig. 4.32.



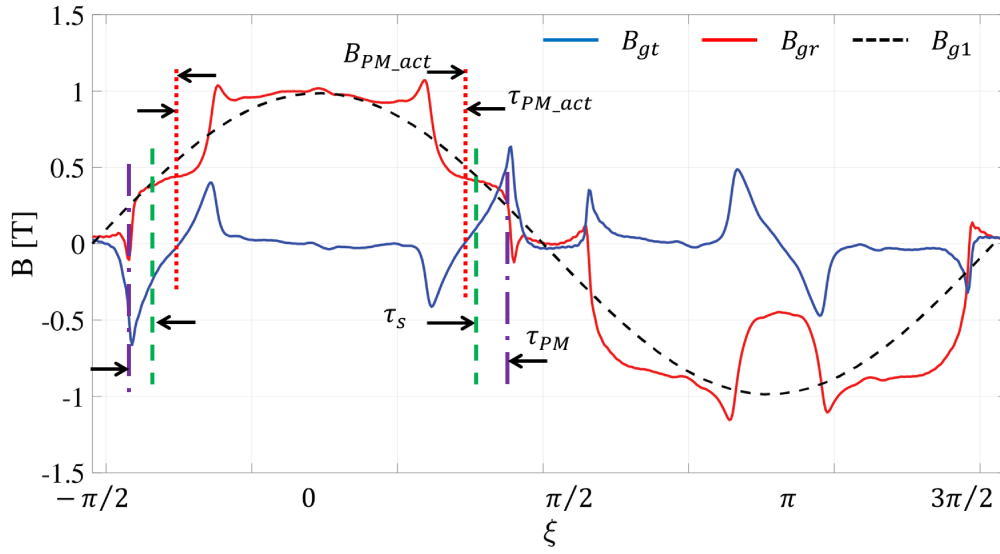


Fig. 4.38  $B_g$  waveforms for CW-SPM motors when  $\tau_{PM} > \tau_s$

In terms of  $l_y$ , not only the central part contributes to the total flux passing into the yoke, but also the lateral portion is included. Nonetheless, the whole flux from one PM pole separates equivalently at the yoke. The relevant geometry and  $B_g$  waveforms are shown in Fig. 4.39 and Fig. 4.40. Hence,  $l_y$  is obtained from (4.56),

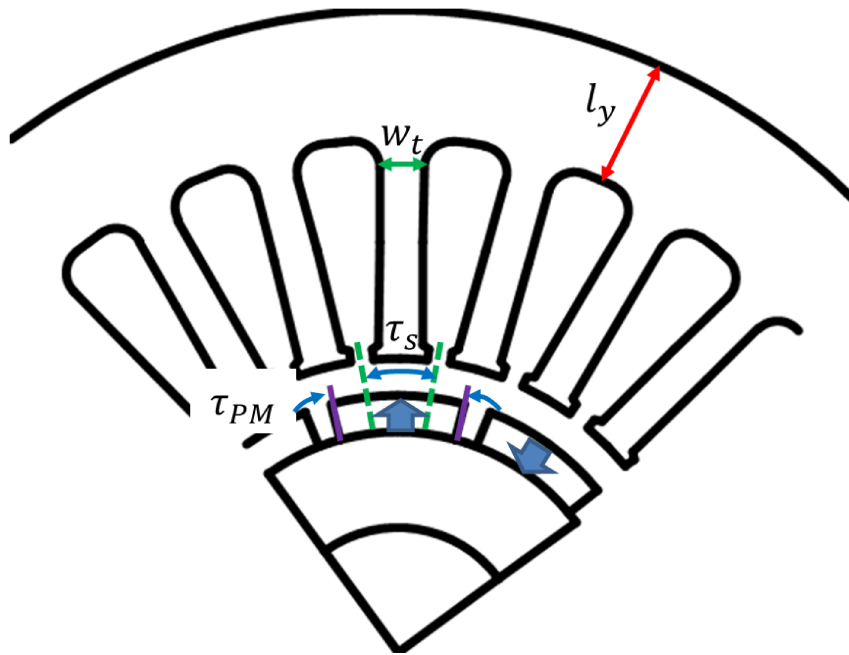


Fig. 4.39 Stator geometry definition for CW-SPM motors when  $\tau_{PM} > 2\tau_s$

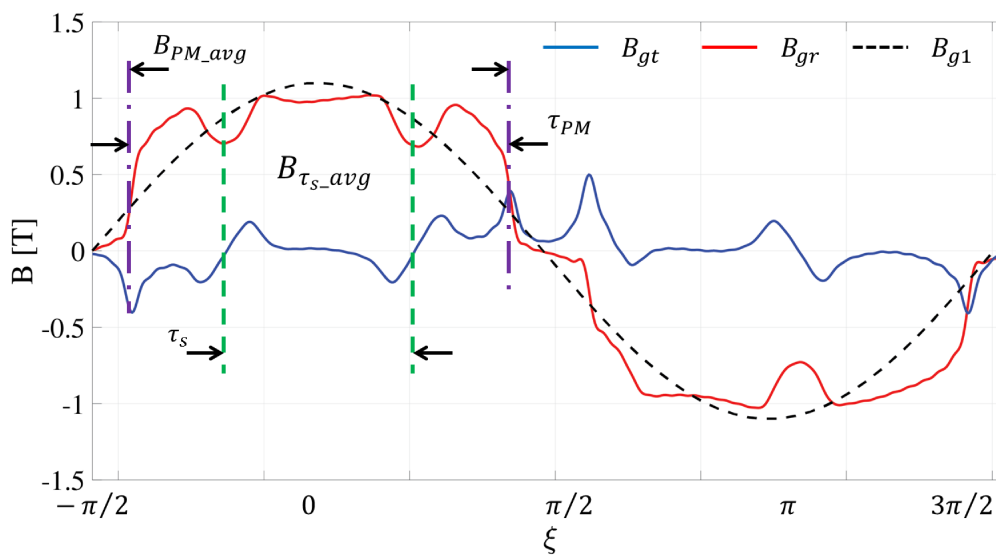


Fig. 4.40  $B_g$  waveforms for CW-SPM motors when  $\tau_{PM} > 2\tau_s$

#### 4.3.2.4 Design Input

The pole-slot combination should be defined first, other the initial design inputs are:

- Stack dimensions  $D$ ,  $L$  and airgap length  $g$ .
- PM remanence  $B_r$  and peak flux density in steel  $B_{fe}$ .
- Thermal loading  $k_j$ .
- PM span angle  $\alpha_m$  and  $k_{so}$ .

In this study, both tooth loading and stator yoke loading are equal to  $B_{fe}$ , i.e.  $B_t = B_y = B_{fe}$ . The number of turns per phase  $N_s$  is set to an initial value and adjusted in the final stages of the design according to the specified voltage and speed ratings.

The definitions of  $k_j$ , torque and PF expressions are kept as same as the ones in last section.

From the analysis in Section II.B, the airgap flux density distribution  $B_g$  directly refers to the magnet on airgap ratio  $l_m/g$ . Therefore,  $x$  and  $l_m/g$  together determine the PM flux linkage  $\lambda_m$ , shown in (4.28).

Then  $B_{g1}$  is re-calculated as the peak of fundamental content of radial component  $B_{gr}$ , reported in Fig. 4.32, 4.34, 4.35, 4.38 and 4.39. For the entire  $l_m/g$  domain,  $B_{g1}$  can be achieved by the Fourier transform of each  $B_{gr}$  distribution over one pole pair, according to (4.46) and (4.53).

#### 4.3.2.5 Design Flowchart

After one point is picked from the plane, one motor model will be automatically built, on the basis of the sizing equations described above. FEA validation follows, to verify whether the motor is in line with the specified performance. The detailed design flowchart is reported in Fig. 4.41.

After FEA validation at rated current condition, if the torque result is not adequate for the target, stack size or thermal loading can be improved to increase the torque generation. Then the process is repeated.

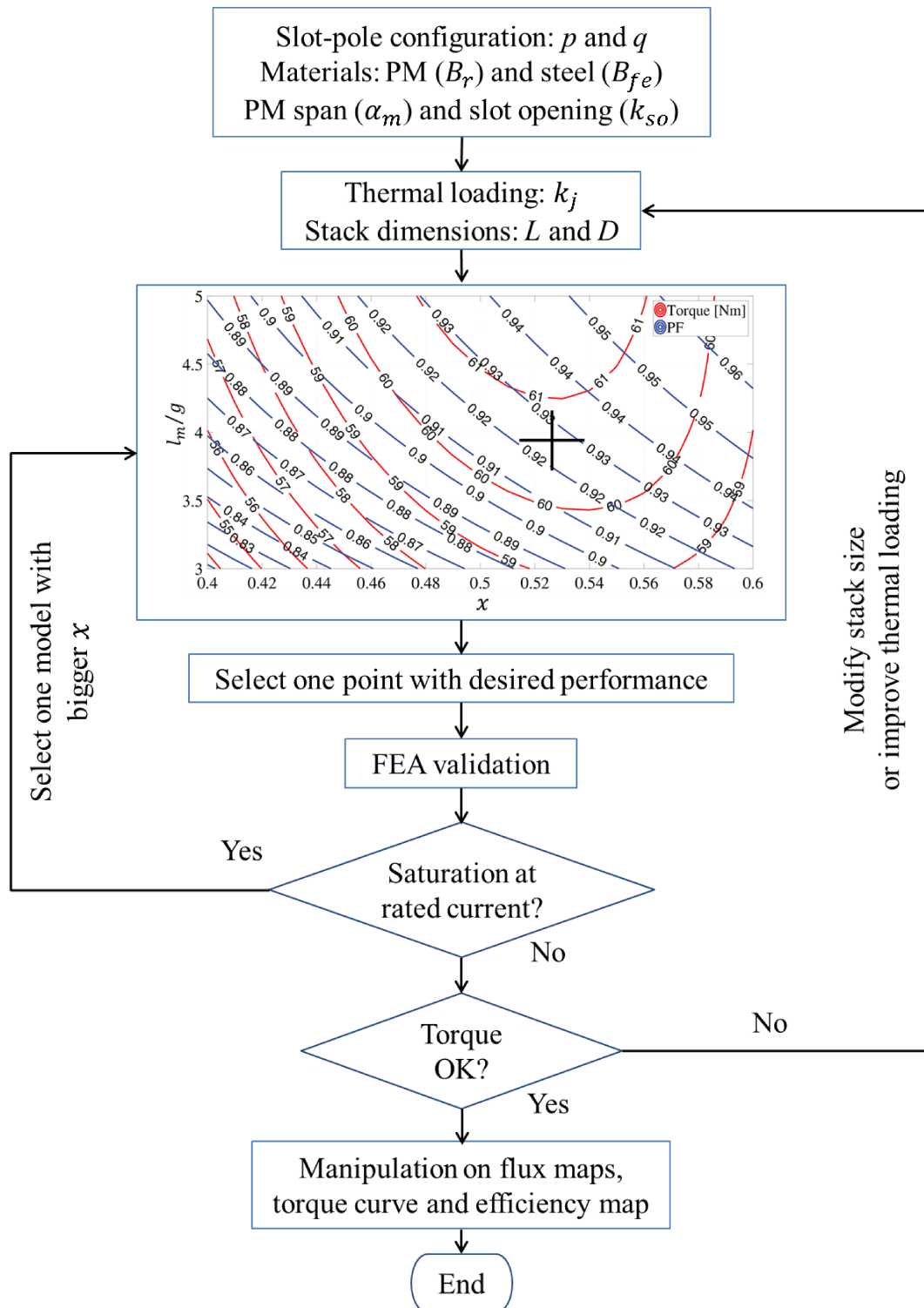


Fig. 4.41 Flowchart of parametric design procedure

### 4.3.3 Design Examples and Results

In this research, both DW and CW machines with different slot-pole combinations are validated by FEA. Results on steel loading, PM flux linkage, torque and PF of all the models are obtained from FEA and compared with analytical models. Both  $B_{gr}$  and  $B_{gt}$  are calculated along the central circumference of airgap. The distinction flux densities between the middle of airgap and tooth shoe faces are neglected. The instruction on selecting model on the parametric plane is illustrated in detail. The relationships among efficiency, torque capability and steel loading are studied. The common specifications are given in Table 4.6.

Table 4.6 Common ratings of motor models

Parameters	Units	DW	CW
Stator outer diameter ( $D$ )	mm	175	
Length ( $L$ )	mm	110	
Copper loss	W	550	
Thermal loading ( $k_j$ )	kW/m <sup>2</sup>	9.1	
Airgap length ( $g$ )	mm	1	
Steel grade ( $g$ )		M250-35A	
Steel loading ( $B_{fe}$ )	T (pk) mm	1.4	
PM grade		NdFeB 32 MGOe	
PM remanence ( $B_r$ )	T	1.16	
Number of turns per phase ( $N_s$ )		120	40
Copper filling factor		0.432	0.55

Three DW-SPM machines are tested (case 1), and other seven CW-SPM machines divided into four cases that corresponds to Section 4.3.2.3. The pole-slot number, PM span, and slot opening ratio are reported in the table for each model.  $D$ ,  $L$  and  $k_j$  are set as invariant for the all models, shown in Table 4.6.

#### 4.3.3.1 Steel Loading

In the study, the desired  $B_{fe}$  is chosen as 1.4 T for all the models. The steel is ‘M250-35A’, whose knee point towards nonlinear portion is around 1.4 T. A simplified linear steel model is used in subdomain model analysis, therefore higher  $B_{fe}$  will make the sizing imprecise.

$B_t$  and  $B_y$  are the maximum measured flux densities on the tooth and yoke at  $\theta_t$  position, respectively. From the FEA results of all the models, the errors of both  $B_t$  and  $B_y$  are controlled less than 3.5 %. It proves that the sizing equations on  $w_t$  and  $l_y$  are suitable for all DW and CW models at open load conditions.

#### 4.3.3.2 Torque and PF Results

At no load condition,  $\lambda_m$  is calculated by (4.28), which has a good agreement with FEA results for all the models, shown in Table 4.7. The nominal rated current  $i_0$  is obtained via (4.14) and used as the input current of FEA simulations. For DW-SPM motors, both torque and PF from FEA results are matched with analytical ones.

In terms of CW-SPM motors, the results on torque and PF from the parametric planes are in accordance with FEA output when the pole number is small, e.g. case 4 ( $p = 2, q = 0.5$ ). Conversely, when  $p$  increases, FEA results on torque become less than the analytical ones (Case 2a, 4, and 5). Cross-saturation occurs and decreases the torque level at  $x = 0.5$  condition, since the electric loading  $A_s$  is considerable and the core is saturated when the motors are fed with  $i_0$ . Severe saturation drags down the machine efficiency and also heats up the machine soon, which should be avoided in the design. In the parametric design process, higher  $x$  selection is recommended when the machine has multi poles. The parametric procedures of Case 2 and 3 are duplicated to design a better machine without saturation. The parametric plane of both cases are reported in Fig. 4.42 and Fig. 4.44, respectively. The relative four motor structures are presented in Fig. 4.43 and Fig. 4.45.

Table 4.7 Comparison between parametric method and FEA results

$l_m/g = 5$	Case	$p$	$q$	$\alpha_m$	$k_{so}$	T [Nm]		PF		$\lambda_m[V s]$		$i_0$ [A]	$B_t$ [T]	$B_y$ [T]
						Plane	FEA	Plane	FEA	Calculated	FEA			
$x = 0.5$	1	2	2	160	0.3	47	46	0.94	0.94	0.596	0.594	26	1.39	1.41
	1	2	3	160	0.3	49	48	0.94	0.95	0.61	0.609	27	1.42	1.39
	1	3	2	160	0.3	59	58	0.94	0.94	0.42	0.42	31	1.42	1.38
	2a	5	2/5	130	0.25	86	78	0.75	0.74	0.072	0.072	159	1.41	1.42
	3a	7	2/7	170	0.3	102	91	0.73	0.67	0.057	0.056	170	1.4	1.38
	4	2	0.5	150	0.3	53	53	0.88	0.88	0.16	0.16	109	1.41	1.41
	5	7	4/7	150	0.3	78	71	0.89	0.74	0.044	0.044	168	1.4	1.45
$x = 0.7$	2b	5	2/5	130	0.25	74	73	0.95	0.95	0.102	0.102	97	1.4	1.38
	3b	7	2/7	170	0.3	94	93	0.95	0.92	0.081	0.081	110	1.43	1.4

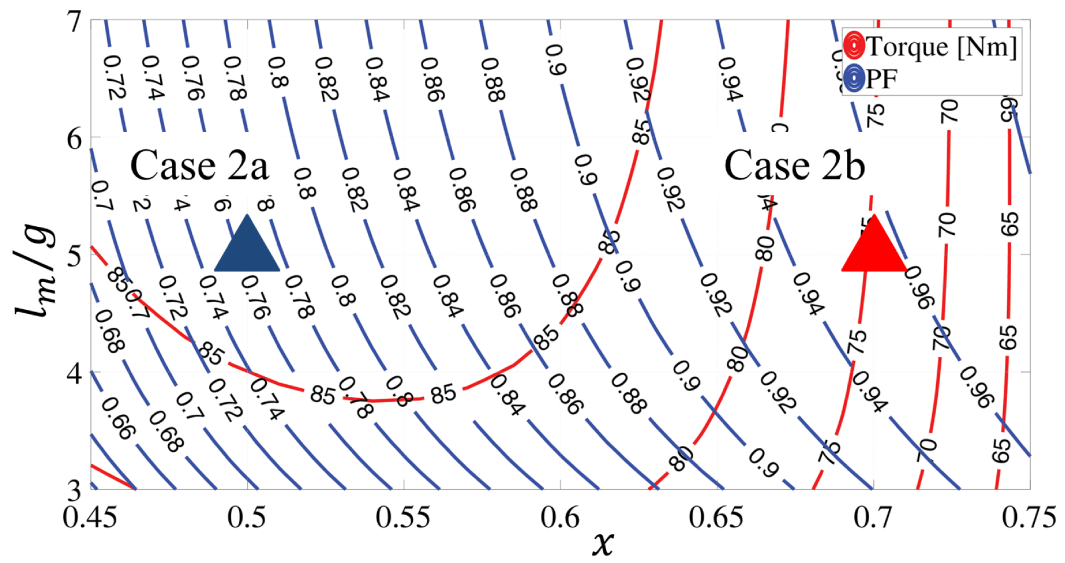


Fig. 4.42 Parametric plane of Case 2

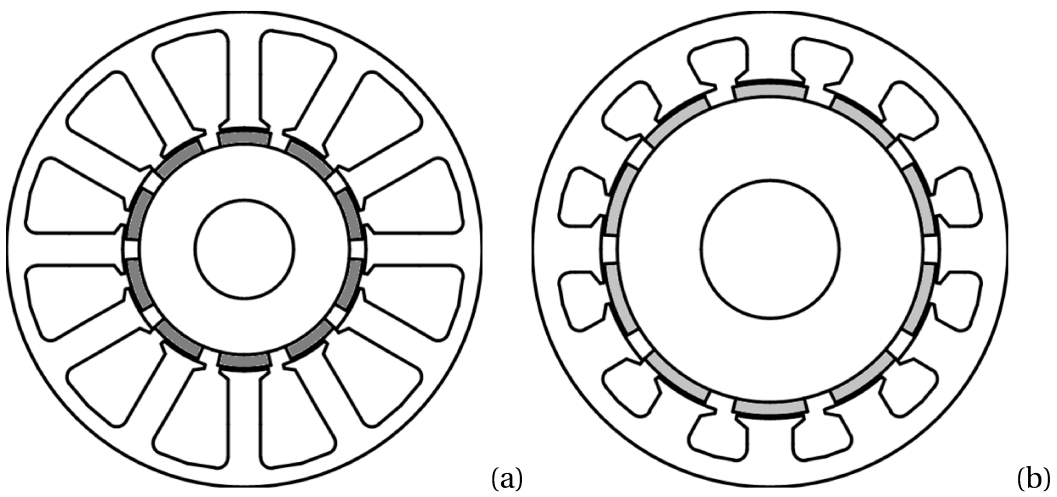


Fig. 4.43 Geometry Case 2



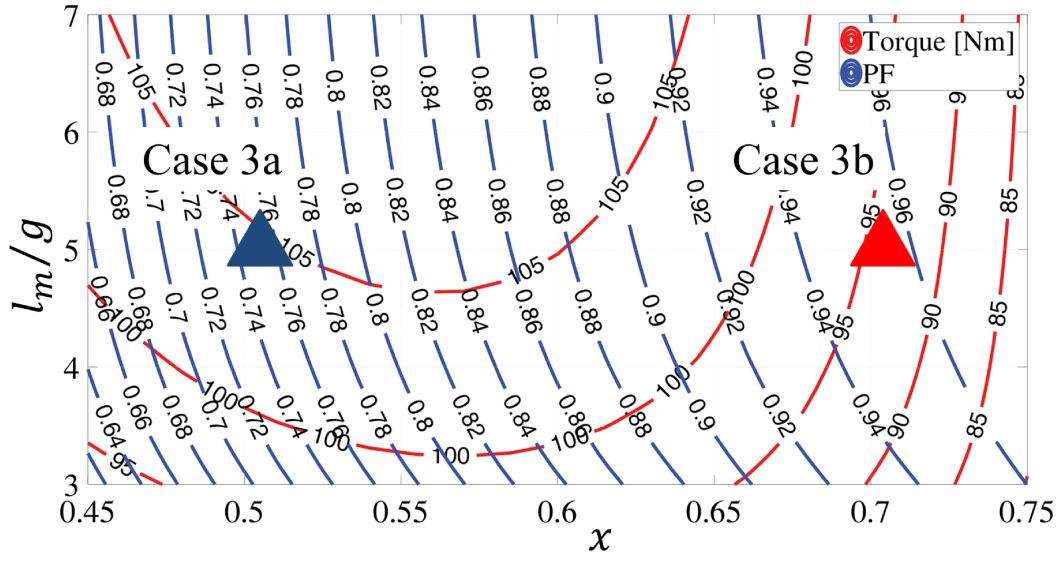


Fig. 4.44 Parametric plane of Case 3

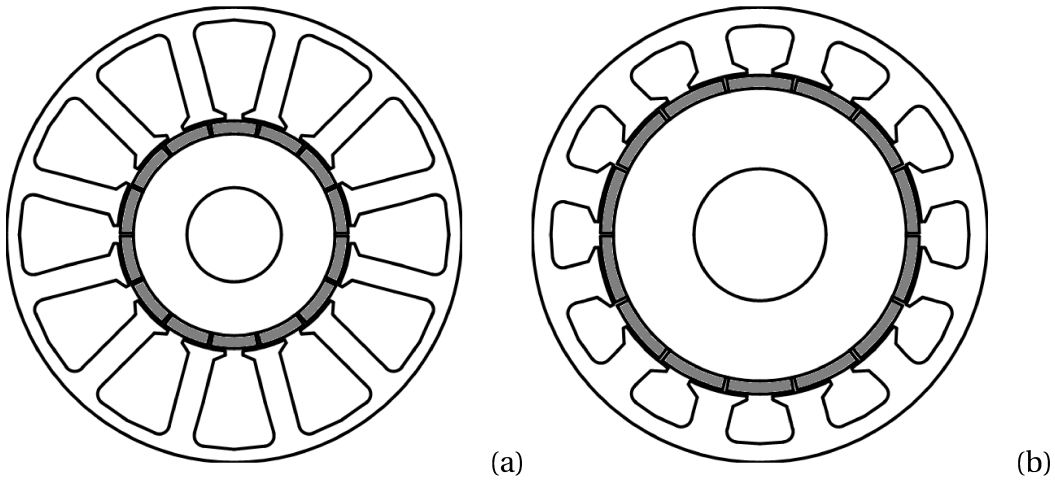


Fig. 4.45 Geometry Case 3

From the motor geometries, the slot area is significantly reduced when the rotor radius is increased from Case 2a to Case 2b. The forecast of PF is also improved (Fig.4.43a and 4.43b). Although the electric loading  $A_s$  is reduced,  $\lambda_m$  grows up according to (4.28). Therefore, the torque producing capability of Case 2b is still considerable compared with heavily saturated model 2a (73 vs 78 Nm). For Case 2b, saturation is totally avoided and the analytical and FEA results are agreed (Table 4.7). If the torque output is still reach the target, stack dimension or thermal loading  $k_j$  can be improved. Then the design procedure can be repeated.

The similar process can be duplicated in Case 3. By using larger rotor, the saturation effect disappears at rated current condition. The torque of case 3b is even higher than the saturated Case 3a, shown in Table 4.7.

#### 4.3.3.3 Efficiency

The efficiency comparisons at 1,000 rpm for both Case 2 and Case 3 are reported in Fig. 4.46 and Fig.4.47. The input currents for both Case 2a and 2b are 97 A (the nominal rated current for case 2b). Both torque and efficiency are improved from 2a to 2b. The same trend can be also found in the two models of Case 3 (Fig. 4.47). It turns out that besides increasing PF, bigger rotor also improves both torque and efficiency. Furthermore, less copper quantity is used due to the smaller slots.

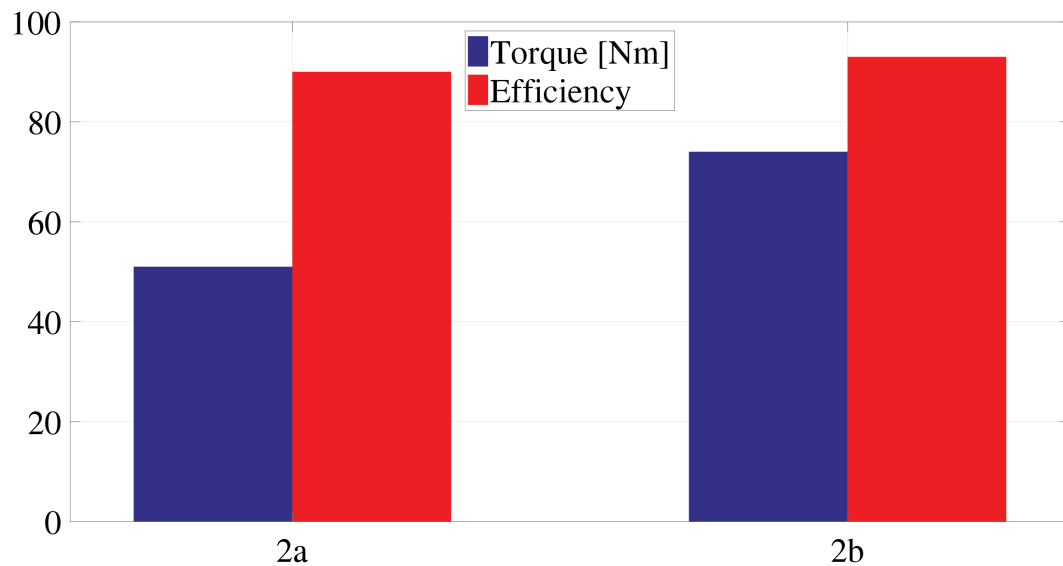


Fig. 4.46 Torque and efficiency comparison between Case 2a and 2b

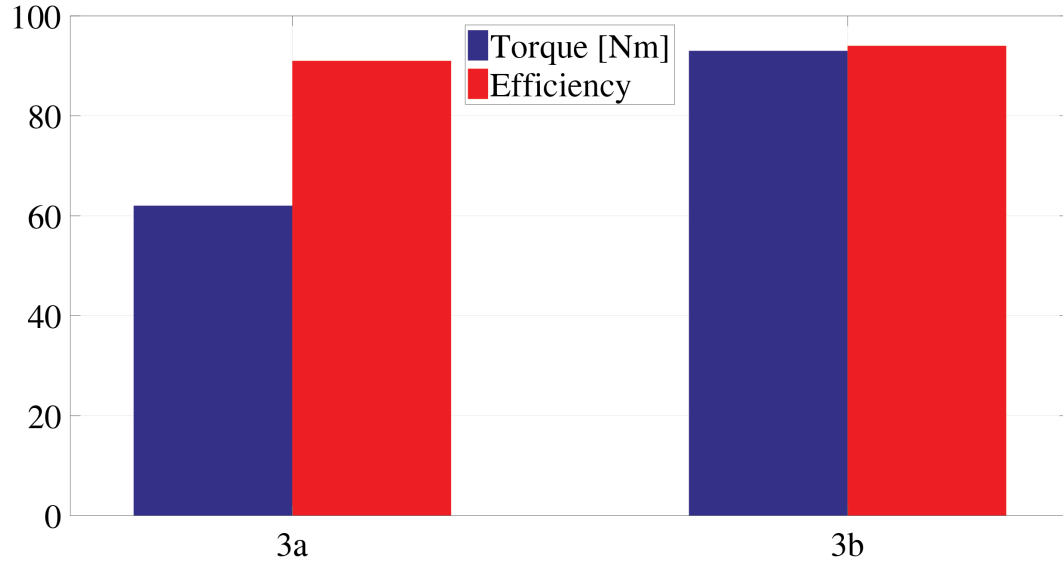


Fig. 4.47 Torque and efficiency comparison between Case 3a and 3b

#### 4.3.4 Design Summary

This study presents a parametric design method for both DW and CW SPM machines. A general design approach based on subdomain model is proposed. By using subdomain model, a Torque-PF parametric plane is established. The stator sizing equations are obtained by considering the most loaded flux pass in one slot pitch. Five different cases of SPM machines are analyzed to get the precise flux quantities passing through the most loaded teeth.

A comprehensive parametric design flowchart for SPM machines is addressed. By using the parametric method, motor models are built according to each sizing situation. The steel loadings on each tooth and yoke are measured and compared with target  $B_{fe}$  at open load condition, which show good agreements for all the cases.

Then the models are also tested at each nominal rated current. Two models are in highly saturated status. Then the design process is repeated to obtain motors with better efficiency and torque performance. The presented method gives an insightful and effective means in SPM machine design.

# Chapter 5

## Conclusion, and Future Work

### 5.1 Conclusion

This dissertation has presented two new design methods for SPM motors. Both design methods are comprehensively illustrated. Dealing with the automatic design using multi objective optimization method for the CW-SPM machines, the principle of using MODE algorithm to get Pareto front during the optimization process is introduced. Obtaining best trade-off machine among the optimization targets from the Pareto front is followed.

Two cases are reported by using automatic design method, each for CW-SPM and DW-SPM machine, respectively. In terms of CW-SPM machines for traction application, design equations, magnetic FEA, multi objective optimization, simplified structural and thermal co-design are presented. Besides providing comprehensive design procedures for CW-SPM machines for traction, the research suggests new design methodologies, such as the goal function  $\lambda_{(d,180^\circ)}$  that summarizes flux weakening capability in one FEA simulation. Torque and power profiles of designed machine are reported. The losses and efficiency map are also presented.

Considering a DW-SPM capable of low cogging torque, an automatic design procedure to optimize the PM shape of rounded SPM motors to find an optimal trade-off between torque and cogging torque behaviors is reported. Both torque and cogging torque calculation through magnet shaping method is analyzed. Dependent on demagnetization limit and optimal magnet span calculation, the

magnet bounds in optimization process are obtained. The cogging torque and maximum torque waveforms of three different motors on Pareto front are shown, which is obtained by MODE optimization and FEA simulations. One optimum motor is selected as the best trade-off machine among PM volume, torque and cogging torque behaviors.

The other design method called parametric design for SPM machines is reported. The parametric design provides a very effective and concise solution for the SPM machine design without losing precision. Three steps of parametric design development are reported. For each step, both design flowcharts and examples are shown.

At the initial stage, a  $(x, b)$  design plane is introduced, and a straightforward design approach for traction is presented. The design plane is to match torque requirement and the key design condition of power factor equal to  $1/\sqrt{2}$ . All designed machines have infinite speed flux weakening range. The illustrated design method for CW-SPM machines simplifies the design process, compared with general design procedures. The model used for the parametric design is FEA validated with success.

After that, a parametric design plane based on  $(x, l_m/g)$  for DW-SPM machines has been presented. The presented method applies to magnets of radial shape and also to rounded shape magnet, for cogging and torque ripple minimization. Based on that, the detailed design flowchart is illustrated. Two motor models for each uniform and nonuniform airgap length are selected as examples and validated by FEA simulation results, showing good agreement with estimated performance. One qualified rounded motor is built and tested, with rounded magnets. The experimental measurements on torque and PF performance of the rounded shape SPM motor prototype is presented. They match with FEA simulations and confirm the accuracy of the presented parametric method.

Eventually, a general design approach based on accurate steel loading for both DW and CW SPM machines is proposed. By using subdomain model, a Torque-PF parametric plane is established. The stator sizing equations are obtained by considering the most loaded flux pass in the stator teeth. Five different cases of SPM motors are analyzed to get the precise flux quantities passing through the most loaded teeth. A comprehensive parametric design flowchart for SPM machines is addressed. In each machine case, the steel loadings on tooth and yoke

are measured and compared with target  $B_{fe}$  at open load condition, which shows good agreements for all the machine cases. Then the models are also tested at each nominal rated current. Two models are in highly saturated status. Therefore the design process is repeated to obtain machines with better efficiency and torque performance. The presented method gives an insightful and effective means in the SPM motor design.

## 5.2 Future Work

The following suggestions can be done in the direction of this dissertation:

- Linear model of steel material is used in the parametric design method now, which is distorted when the steel loading  $B_{fe}$  is over 1.45 T. Applying also nonlinear portion of the material characteristic is a potential way to improve the accuracy of sizing equations when more steel loading is needed. It is also a possible solution to improve the motor efficiency by increasing  $B_{fe}$  at open load condition towards to nonlinear portion of the  $B - H$  curve.
- Armature current effect is neglected in the sizing equations, which has little influence for DW-SPM motors. However, saturation may occur when the slot are large for CW-SPM motors. To solve this issue, bigger rotor is perused as suggested in the dissertation. Another solution is to take account of the armature effect in the sizing equations.
- Inductances are calculated from a simplified 2-D slot model. A more accurate analytical model can be modified into the calculation of inductances. Then the accuracy of estimated PF can be improved.
- Cogging torque calculation of SPM motors is mainly related to the rotor positions. Several rotor positions have to be simulated to get the peak to peak value of cogging torque. The way to reduce the number of rotor positions to get cogging torque value is a promising direction in the study.
- More cross functions can be added as the optimization targets in the automatic design precess, such as the cost of the PMs.

# References

- [1] TJE Miller. *Permanent Magnet and Reluctance Motor Drives*. Oxford, UK: Oxford Science Publications, 1989.
- [2] Thomas A Lipo. *Vector control and dynamics of AC drives*, volume 41. Oxford university press, 1996.
- [3] Ion Boldea. *The induction machines design handbook; 2nd ed.* Electric Power Engineering Series. CRC Press, Hoboken, NJ, 2009.
- [4] Juha Pyrhonen, Tapani Jokinen, and Valeria Hrabovcova. *Design of rotating electrical machines*. John Wiley & Sons, 2013.
- [5] Thomas A Lipo. *Analysis of synchronous machines*. CRC Press, 2012.
- [6] T. M. Jahns. Motion control with permanent-magnet ac machines. *Proceedings of the IEEE*, 82(8):1241–1252, Aug 1994.
- [7] S. S. Williamson, A. Emadi, and K. Rajashekara. Comprehensive efficiency modeling of electric traction motor drives for hybrid electric vehicle propulsion applications. *IEEE Transactions on Vehicular Technology*, 56(4):1561–1572, July 2007.
- [8] P. Pillay and R. Krishnan. Modeling of permanent magnet motor drives. *IEEE Transactions on Industrial Electronics*, 35(4):537–541, Nov 1988.
- [9] R. Islam, I. Husain, A. Fardoun, and K. McLaughlin. Permanent-magnet synchronous motor magnet designs with skewing for torque ripple and cogging torque reduction. *IEEE Transactions on Industry Applications*, 45(1):152–160, Jan 2009.
- [10] P. Pillay and R. Krishnan. Modeling, simulation, and analysis of permanent-magnet motor drives. i. the permanent-magnet synchronous motor drive. *IEEE Transactions on Industry Applications*, 25(2):265–273, Mar 1989.

- [11] L. Zhong, M. F. Rahman, W. Y. Hu, and K. W. Lim. Analysis of direct torque control in permanent magnet synchronous motor drives. *IEEE Transactions on Power Electronics*, 12(3):528–536, May 1997.
- [12] J. D. Livingston. The history of permanent-magnet materials. *JOM*, 42(2):30–34, Feb 1990.
- [13] A Saliba-Silva, R.N Faria, M.A Baker, and I Costa. Improving the corrosion resistance of ndfeb magnets: an electrochemical and surface analytical study. *Surface and Coatings Technology*, 185(2):321 – 328, 2004.
- [14] Yutaka Matsuura. Recent development of nd–fe–b sintered magnets and their applications. *Journal of Magnetism and Magnetic Materials*, 303(2):344 – 347, 2006. The 6th International Symposium on Physics of Magnetic Materials.
- [15] Jacek F Gieras. *Permanent magnet motor technology: design and applications*. CRC press, 2002.
- [16] Duane C Hanselman. *Brushless permanent magnet motor design*. The Writers’ Collective, 2003.
- [17] Ramu Krishnan. *Permanent magnet synchronous and brushless DC motor drives*. CRC press, 2009.
- [18] Dieter Gerling. *Electrical Machines*. Springer, 2016.
- [19] A. Khaligh and Z. Li. Battery, ultracapacitor, fuel cell, and hybrid energy storage systems for electric, hybrid electric, fuel cell, and plug-in hybrid electric vehicles: State of the art. *IEEE Transactions on Vehicular Technology*, 59(6):2806–2814, July 2010.
- [20] J. de Santiago, H. Bernhoff, B. Ekergård, S. Eriksson, S. Ferhatovic, R. Waters, and M. Leijon. Electrical motor drivelines in commercial all-electric vehicles: A review. *IEEE Transactions on Vehicular Technology*, 61(2):475–484, Feb 2012.
- [21] J. Martinez, K. Krischan, and A. Muetze. A two-step analytic design and optimization of small variable speed pmsms for home appliances. In *2016 18th European Conference on Power Electronics and Applications (EPE’16 ECCE Europe)*, pages 1–10, Sept 2016.
- [22] L. Wu, R. Qu, and S. Jia. Low rotor eddy current losses spm servo motors with fractional slot concentrated windings and novel retaining cage. In *2016 IEEE Conference on Electromagnetic Field Computation (CEFC)*, pages 1–1, Nov 2016.



- [23] E. M. Tsampouris, M. E. Beniakar, and A. G. Kladas. Geometry optimization of pmsms comparing full and fractional pitch winding configurations for aerospace actuation applications. *IEEE Transactions on Magnetics*, 48(2):943–946, Feb 2012.
- [24] M. Popescu, D. Staton, D. Dorrell, F. Marignetti, and D. Hawkins. Study of the thermal aspects in brushless permanent magnet machines performance. In *2013 IEEE Workshop on Electrical Machines Design, Control and Diagnosis (WEMDCD)*, pages 60–69, March 2013.
- [25] S. Morimoto, Y. Tong, Y. Takeda, and T. Hirasu. Loss minimization control of permanent magnet synchronous motor drives. *IEEE Transactions on Industrial Electronics*, 41(5):511–517, Oct 1994.
- [26] N. Bianchi, S. Bolognani, and F. Luise. Potentials and limits of high-speed pm motors. *IEEE Transactions on Industry Applications*, 40(6):1570–1578, Nov 2004.
- [27] T. Schneider and A. Binder. *Evaluation of new Surface Mounted Permanent Magnet Synchronous Machine with Finite Element Calculations*, pages 215–220. Springer Netherlands, Dordrecht, 2005.
- [28] J. Dong, Y. Huang, L. Jin, and H. Lin. Comparative study of surface-mounted and interior permanent-magnet motors for high-speed applications. *IEEE Transactions on Applied Superconductivity*, 26(4):1–4, June 2016.
- [29] A. Yousefi-Talouki, P. Pescetto, and G. Pellegrino. Sensorless direct flux vector control of synchronous reluctance motors including standstill, mtpa, and flux weakening. *IEEE Transactions on Industry Applications*, 53(4):3598–3608, July 2017.
- [30] A. Yousefi-Talouki, P. Pescetto, G. Pellegrino, and I. Boldea. Combined active flux and high frequency injection methods for sensorless direct flux vector control of synchronous reluctance machines. *IEEE Transactions on Power Electronics*, PP(99):1–1, 2017.
- [31] A. Yousefi-Talouki and G. Pellegrino. Sensorless direct flux vector control of synchronous reluctance motor drives in a wide speed range including standstill. In *2016 XXII International Conference on Electrical Machines (ICEM)*, pages 1167–1173, Sept 2016.
- [32] Olgierd Cecil Zienkiewicz, Robert Leroy Taylor, Robert Leroy Taylor, and JZ Zhu. *Finite Element Method: Its Basis and Fundamentals, The: Its Basis and Fundamentals*. Elsevier, Incorporated, 2013.

- [33] Nicola Bianchi. *Electrical machine analysis using finite elements*. CRC press, 2005.
- [34] Cupertino F. et al. Syre - synchronous reluctance (machines) – evolution, 2014.
- [35] A. B. Proca, A. Keyhani, A. El-Antably, Wenzhe Lu, and Min Dai. Analytical model for permanent magnet motors with surface mounted magnets. *IEEE Transactions on Energy Conversion*, 18(3):386–391, Sept 2003.
- [36] Gianmario Pellegrino, Alfredo Vagati, Barbara Boazzo, and Paolo Guglielmi. Comparison of induction and pm synchronous motor drives for ev application including design examples. *IEEE Transactions on industry applications*, 48(6):2322–2332, 2012.
- [37] J. Wang, X. Yuan, and K. Atallah. Design optimization of a surface-mounted permanent-magnet motor with concentrated windings for electric vehicle applications. *IEEE Transactions on Vehicular Technology*, 62(3):1053–1064, March 2013.
- [38] S. Jurkovic, K. Rahman, B. Bae, N. Patel, and P. Savagian. Next generation chevy volt electric machines; design, optimization and control for performance and rare-earth mitigation. In *2015 IEEE Energy Conversion Congress and Exposition (ECCE)*, pages 5219–5226, Sept 2015.
- [39] L. J. Wu, Z. Q. Zhu, D. Staton, M. Popescu, and D. Hawkins. Analytical prediction of electromagnetic performance of surface-mounted pm machines based on subdomain model accounting for tooth-tips. *IET Electric Power Applications*, 5(7):597–609, August 2011.
- [40] W. Zhao, T. A. Lipo, and B. I. Kwon. Optimal design of a novel asymmetrical rotor structure to obtain torque and efficiency improvement in surface inset pm motors. *IEEE Transactions on Magnetics*, 51(3):1–4, March 2015.
- [41] A. Rahideh and T. Korakianitis. Analytical armature reaction field distribution of slotless brushless machines with inset permanent magnets. *IEEE Transactions on Magnetics*, 48(7):2178–2191, July 2012.
- [42] R. P. Jastrzebski, P. Jaatinen, O. Pyrhönen, and A. Chiba. Design of 6-slot inset pm bearingless motor for high-speed and higher than 100kw applications. In *2017 IEEE International Electric Machines and Drives Conference (IEMDC)*, pages 1–6, May 2017.
- [43] Z. Zhang, C. Xia, H. Wang, and T. Shi. Analytical field calculation and analysis of surface inset permanent magnet machines with high saliency ratio. *IEEE Transactions on Magnetics*, 52(12):1–12, Dec 2016.

- [44] X. Ge, Z. Q. Zhu, J. Li, and J. Chen. A spoke-type ipm machine with novel alternate airspace barriers and reduction of unipolar leakage flux by step-staggered rotor. *IEEE Transactions on Industry Applications*, 52(6):4789–4797, Nov 2016.
- [45] J. P. Alexander, S. Galioto, and A. M. El-Refaie. First order mechanical sizing equations for the electromagnetic optimization of spoke ipm machines. In *2016 XXII International Conference on Electrical Machines (ICEM)*, pages 357–363, Sept 2016.
- [46] X. Ge, Z. Q. Zhu, J. B. Li, and J. T. Chen. A spoke-type ipm machine with novel alternate airspace barriers and reduction of unipolar leakage flux by step-staggered rotor. In *2015 IEEE International Electric Machines Drives Conference (IEMDC)*, pages 53–59, May 2015.
- [47] Y. Hu, S. Zhu, C. Liu, and K. Wang. Electromagnetic performance analysis of interior pm machines for electric vehicle applications. *IEEE Transactions on Energy Conversion*, PP(99):1–1, 2017.
- [48] Z. S. Du and T. A. Lipo. Permanent magnet material and pulsating torque minimization in spoke type interior pm machines. In *2016 IEEE Energy Conversion Congress and Exposition (ECCE)*, pages 1–8, Sept 2016.
- [49] A. S. Abdel-Khalik, S. Ahmed, and A. M. Massoud. Effect of multilayer windings with different stator winding connections on interior pm machines for ev applications. *IEEE Transactions on Magnetics*, 52(2):1–7, Feb 2016.
- [50] W Len Soong and TJE Miller. Field-weakening performance of brushless synchronous ac motor drives. *IEE Proceedings-Electric Power Applications*, 141(6):331–340, 1994.
- [51] F. W. Merrill. Permanent magnet excited synchronous motors. *Electrical Engineering*, 74(2):143–143, Feb 1955.
- [52] J. Becker, F. Luborsky, and D. Martin. Permanent magnet materials. *IEEE Transactions on Magnetics*, 4(2):84–99, Jun 1968.
- [53] M. Sagawa, S. Fujimura, H. Yamamoto, Y. Matsuura, and K. Hiraga. Permanent magnet materials based on the rare earth-iron-boron tetragonal compounds. *IEEE Transactions on Magnetics*, 20(5):1584–1589, September 1984.
- [54] R. Coehoorn, D.B. de Mooij, and C. de Waard. Meltspun permanent magnet materials containing fe3b as the main phase. *Journal of Magnetism and Magnetic Materials*, 80(1):101 – 104, 1989.

- [55] J. S. Choi and J. Yoo. Design of a halbach magnet array based on optimization techniques. *IEEE Transactions on Magnetics*, 44(10):2361–2366, Oct 2008.
- [56] Moon G. Lee, Sung Q. Lee, and Dae-Gab Gweon. Analysis of halbach magnet array and its application to linear motor. *Mechatronics*, 14(1):115 – 128, 2004.
- [57] Z. Q. Zhu and D. Howe. Instantaneous magnetic field distribution in brushless permanent magnet dc motors. iii. effect of stator slotting. *IEEE Transactions on Magnetics*, 29(1):143–151, Jan 1993.
- [58] O. Laldin, S. D. Sudhoff, and S. Pekarek. Modified carter's coefficient. *IEEE Transactions on Energy Conversion*, 30(3):1133–1134, Sept 2015.
- [59] S. Neville. Use of carter's coefficient with narrow teeth. *Electrical Engineers, Proceedings of the Institution of*, 114(9):1245–1250, September 1967.
- [60] Thomas A Lipo. *Introduction to AC machine design*. Wisconsin Power Electronics Research Center, University of Wisconsin, 2004.
- [61] A. V. Stankovic, E. L. Benedict, V. John, and T. A. Lipo. A novel method for measuring induction machine magnetizing inductance. *IEEE Transactions on Industry Applications*, 39(5):1257–1263, Sept 2003.
- [62] A. Hassanpour Isfahani and S. Vaez-Zadeh. Effects of magnetizing inductance on start-up and synchronization of line-start permanent-magnet synchronous motors. *IEEE Transactions on Magnetics*, 47(4):823–829, April 2011.
- [63] T. A. Lipo and A. Consoli. Modeling and simulation of induction motors with saturable leakage reactances. *IEEE Transactions on Industry Applications*, IA-20(1):180–189, Jan 1984.
- [64] P. Ponomarev, P. Lindh, and J. Pyrhönen. Effect of slot-and-pole combination on the leakage inductance and the performance of tooth-coil permanent-magnet synchronous machines. *IEEE Transactions on Industrial Electronics*, 60(10):4310–4317, Oct 2013.
- [65] M. F. Momen and S. Datta. Analysis of flux leakage in a segmented core brushless permanent magnet motor. *IEEE Transactions on Energy Conversion*, 24(1):77–81, March 2009.
- [66] W. Li, K. T. Chau, C. Liu, S. Gao, and D. Wu. Analysis of tooth-tip flux leakage in surface-mounted permanent magnet linear vernier machines. *IEEE Transactions on Magnetics*, 49(7):3949–3952, July 2013.

- [67] A. M. EL-Refaie. Fractional-slot concentrated-windings synchronous permanent magnet machines: Opportunities and challenges. *IEEE Transactions on Industrial Electronics*, 57(1):107–121, Jan 2010.
- [68] A. Boglietti, A. M. El-Refaie, O. Drubel, A. M. Omekanda, N. Bianchi, E. B. Agamloh, M. Popescu, A. Di Gerlando, and J. Borg Bartolo. Electrical machine topologies: Hottest topics in the electrical machine research community. *IEEE Industrial Electronics Magazine*, 8(2):18–30, June 2014.
- [69] A. M. EL-Refaie and T. M. Jahns. Optimal flux weakening in surface pm machines using fractional-slot concentrated windings. *IEEE Transactions on Industry Applications*, 41(3):790–800, May 2005.
- [70] Ayman M El-Refaie, Thomas M Jahns, and Donald W Novotny. Analysis of surface permanent magnet machines with fractional-slot concentrated windings. *IEEE Transactions on Energy conversion*, 21(1):34–43, 2006.
- [71] N. Bianchi, S. Bolognani, M. D. Pre, and G. Grezzani. Design considerations for fractional-slot winding configurations of synchronous machines. *IEEE Transactions on Industry Applications*, 42(4):997–1006, July 2006.
- [72] Nicola Bianchi, Silverio Bolognani, and Paolo Frare. Design criteria for high-efficiency spm synchronous motors. *IEEE Transactions on energy conversion*, 21(2):396–404, 2006.
- [73] N. Bianchi, S. Bolognani, and M. Dai Pre. Magnetic loading of fractional-slot three-phase pm motors with nonoverlapped coils. *IEEE Transactions on Industry Applications*, 44(5):1513–1521, Sept 2008.
- [74] A. M. El-Refaie and T. M. Jahns. Scalability of surface pm machines with concentrated windings designed to achieve wide speed ranges of constant-power operation. *IEEE Transactions on Energy Conversion*, 21(2):362–369, June 2006.
- [75] A. M. El-Refaie and T. M. Jahns. Impact of winding layer number and magnet type on synchronous surface pm machines designed for wide constant-power speed range operation. *IEEE Transactions on Energy Conversion*, 23(1):53–60, March 2008.
- [76] A. M. El-Refaie, Z. Q. Zhu, T. M. Jahns, and D. Howe. Winding inductances of fractional slot surface-mounted permanent magnet brushless machines. In *2008 IEEE Industry Applications Society Annual Meeting*, pages 1–8, Oct 2008.

- [77] G. Dajaku, W. Xie, and D. Gerling. Reduction of low space harmonics for the fractional slot concentrated windings using a novel stator design. *IEEE Transactions on Magnetics*, 50(5):1–12, May 2014.
- [78] G. Dajaku, H. Hofmann, F. Hetemi, X. Dajaku, W. Xie, and D. Gerling. Comparison of two different ipm traction machines with concentrated winding. *IEEE Transactions on Industrial Electronics*, 63(7):4137–4149, July 2016.
- [79] B. Prieto, M. Martínez-Iturralde, L. Fontán, and I. Elosegui. Analytical calculation of the slot leakage inductance in fractional-slot concentrated-winding machines. *IEEE Transactions on Industrial Electronics*, 62(5):2742–2752, May 2015.
- [80] B. Boazzo, G. Pellegrino, and A. Vagati. Multipolar spm machines for direct drive application: A comprehensive design approach. In *2012 IEEE International Energy Conference and Exhibition (ENERGYCON)*, pages 98–105, Sept 2012.
- [81] Barbara Boazzo, Gianmario Pellegrino, and Alfredo Vagati. Multipolar spm machines for direct-drive application: A general design approach. *IEEE Transactions on Industry Applications*, 50(1):327–337, 2014.
- [82] D. Meeker. Finite element method magnetics (femm), 2014.
- [83] G. Pellegrino and F. Cupertino. Ipm motor rotor design by means of fea-based multi-objective optimization. In *2010 IEEE International Symposium on Industrial Electronics*, pages 1340–1346, July 2010.
- [84] G. Pellegrino and F. Cupertino. Fea-based multi-objective optimization of ipm motor design including rotor losses. In *2010 IEEE Energy Conversion Congress and Exposition*, pages 3659–3666, Sept 2010.
- [85] F. Cupertino, G. M. Pellegrino, E. Armando, and C. Gerada. A syr and ipm machine design methodology assisted by optimization algorithms. In *2012 IEEE Energy Conversion Congress and Exposition (ECCE)*, pages 3686–3691, Sept 2012.
- [86] G. Pellegrino, F. Cupertino, and C. Gerada. Barriers shapes and minimum set of rotor parameters in the automated design of synchronous reluctance machines. In *2013 International Electric Machines Drives Conference*, pages 1204–1210, May 2013.
- [87] G. Pellegrino, F. Cupertino, and C. Gerada. Automatic design of synchronous reluctance motors focusing on barrier shape optimization. *IEEE Transactions on Industry Applications*, 51(2):1465–1474, March 2015.

- [88] F. Cupertino, G. Pellegrino, and C. Gerada. Design of synchronous reluctance machines with multi-objective optimization algorithms. In *2013 IEEE Energy Conversion Congress and Exposition*, pages 1858–1865, Sept 2013.
- [89] F. Cupertino, G. Pellegrino, and C. Gerada. Design of synchronous reluctance motors with multiobjective optimization algorithms. *IEEE Transactions on Industry Applications*, 50(6):3617–3627, Nov 2014.
- [90] M. Palmieri, M. Perta, F. Cupertino, and G. Pellegrino. Effect of the numbers of slots and barriers on the optimal design of synchronous reluctance machines. In *2014 International Conference on Optimization of Electrical and Electronic Equipment (OPTIM)*, pages 260–267, May 2014.
- [91] M. Gamba, G. Pellegrino, and F. Cupertino. Optimal number of rotor parameters for the automatic design of synchronous reluctance machines. In *2014 International Conference on Electrical Machines (ICEM)*, pages 1334–1340, Sept 2014.
- [92] M. Gamba, G. Pellegrino, and A. Vagati. A new pm-assisted synchronous reluctance machine with a nonconventional fractional slot per pole combination. In *2014 International Conference on Optimization of Electrical and Electronic Equipment (OPTIM)*, pages 268–275, May 2014.
- [93] M. Palmieri, M. Perta, F. Cupertino, and G. Pellegrino. High-speed scalability of synchronous reluctance machines considering different lamination materials. In *IECON 2014 - 40th Annual Conference of the IEEE Industrial Electronics Society*, pages 614–620, Oct 2014.
- [94] M. Di Nardo, M. Degano, M. Galea, C. Gerada, M. Palmieri, F. Cupertino, N. Bianchi, and D. Gerada. End barrier shape optimizations and sensitivity analysis of synchronous reluctance machines. In *IECON 2015 - 41st Annual Conference of the IEEE Industrial Electronics Society*, pages 002914–002919, Nov 2015.
- [95] F. Cupertino, M. Palmieri, and G. Pellegrino. Design of high-speed synchronous reluctance machines. In *2015 IEEE Energy Conversion Congress and Exposition (ECCE)*, pages 4828–4834, Sept 2015.
- [96] M. Di Nardo, M. Galea, C. Gerada, M. Palmieri, F. Cupertino, and S. Mebarki. Comparison of multi-physics optimization methods for high speed synchronous reluctance machines. In *IECON 2015 - 41st Annual Conference of the IEEE Industrial Electronics Society*, pages 002771–002776, Nov 2015.
- [97] M. Di Nardo, M. Galea, C. Gerada, M. Palmieri, and F. Cupertino. Multi-physics optimization strategies for high speed synchronous reluctance ma-

- chines. In *2015 IEEE Energy Conversion Congress and Exposition (ECCE)*, pages 2813–2820, Sept 2015.
- [98] C. Lu, S. Ferrari, and G. Pellegrino. Two design procedures for pm synchronous machines for electric powertrains. *IEEE Transactions on Transportation Electrification*, 3(1):98–107, March 2017.
- [99] Wenping Cao, Barrie C Mecrow, Glynn J Atkinson, John W Bennett, and David J Atkinson. Overview of electric motor technologies used for more electric aircraft (mea). *IEEE Transactions on Industrial Electronics*, 59(9):3523–3531, 2012.
- [100] Ayman M El-Refaie. Motors/generators for traction/propulsion applications: A review. *IEEE Vehicular Technology Magazine*, 8(1):90–99, 2013.
- [101] Tim Burrell and Steven Campbell. Benchmarking ev and hev power electronics and electric machines. In *Transportation Electrification Conference and Expo (ITEC), 2013 IEEE*, pages 1–6. IEEE, 2013.
- [102] Silong Li, Yingjie Li, Wooyoung Choi, and Bulent Sarlioglu. High-speed electric machines: Challenges and design considerations. *IEEE Transactions on Transportation Electrification*, 2(1):2–13, 2016.
- [103] International Efficiency Commission et al. Rotating electrical machines-part 30-1: Efficiency classes of line operated ac motors (ie code). Technical report, IEC 60034-30-1, Mar, 2014.
- [104] Srivatsan Ramarathnam, Abdul Kalam Mohammed, Berker Bilgin, Anand Sathyan, Hossein Dadkhah, and Ali Emadi. A review of structural and thermal analysis of traction motors. *IEEE Transactions on Transportation Electrification*, 1(3):255–265, 2015.
- [105] P. Arumugam, Z. Xu, A. La Rocca, G. Vakil, M. Dickinson, E. Amankwah, T. Hamiti, S. Bozhko, C. Gerada, and S. J. Pickering. High-speed solid rotor permanent magnet machines: Concept and design. *IEEE Transactions on Transportation Electrification*, 2(3):391–400, Sept 2016.
- [106] Ali Rabiei, Torbjörn Thiringer, Mikael Alatalo, and Emma Arfa Grunditz. Improved maximum-torque-per-ampere algorithm accounting for core saturation, cross-coupling effect, and temperature for a pmsm intended for vehicular applications. *IEEE Transactions on Transportation Electrification*, 2(2):150–159, 2016.
- [107] Zhi Yang, Fei Shang, Ian P Brown, and Mahesh Krishnamurthy. Comparative study of interior permanent magnet, induction, and switched reluctance



- motor drives for ev and hev applications. *IEEE Transactions on Transportation Electrification*, 1(3):245–254, 2015.
- [108] Martin van der Geest, Henk Polinder, Jan Abraham Ferreira, and Markus Christmann. Power density limits and design trends of high-speed permanent magnet synchronous machines. *IEEE Transactions on Transportation Electrification*, 1(3):266–276, 2015.
- [109] Infolytica. Magnet by infolytica. <http://www.infolytica.com/>, 2017.
- [110] Emission Test Cycles DieselNet. New european driving cycle, 2000.
- [111] A. Boglietti, A. Cavagnino, M. Lazzari, and M. Pastorelli. A simplified thermal model for variable-speed self-cooled industrial induction motor. *IEEE Transactions on Industry Applications*, 39(4):945–952, July 2003.
- [112] Infolytica. Motorsolve by infolytica. <http://www.infolytica.com/>, 2017.
- [113] Amin Mahmoudi, Wen L Soong, Gianmario Pellegrino, and Eric Armando. Efficiency maps of electrical machines. In *Energy Conversion Congress and Exposition (ECCE), 2015 IEEE*, pages 2791–2799. IEEE, 2015.
- [114] C. Lu and G. Pellegrino. Magnet shape optimization of surface-mounted permanent magnet synchronous machine through fea method. *Journal of Electrical Engineering*, 17, 2017.
- [115] Z. Q. Zhu and D. Howe. Influence of design parameters on cogging torque in permanent magnet machines. *IEEE Transactions on Energy Conversion*, 15(4):407–412, Dec 2000.
- [116] T. M. Jahns and W. L. Soong. Pulsating torque minimization techniques for permanent magnet ac motor drives-a review. *IEEE Transactions on Industrial Electronics*, 43(2):321–330, Apr 1996.
- [117] Y. Duan and D. M. Ionel. A review of recent developments in electrical machine design optimization methods with a permanent-magnet synchronous motor benchmark study. *IEEE Transactions on Industry Applications*, 49(3):1268–1275, May 2013.
- [118] R. Lateb, N. Takorabet, and F. Meibody-Tabar. Effect of magnet segmentation on the cogging torque in surface-mounted permanent-magnet motors. *IEEE Transactions on Magnetics*, 42(3):442–445, March 2006.
- [119] D. Zarko, D. Ban, and T. A. Lipo. Analytical solution for cogging torque in surface permanent-magnet motors using conformal mapping. *IEEE Transactions on Magnetics*, 44(1):52–65, Jan 2008.

- [120] C. Lu and G. Pellegrino. A simple design method for surface-mounted pm machines for traction application. In *2016 IEEE Energy Conversion Congress and Exposition (ECCE)*, pages 1–7, Sept 2016.
- [121] Timothy A Burress, Steven L Campbell, Chester Coomer, Curtis William Ayers, Andrew A Wereszczak, Joseph Philip Cunningham, Laura D Marlino, Larry Eugene Seiber, and Hua-Tay Lin. Evaluation of the 2010 toyota prius hybrid synergy drive system. Technical report, Oak Ridge National Laboratory (ORNL); Power Electronics and Electric Machinery Research Facility, 2011.
- [122] Robert H Staunton, Timothy A Burress, and Laura D Marlino. Evaluation of 2005 honda accord hybrid electric drive system. Technical report, Oak Ridge National Laboratory (ORNL), Oak Ridge, TN, 2006.
- [123] Ayman M El-Refaie and Thomas M Jahns. Optimal flux weakening in surface pm machines using concentrated windings. In *Industry Applications Conference, 2004. 39th IAS Annual Meeting. Conference Record of the 2004 IEEE*, volume 2, pages 1038–1047. IEEE, 2004.
- [124] F. Magnussen and C. Sadarangani. Winding factors and joule losses of permanent magnet machines with concentrated windings. In *Electric Machines and Drives Conference, 2003. IEMDC'03. IEEE International*, volume 1, pages 333–339 vol.1, June 2003.
- [125] A. M. EL-Refaie, M. R. Shah, J. P. Alexander, S. Galimoto, K. K. Huh, and W. D. Gerstler. Rotor end losses in multiphase fractional-slot concentrated-winding permanent magnet synchronous machines. *IEEE Transactions on Industry Applications*, 47(5):2066–2074, Sept 2011.
- [126] F Biais and Ph Langry. Optimization of a permanent magnet traction motor for electric vehicle. In *Colloque sur les véhicules électriques et hybrides*, pages 59–71, 1999.
- [127] Keld Folsach Rasmussen, John H Davies, TJE Miller, MI McGelp, and Mircea Olaru. Analytical and numerical computation of air-gap magnetic fields in brushless motors with surface permanent magnets. *IEEE Transactions on Industry Applications*, 36(6):1547–1554, 2000.
- [128] G. Pellegrino M. Davoli C. Lu, S. Ferrari and C. Bianchini. Parametric design method for spm machines including rounded pm shape. In *2017 IEEE Energy Conversion Congress and Exposition (ECCE)*, pages 1–7, Oct 2017.
- [129] Z. Q. Zhu and D. Howe. Analytical prediction of the cogging torque in radial-field permanent magnet brushless motors. *IEEE Transactions on Magnetics*, 28(2):1371–1374, Mar 1992.

- [130] W. Q. Chu and Z. Q. Zhu. Investigation of torque ripples in permanent magnet synchronous machines with skewing. *IEEE Transactions on Magnetics*, 49(3):1211–1220, March 2013.
- [131] N. Bianchi and S. Bolognani. Design techniques for reducing the cogging torque in surface-mounted pm motors. *IEEE Transactions on Industry Applications*, 38(5):1259–1265, Sep 2002.
- [132] C. Bianchini, M. Davoli, G. Pellegrino, F. Immovilli, and E. Lorenzani. Low cost pm synchronous servo-applications employing asynchronous-motor frame. In *2015 IEEE Energy Conversion Congress and Exposition (ECCE)*, pages 6090–6095, Sept 2015.
- [133] Y. Pang, Z. Q. Zhu, and Z. J. Feng. Cogging torque in cost-effective surface-mounted permanent-magnet machines. *IEEE Transactions on Magnetics*, 47(9):2269–2276, Sept 2011.
- [134] K. I. Laskaris and A. G. Kladas. Permanent-magnet shape optimization effects on synchronous motor performance. *IEEE Transactions on Industrial Electronics*, 58(9):3776–3783, Sept 2011.
- [135] Z. Chen, C. Xia, Q. Geng, and Y. Yan. Modeling and analyzing of surface-mounted permanent-magnet synchronous machines with optimized magnetic pole shape. *IEEE Transactions on Magnetics*, 50(11):1–4, Nov 2014.
- [136] E. Armando, P. Guglielmi, G. Pellegrino, and R. Bojoi. Flux linkage maps identification of synchronous ac motors under controlled thermal conditions. In *2017 IEEE International Electric Machines and Drives Conference (IEMDC)*, pages 1–8, May 2017.
- [137] Z. Q. Zhu, D. Howe, and C. C. Chan. Improved analytical model for predicting the magnetic field distribution in brushless permanent-magnet machines. *IEEE Transactions on Magnetics*, 38(1):229–238, Jan 2002.
- [138] Z. J. Liu and J. T. Li. Accurate prediction of magnetic field and magnetic forces in permanent magnet motors using an analytical solution. *IEEE Transactions on Energy Conversion*, 23(3):717–726, Sept 2008.
- [139] F. Dubas and C. Espanet. Analytical solution of the magnetic field in permanent-magnet motors taking into account slotting effect: No-load vector potential and flux density calculation. *IEEE Transactions on Magnetics*, 45(5):2097–2109, May 2009.
- [140] Z. Q. Zhu, L. J. Wu, and Z. P. Xia. An accurate subdomain model for magnetic field computation in slotted surface-mounted permanent-magnet machines. *IEEE Transactions on Magnetics*, 46(4):1100–1115, April 2010.

- [141] L. J. Wu, Z. Q. Zhu, D. Staton, M. Popescu, and D. Hawkins. An improved subdomain model for predicting magnetic field of surface-mounted permanent magnet machines accounting for tooth-tips. *IEEE Transactions on Magnetics*, 47(6):1693–1704, June 2011.
- [142] L. J. Wu, Z. Q. Zhu, D. Staton, M. Popescu, and D. Hawkins. Analytical model of eddy current loss in windings of permanent-magnet machines accounting for load. *IEEE Transactions on Magnetics*, 48(7):2138–2151, July 2012.
- [143] L. J. Wu and Z. Q. Zhu. Simplified analytical model and investigation of open-circuit ac winding loss of permanent-magnet machines. *IEEE Transactions on Industrial Electronics*, 61(9):4990–4999, Sept 2014.
- [144] L. Wu and Z. Q. Zhu. Analytical modeling of surface-mounted pm machines accounting for magnet shaping and varied magnet property distribution. *IEEE Transactions on Magnetics*, 50(7):1–11, July 2014.
- [145] Y. Zhou, H. Li, G. Meng, S. Zhou, and Q. Cao. Analytical calculation of magnetic field and cogging torque in surface-mounted permanent-magnet machines accounting for any eccentric rotor shape. *IEEE Transactions on Industrial Electronics*, 62(6):3438–3447, June 2015.
- [146] C. Xia, Z. Chen, T. Shi, and H. Wang. Cogging torque modeling and analyzing for surface-mounted permanent magnet machines with auxiliary slots. *IEEE Transactions on Magnetics*, 49(9):5112–5123, Sept 2013.
- [147] C. Xia, Z. Zhang, and Q. Geng. Analytical modeling and analysis of surface mounted permanent magnet machines with skewed slots. *IEEE Transactions on Magnetics*, 51(5):1–8, May 2015.
- [148] T. Lubin, S. Mezani, and A. Rezzoug. Two-dimensional analytical calculation of magnetic field and electromagnetic torque for surface-inset permanent-magnet motors. *IEEE Transactions on Magnetics*, 48(6):2080–2091, June 2012.